

Investigating Biochemical Interactions Relevant To Human Health Using  
Backscattering Interferometry

By

Ian R. Olmsted

Dissertation

Submitted to the Faculty of the  
Graduate School of Vanderbilt University  
in partial fulfillment of the requirements

for the degree of

DOCTOR OF PHILOSOPHY

in

Chemistry

August, 2013

Nashville, TN

Approved:

Darryl J. Bornhop

John A. McLean

Eric P. Skaar

David W. Wright

Copyright © 2013 by Ian R. Olmsted

All rights reserved

To the giants who came before me, on whose shoulders I stand.

## ACKNOWLEDGEMENTS

This work was funded by NSF, Vanderbilt University, NIH and the Labrecque Foundation. I would like to thank my committee members for guidance and support. I am especially grateful to Dr. Bornhop for continually pushing me to accomplish more. Many former and present Bornhop group members, particularly Amanda Kussrow and Frank Moss, have been very helpful in the advancement of this work. I am thankful to my parents who always encouraged me to reach higher, and most of all to my adoring wife Spring, who has always been there for me despite my meager graduate student's salary.

## TABLE OF CONTENTS

	Page
DEDICATION .....	iii
ACKNOWLEDGEMENTS.....	iv
LIST OF TABLES .....	viii
LIST OF FIGURES .....	ix
Chapter	
1. Introduction	
1.1 Importance of early disease detection and diagnosis .....	1
1.2 Common biomolecular interaction detection methods .....	2
1.2.1 Enzyme Linked Immunosorption Assay.....	3
1.2.3 Real-time polymerase chain reaction .....	4
1.2.4 Fluorescence-based assays.....	6
1.2.1 Surface Plasmon Resonance .....	8
1.2.5 Isothermal Calorimetry .....	9
1.2.6 Interferometric methods.....	10
1.3 Backscattering Interferometry .....	19
2. Comparison of free-solution and surface-immobilized molecular interactions using a single platform	
2.1 Introduction .....	28
2.2 Methods .....	31
2.2.1 Surface immobilization procedures.....	31
2.2.2 Surface characterization .....	33
2.2.3 Immobilized assay procedures .....	34
2.2.4 Free solution assay procedures.....	35
2.3 Results and discussion .....	35
2.3.1 Free-solution measurement.....	35
2.3.2 Surface vs. free-solution: how tether distance impacts measured affinity for concanavalin A.....	37
2.4 Summary and future directions .....	43
3. Probing allosteric aptamer-protein interactions with backscattering interferometry	
3.1 Aptamers as potential therapeutics.....	45
3.2 Methods .....	46
3.3 Results.....	48

3.3.1 BSI measurement of equilibrium binding constants of aptamers .....	48
3.3.2 Multivalent interactions affect exosite binding characteristics .....	50
3.3.3 Computational structural modeling .....	52
3.4 Summary and future directions .....	52
4. The effect of hybridization-induced secondary structure on RNA detection using backscattering interferometry	
4.1 Introduction .....	54
4.2 Materials and methods.....	57
4.2.1 Preparation of the synthetic RNA target .....	57
4.2.2 Synthesis of the oligonucleotide probes .....	57
4.2.3 Quantification of relative nucleic acid hybridization .....	58
4.2.4 Preparation and evaluation of surrogate nasal wash samples ..	58
4.2.5 RNA folding analysis .....	59
4.2.6 Nucleic acid secondary structure determination .....	60
4.3 Results.....	61
4.3.1 Enhanced BSI sensitivity using 22-mer probe length .....	61
4.3.2 Enhanced BSI sensitivity using multiple distributed probes .....	64
4.3.3 Target specificity is maintained in RNA samples extracted from complex matrices .....	66
4.3.4 RNA target folding affects BSI binding signal .....	68
4.3.5 Enhanced BSI sensitivity using LNA probes.....	70
4.3.6 Induced A-form secondary structure improves BSI sensitivity.....	72
4.4 Discussion .....	75
4.5 Summary and future directions .....	80
5. Improving the current limits of detection of non-small cell lung cancer biomarkers via backscattering interferometry	
5.1 Introduction .....	82
5.2 Materials and methods.....	84
5.2.1 Biomarker calibration curve construction.....	84
5.2.2 BSI patient serum sample analysis.....	85
5.3 Results and discussion .....	86
5.3.1 Improving current limits of detection .....	86
5.3.2 Patient serum sample analysis .....	88
5.4 Summary and future directions .....	91
6. Baclofen and other GABA <sub>B</sub> receptor agents are allosteric modulators of the CXCL12 chemokine receptor CXCR4	
6.1 Introduction .....	93

6.2 Materials and Methods.....	94
6.3 Results and Discussion.....	95
6.4 Summary .....	99
6.4.1 Physiological implication.....	100
6.4.2 Putative applications in cancer treatment and inflammation....	101
6.4.3 Key observations and future directions.....	102
 7. Multiplexing the backscattering interferometer for improved performance and higher throughput	
6.1 Introduction .....	104
6.2 Previous BSI multiplex strategies .....	105
6.3 Single Channel Sample Reference BSI .....	105
6.4 Results.....	107
6.5 Summary and future directions .....	114
 8. Conclusions .....	116
 Appendices.....	120
 References .....	127
 Curriculum Vitae .....	142

## LIST OF TABLES

Table .....	Page
2.1 Summary of affinities with respect to distance from the surface.....	41
3.1 Comparison of aptamer-thrombin binding affinities obtained using BSI ..	48
4.1 Summary of probe:RSV assay results .....	64
5.1 Comparison of BSI and ELISA performance .....	91



## LIST OF FIGURES

Figure .....	Page
1.1 Block diagram of a Mach-Zehnder interferometer (MZI).....	12
1.2 Block diagram of a Young interferometer (YI).....	13
1.3 Block diagram of diffraction optics .....	15
1.4 Block diagram of a dual polarization interferometer (DPI) .....	17
1.5 Block diagram of a bilayer interferometer (BLI) .....	19
1.6 Block diagram of a backscattering interferometer (BSI) .....	21
2.1 Biotinylated ConA immobilized on an ester-activated glass slide at various distances from the surface .....	32
2.2 Mannose and glucose bind to ConA in free-solution .....	36
2.3 Tapping-mode AFM characterization of surface chemistry.....	38
2.4 Comparison of $1/K_{ads}$ vs. distance from the channel surface .....	42
3.1 Measurement of dissociation binding constants of aptamers to thrombin using the single channel BSI setup.....	49
3.2 Measurement of aptamer binding to pre-formed aptamer-protein complexes .....	50
4.1 Comparison of the BSI binding response and net hybridization upon adding various DNA probes to the RNA target .....	62
4.2 Comparison of the BSI binding response and net hybridization of various numbers and distributions of probes to the RNA target .....	65
4.3 Saturation curves of target RNA incubated with either a single 22-mer probe or a mixture of nine distributed probes .....	66
4.4 Evaluations of BSI specificity.....	67
4.5 DNA probes designed to bind different regions of the RNA target generate a range of BSI binding responses .....	69

4.6 Comparison of the BSI binding response and net hybridization of LNA and DNA probes of the same sequence to target RNA .....	70
4.7 Relative degree of A-form nucleic acid character of the DNA:DNA, DNA:RNA, and LNA:RNA hybrids corresponds with BSI signal .....	72
4.8 Relative degree of A-form character corresponds to increased BSI signal .....	74
5.1 BSI out-performs ELISA for the detection of cyfra 21-1 and galectin-7 .....	88
5.2 Raw patient sample data for cyfra 21.1 and galectin-7 .....	89
5.3 Cyfra 21.1 concentrations in patient serum samples measured by BSI.....	90
6.1 Representative plots of BSI signal versus ligand concentration for the determinations of binding constants for CXCR4 .....	97
6.2 The binding of baclofen to CXCR4 is enhanced when SDF is already bound to the allosteric site .....	98
7.1 Block diagram of the SCSR-BSI optical train.....	107
7.2 Plot of SCSR-BSI instrumental noise .....	108
7.3 Temperature calibration curve of two separate regions of the SCSR-BSI capillary .....	109
7.4 Glycerol calibration curve interrogating two separate regions of the SCSR-BSI capillary .....	111
7.5 Calibration curve where region 1 contains water as a reference and region 2 contains varying concentrations of glycerol .....	113
A.1 Concanavalin A surface immobilization chemistry .....	120
A.2 Free-solution binding determinations .....	120
B.1 Computational model of thrombin-aptamer interactions.....	122

## CHAPTER 1

### BIOMOLECULAR INTERACTIONS IN DETECTION AND DISEASE DIAGNOSIS

#### 1.1 Importance of early disease detection and diagnosis

Early detection is generally the most important factor in successfully curing, treating, or managing most diseases. Often, the earlier a disease is diagnosed, the more likely it is that it can be cured or successfully treated. Managing a disease, especially early in its course, may lower its impact on patient life or prevent serious complications. Many diseases such as cancer, HIV, and kidney disease are most effectively treated before any symptoms or warning signs are manifested. Unfortunately, by the time a patient shows signs of illness, it has often progressed to an advanced stage, making treatment difficult leading to an overall survival rate that is diminished. It is therefore critical to be able to detect and diagnose diseases at the earliest possible stage. This goal is partially accomplished today, yet it may be possible, in part through regular screening with technologies capable of quantifying disease biomarkers at clinically relevant concentrations, to expand medicine to be more personalized and thus efficacious.

Early detection is best embodied in tests that are able determine the presence or absence of a disease or condition in an apparently healthy individual. The most common early detection methods include blood tests for an array of indicators, imaging techniques such as x-ray and MRI, or molecular

interaction-based techniques that detect the presence of a disease-specific biomarker, such as the RNA of respiratory syncytial virus (RSV), or proteins excreted from metastatic tumor cells such as prostate specific antigen (PSA), carcinoembryonic antigen (CEA) and cyfra 21-1[13-17]. Each early diagnostic tool is different in design and methodology, affecting the sensitivity (ability to correctly identify those with the disease), specificity (ability to correctly identify those without the disease), and positive and negative predictive values of the tool. Ideally, early diagnostic tests are rapid, simple, safe, cost effective, and minimally invasive.

## **1.2 Common biomolecular interaction detection methods**

Generally, biomarker discovery and validation, disease detection, and treatment efficacy monitoring rely on some form of molecular interaction detection methodology. A number of methods are currently employed to monitor biomolecular interactions, covering a wide range of complexity and performance. These techniques include immuno-precipitation, fluorescence spectroscopy (fluorescence polarization, etc.), isothermal titration calorimetry (ITC), real-time polymerase chain reaction (RT-PCR), surface plasmon resonance (SPR), enzyme linked immunosorption assay (ELISA), electrochemical detection, quartz microbalance mass detection, mass spectrometry and several forms of interferometry. Although each is effective for specific applications, these methods also possess certain limitations. Several approaches require a label of some type (e.g. fluorescent); some involve complicated surface chemistry (e.g. SPR,

ELISA), some are expensive and time consuming, while others have low sensitivity and require large sample quantities (e.g., ITC) or require the use of easily degraded enzymes (RT-PCR). Therefore, there exists a need for an efficient detection method that will allow the investigator to determine if chemical or biochemical species interacted, rapidly, robustly, with high sensitivity, a good dynamic range and in small sample volumes. The Holy Grail would be to perform these determinations in free solution, and label-free keeping assay complexity and cost to a minimum. Label-free techniques are particularly attractive because theoretically they can study interacting species without a chemical modification that could impact how they react. This dissertation will focus on label-free molecular interaction methods.

### **1.2.1 Enzyme Linked Immunosorption Assay**

ELISA is perhaps the most common antibody-based detection method in use today[18]. Typically, target antigens are fished from the sample, usually via a specific antibody that has been immobilized in a polystyrene microtiter plate. After the antigen is immobilized, the detection molecule is added, forming a complex with the antigen. Between each step in an ELISA assay, the plate is typically washed with a mild detergent solution to remove any proteins or antibodies that are not specifically bound. After the final wash step, the plate is developed by adding an enzymatic substrate to produce a visible signal, which indicates the quantity of antigen in the sample. Various signal transduction and amplification methods are used in ELISA. One example is the detection of an

antibody that is covalently linked to a color changing enzyme using a uv-vis detector. Currently, chemiluminescent detection platforms (i.e. Luminex) represent the most sensitive form of signal transduction routinely providing detection in the femtomolar to nanomolar range depending on the application[19-21], but this method is more expensive than the more common detection approaches.

ELISA assays are widely used, generally reliable and relatively sensitive[22]. However, assay development is time consuming and relies on the ability to isolate two molecules, generally antibodies, that bind different regions (epitopes) of the target. Furthermore, complicated immobilization and bioconjugation chemistry are necessary, requiring many costly months of development. Finally, with the exception of the very new, microfluidic-based formats[23], ELISA is relatively sample intensive, commonly requiring milliliters of precious sample such as human serum.

### **1.2.2 Real-time Polymerase Chain Reaction**

PCR is a biochemical technology used to amplify a single or a few copies of a strand of DNA, ultimately generating thousands to millions of copies of a particular DNA sequence. Developed in 1983 by Kary Mullis[24], PCR is now a common technique used in medical and biological research labs for a variety of applications[25, 26]. The method relies on thermal cycling, consisting of cycles of repeated heating and cooling of the reaction for DNA melting and enzymatic replication of the DNA. Primers (short DNA fragments) containing sequences

complementary to the target region along with a DNA polymerase (after which the method is named) are key components to enable repeated rounds of amplification. Almost all PCR applications employ a heat-stable DNA polymerase, such as Taq polymerase, an enzyme originally isolated from the bacterium *Thermus aquaticus*. This DNA polymerase enzymatically assembles a new DNA strand from DNA building-blocks, the nucleotides, by using single-stranded DNA as a template and DNA oligonucleotides (also called DNA primers), which are required for initiation of DNA synthesis. Real-time PCR-based assays have gained favor in the recent past, especially in the field of molecular diagnostics[27]. However, the wide use of real-time PCR methods has also highlighted some of the critical points and limitations of these assays.

While PCR is unquestionably one of the most sensitive methods for detecting nucleotides, the reliance of the technique on thermally sensitive enzymes which have strict storage requirements, make the method less than ideal in regions of the world (rural and third world areas) where the ability to ship and store reagents at specific temperatures is not practical. Furthermore, PCR is more expensive than alternative approaches. The direct costs of PCR reagents, equipment, dedicated space, personnel training, and labor have been reported to be as high as US\$125 per reaction[28]. Even though DNA sequencing is being widely used in disease detection (Hepatitis C[29], West Nile virus[30], *Helicobacter pylori* infection[31]), and even for profiling cancer patients for therapy selection (Caris Life Sciences, etc.), the presence or absence of a nucleotide is not, in many cases, the desired information needed to diagnose a disease,

monitor treatment or determine drug efficacy. For example, many cancer diagnostic tests involve the detection of protein biomarkers[13, 14, 16, 32], and many drug efficacy monitoring tests measure drug metabolite levels[33, 34].

### **1.2.3 Fluorescence-based assays**

Fluorescence spectroscopy measures the light emitted from a molecule upon excitation by a light source and has very high sensitivity, allowing for the detection of a single molecule, and is the common form of signal transduction in ELISA and PCR assays [35, 36]. The two most common approaches used to specifically study molecular interactions are fluorescence (Förster) resonance energy transfer (FRET) and fluorescence polarization (FP).

FRET capitalizes on a mechanism based on detecting the energy transfer between two chromophores [37] and can be used as a molecular ruler. In this extremely powerful technique, a donor chromophore, which is in an excited state, transfers energy to an acceptor chromophore via non-radiative dipole-dipole coupling[38]. The efficiency of this energy transfer is approximately inversely proportional to the sixth power of the distance between donor and acceptor making FRET extremely sensitive to molecule-molecule separation[39]. FRET can be used to determine if two fluorophores are within a certain distance of each other[40] and has been used to detect molecular interactions in a number of systems such as cell-surface protein-protein interactions, protein heteromerization and at the single molecule level[41-43]. FRET has also been used to measure distances between domains in a single protein, providing information about protein conformation[44]. A limitation of FRET is the



requirement for external illumination to initiate the fluorescence transfer, which can lead to background noise from direct excitation of the acceptor or to photobleaching. Another factor that can limit FRET detectability is a donor:acceptor stoichiometry that is outside the range of 10:1 to 1:10[45]. For FRET measurements of protein–protein interactions where one partner might be in excess, this can be a serious limitation.

Fluorescence polarization assay (FPA) is a homogeneous assay useful for the rapid and specific detection of molecular interactions[46]. The principle of the assay is that a fluorescent dye (attached to one of the two binding pair) can be excited by plane-polarized light at the appropriate wavelength, with the resulting emission being principally polarized in the same orientation as the excitation source. Since molecular motion is size dependent, the magnitude of emitted and polarized fluorescence is impacted upon a binding event. As a rule, a small molecule rotates faster when in solution than a larger molecule. When a small molecule that previously rotated rapidly binds to a larger molecule, the rotation rate is decreased leading to a reduction in the measured polarized fluorescence. When measuring antigen-antibody interactions, the rate of reaction is very rapid and usually a result may be obtained in minutes[47], as opposed to 4-8 hours required for ELISA-based assays. Such decreases in time requirements allow for more rapid assay development. Fluorescence polarization has been shown to be effective in measuring a vast array of bimolecular binding events such as protein–protein, DNA–protein, DNA–DNA, receptor–ligand, and protein–drug interactions [48-50]. Additionally, FP can be performed in picoliters of sample,

making the characterization of precious or costly samples more accessible [50]. However, one inherent challenge with FP, FRET, and fluorescent-based assays as a whole, is that the addition of a label can affect binding properties and conformation due to an alteration in the protein structure[51].

#### **1.2.4 Surface Plasmon Resonance**

Label-free methods play an important role in molecular interaction studies. Not only do label-free assays save time and reduce cost, by eliminating chemical labeling, but they also allow for measurements to be made without the potential perturbation due to the label [52]. SPR has become a common technique for label-free monitoring of binding events in small volumes [5, 53-56]. SPR measures the localized change in the refractive index (RI) near the surface in order to detect binding [57-59] and has been implemented in numerous formats. SPR has the advantage of allowing the determination of both forward and reverse reaction rates of the binding in order to calculate the dissociation constant. However, any refractive index change between different solutions must be taken into account when using this technique. Also, SPR is a heterogeneous (e.g. requires one of the species to be tethered to the sensor surface) method that requires complicated surface chemistry and expensive gold-plated slides[54, 58]. The gold plating is needed for generation of the surface Plasmon, and while significant progress has been made to simplify the immobilization chemistry, the attachment of a molecule to a surface can change the protein structure which can affect the binding[55] and/or alter the affinity of the interaction,[5, 11, 60, 61].

This perturbation is especially problematic if the molecule must be mutated in order to make the attachment possible[62]. Furthermore, the surface loading of the chip is critical to protein binding determinations as different methods of attachment can cause variations in the KD values calculated. Finally, the SPR measurements are mass sensitive, which makes it difficult to monitor the binding of a small ligand to a large protein without immobilizing the small molecule (ligand)[5, 63-65].

### **1.2.5 Isothermal Calorimetry**

ITC takes advantage of the fact that heat is a universal signal that will always be absorbed or produced when compounds interact. ITC is performed by monitoring the heat change for a series of small injections of ligand. Many biophysical values of interest, such as  $\Delta G$ ,  $\Delta H$ , and  $\Delta S$ , as well as KD, can be extracted from ITC experiments. However, despite the advantage of being able to calculate these constants, the disadvantages of ITC are that the assay typically requires long analysis times and significantly more material than other methods due to the large sample volumes and the high concentrations required[11, 65-67]. Large sample quantities are particularly problematic when there is a limited amount of the analyte available to perform the study, such as the characterization of precious post-mortem patient samples or costly/hard to synthesize compounds.

### **1.2.6 Interferometric Methods:**

When two or more light waves are superimposed, an interference pattern is created. By studying these patterns, the properties of the light waves and the material that they have been in contact with can be explored. The field of interferometry, has produced some of the most sensitive optical measurement techniques devised by humans. As a result, interferometer has been implemented widely and in applications, including astronomy, metrology, oceanography, seismology, and biological sciences[68].

Interferometry has also been applied to biological sciences as a tool to monitor and quantify molecular interactions[3, 6, 52, 69-79]. Interferometry offers the dual advantage of being a highly sensitive technique that does not require the use of expensive molecular labels. Therefore, molecular interactions may be characterized with both binding partners in their native states, eliciting quantitative, meaningful (i.e. unperturbed by labeling) affinity data in a cost-effective format. Here we describe several different types of interferometers which have been successfully utilized to study molecular interactions.

#### *Mach-Zehnder Interferometer:*

The Mach–Zehnder interferometer (MZI) is a device used to determine the relative phase shift between two collimated beams derived by splitting light from a single source and then combining the beams. This type of interferometer has been used, among other things, to measure phase shifts between the two beams caused by a difference in refractive index (RI) between the sample and the

reference arm of a waveguide (Figure 1.1). A laser light source illuminates a single-mode waveguide which is then split into a sample and reference arm. The reference arm is coated with a thin cladding layer, while the sample arm has a window to allow the evanescent field to interact with the sample. Finally, the sensor and reference arms are recombined which leads to beam interference. When no sample is present (both arms contain the same sample), the two waves have the same phase. However, when a sample with a different refractive index (RI) to that of the reference arm is added to one of the arms a phase change occurs in the second beam path, resulting in a change in the energy distribution of light in the interference pattern, leading to a change in the intensity of the fringes. Binding events are thereby quantified by detecting the difference in intensity of the interaction channel and the reference channel of the interferometer shown in figure 1.1 using a photodetector.

Intrinsically, the evanescent sensing approach of the MZI instrumental configuration requires a single polarization and single-mode illumination to prevent interference from cross-polarization and multimodal effects. The sensitivity of the MZI is generally correlated with the length of the sensing window, making it difficult to measure low concentrations of analytes without using long path lengths and thus relatively large amounts of sample is required to fill the channel. The MZI was first used for biosensing in 1993 and has since been utilized in a broad range of applications[69, 80-83]. In 1997, Brosinger *et al.*, demonstrated the ability to resolve a refractive index change of  $2 \times 10^{-5}$  refractive index units (RIU) with their early MZI configuration[80]. Initial

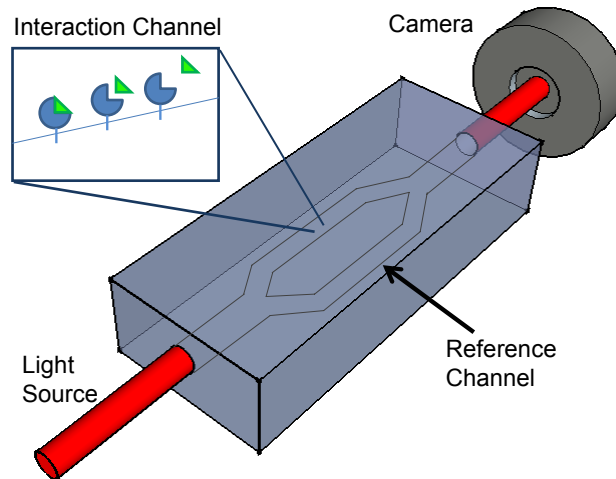


**Figure 1.1:** Block diagram of a Mach-Zehnder interferometer (MZI)

experiments to test the biosensing ability of the instrument were also reported, demonstrating that MZI can detect fetal calf serum binding nonspecifically to the sensor surface[80]. More recently, Bruck et al. have developed a novel polymer-based MZI which is compatible with mass production techniques such as injection molding and spin coating[84]. This group reports label-free protein detection with sensitivity of  $\sim 100$  ng/mL. Though such detection limits are not compatible with most ultra-sensitive biosensors, it is a cost efficient alternative for routine protein analysis where expected concentrations are within the dynamic range of the polymer-based MZI.

*Young Interferometer:*

Another waveguiding interferometer is the Young interferometer (YI). The Young interferometer, also called Young's double-slit interferometer, was the

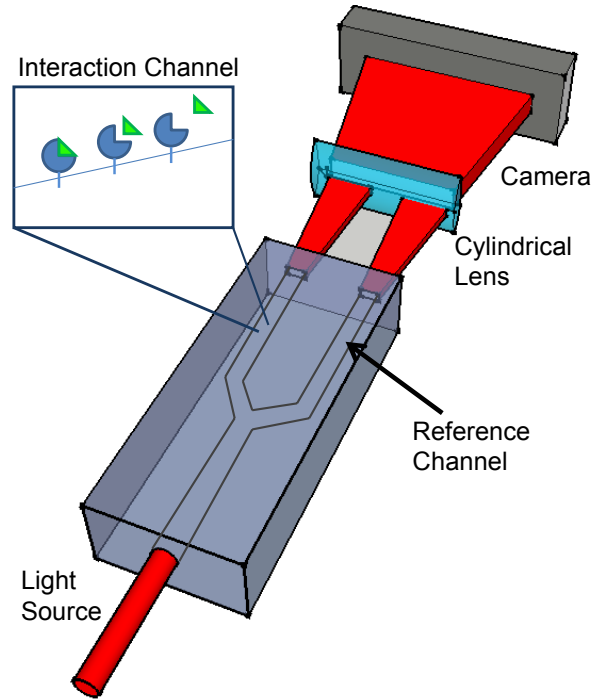


**Figure 1.2:** Block diagram of a Young interferometer (YI)

original version of the modern double-slit experiment, performed at the beginning of the nineteenth century by Thomas Young[85]. This experiment played a major role in the general acceptance of the wave theory of light. Today's YI configuration employs a single-mode laser to illuminate a single-mode waveguide, which is then split into a sample and reference arm, as with the Mach-Zehnder interferometer. However, instead of creating interference by recombining the individual waveguides as in the MZI, the YI the optical output of the individual waveguides interact in free space to create the interference fringes, which are displayed onto a CCD camera (Figure 1.2).

The YI was first used to measure molecular interactions in 1994[69] and has been widely published on thereafter[86-88]. In 2007, Ymeti *et al.* reported a

refractive index detection limit of  $1 \times 10^{-8}$  RIU for their ultrafast integrated handheld YI[89, 90]. In 2012, the same group detected femtomoles of HSV-1 and avian-influenza viruses at the biosensor surface[91].

#### *Diffraction Optics:*

Diffraction-based sensing employs a technique of immobilizing the probe molecules into an array of closely spaced strips that will diffract an incoming laser light to create an interference pattern (Figure 1.3). This interference pattern has been shown to change as sample is introduced and binding occurs on the strips of capture species. The resulting change in the height and refractive index of the diffraction grating changes the intensity of diffracted light. The intensity of the refractive spots is measured using a photodetector, allowing changes associated with a binding event within the sample to be measured. Though label-free applications of diffraction optics exist, performance can be enhanced by using labeling strategies.

Early studies by St. John *et al.* demonstrated that diffraction optics can be used to detect whole bacteria cells captured using an antibody grating stamped on a silicon surface[92]. Currently, Axela Biosensors offers a commercialized diffraction based sensor known as the dotLab™ System which enables multiplexing of immunoassays over a broad dynamic range. They demonstrated the ability to simultaneously measure binding of two similar sets of antibody/analyte pairs with concentrations which differed by 6 orders of magnitude; however, labeling strategies were implemented to measure the



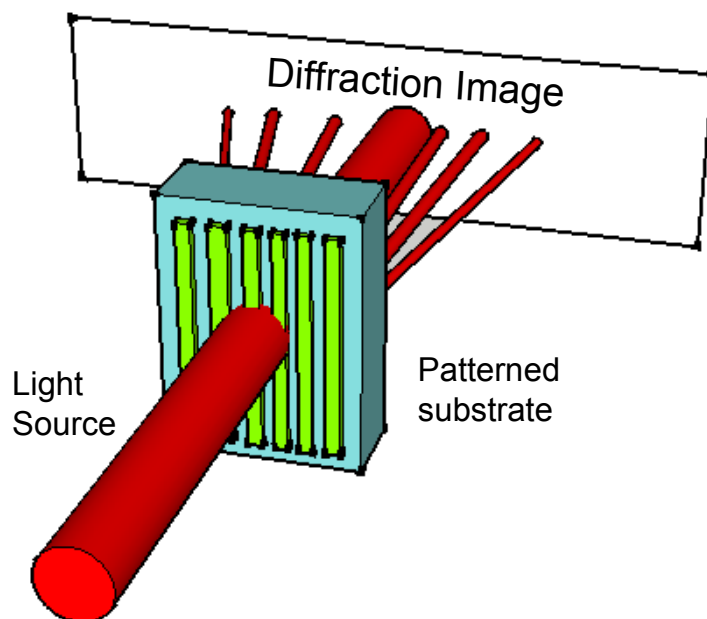


**Figure 1.3:** Block diagram of diffraction optics

analyte of lower concentration[93]. More recently, Gnanaprakasa *et al* reported the detection of the HipO gene from *Campylobacter jejuni* which is a significant cause of human bacterial gastroenteritis, affecting more than 24 million people annually. [94]. This group reports instrument sensitivity on the order of 2.5 nM, which is 2-fold better than the 5.0 nM detection limits reported by dotLab™.

#### *Dual Polarization:*

Dual polarization interferometry (DPI) is an analytical technique that can probe molecular scale layers adsorbed to the surface of a waveguide by using the evanescent wave of a laser beam confined to the waveguide. It is typically used to measure the conformational change in proteins, or other biomolecules,

as they function. This technique utilizes two waveguides, a sample and reference waveguide, which are stacked, so they can be illuminated by a single laser with the resultant light exiting the waveguides forming a two dimensional interference pattern in the far field (Figure 1.4).

In DPI, the polarization of the laser is rotated to alternately excite two polarization modes of the waveguides: transverse electric (TE) and transverse magnetic (TM). The absolute effective refractive index of a waveguide mode is found by solving the equations of electromagnetism for a system of uniform multiple dielectric. The parameters required to solve the equations are the refractive index and thickness of each layer for each of the two allowed states of polarization. Provided the input information is complete, an effective refractive index value for each mode is obtained. If a new layer is introduced to (or removed from) the system it will alter the effective refractive index of the mode. For each of the two polarization states, the new effective refractive index can satisfy a continuous range of thickness and refractive index values for the new layer. However, there will only be one unique combination that satisfies the effective refractive index of both the TE and TM modes simultaneously. By rapidly switching the polarization and using a flow-through system to introduce samples, real-time measurements of chemical reactions taking place on a chip surface can be made. These measurements can be used to infer conformational information about the molecular interactions taking place, as the molecule size (from the layer thickness) and the fold density (from the RI) change.

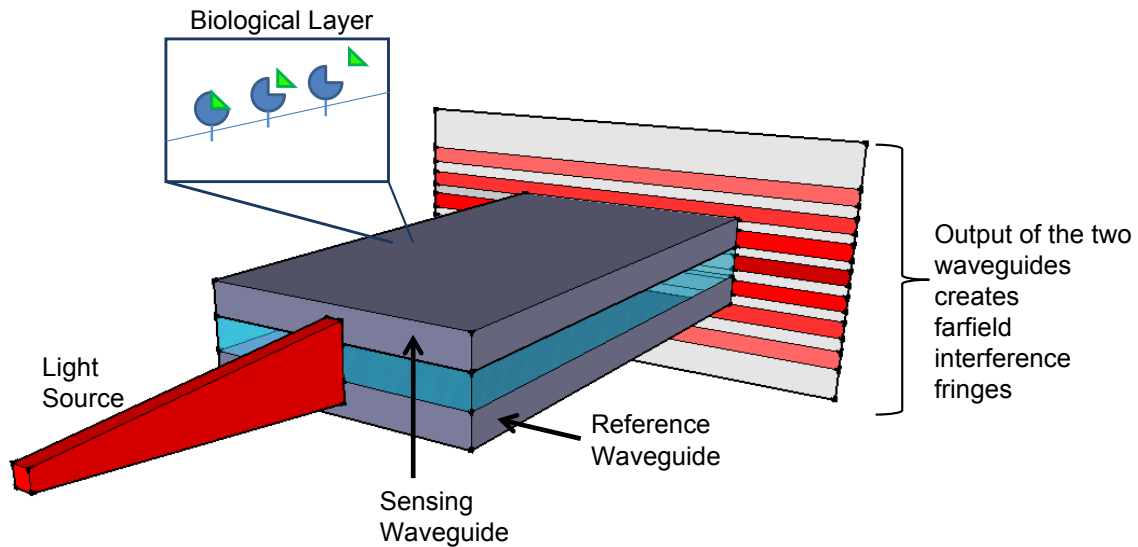


**Figure 1.4:** Block diagram of a dual polarization interferometer (DPI)

Swann *et al.* measured the binding and surface loading of streptavidin to the biotin-functionalized surface of their DPI to monitor nonspecific binding, thickness, and density changes of protein layers as well as other structural aspects of the streptavidin biotin system[95]. In 2011, Lee *et al* characterized peptide-induced changes in biomembrane structures[96]. In 2012, Coan *et al* used DPI to differentiate between various slight conformational changes in calmodulin induced by a cohort of small-molecule inhibitors. The work noted here illustrates how DPI can be used to assess and differentiate ligands with distinct structural modes of action. Farfield Sensors, Ltd has been commercializing DPI-based biosensing systems since 2000 with the introduction of the AnaLight® 250, and has most recently released the AnaLight® 4D which enables the measurement of structural changes within lipid bilayers[97, 98].

### *Biolayer Interferometry:*

Biolayer interferometry is a label-free technology for measuring biomolecular interactions. It is an optical analytical technique that analyzes the interference pattern of white light reflected from two surfaces: a layer of immobilized protein on the biosensor tip, and an internal reference layer (Figure 1.5). Any change in the number of molecules bound to the biosensor tip causes a shift in the interference pattern that can be measured in real-time. The binding between a ligand immobilized on the biosensor tip surface and an analyte in solution produces an increase in optical thickness at the biosensor tip, which results in a wavelength shift,  $\Delta\lambda$ , which is a direct measure of the change in thickness of the biological layer. Interactions are measured in real time by continuously monitoring the relative intensity of each wavelength that is reflected back through the sensor and to the detector, providing the ability to monitor binding specificity, rates of association and dissociation, or concentration. Because signal transduction takes place at the sensor surface, only molecules binding to or dissociating from the biosensor can shift the interference pattern and generate a response profile. Therefore, unbound molecules, changes in the refractive index of the surrounding medium, or changes in flow rate do not affect the interference pattern. This is a unique characteristic of bio-layer interferometry and extends its capability to perform in crude samples used in applications for protein-protein interactions, quantitation, affinity[99], and kinetics[100]. Recently, Jian Li et al used BLI in the detection of low-affinity anti-drug antibodies, leading to improved drug tolerance in immunogenicity testing [101].

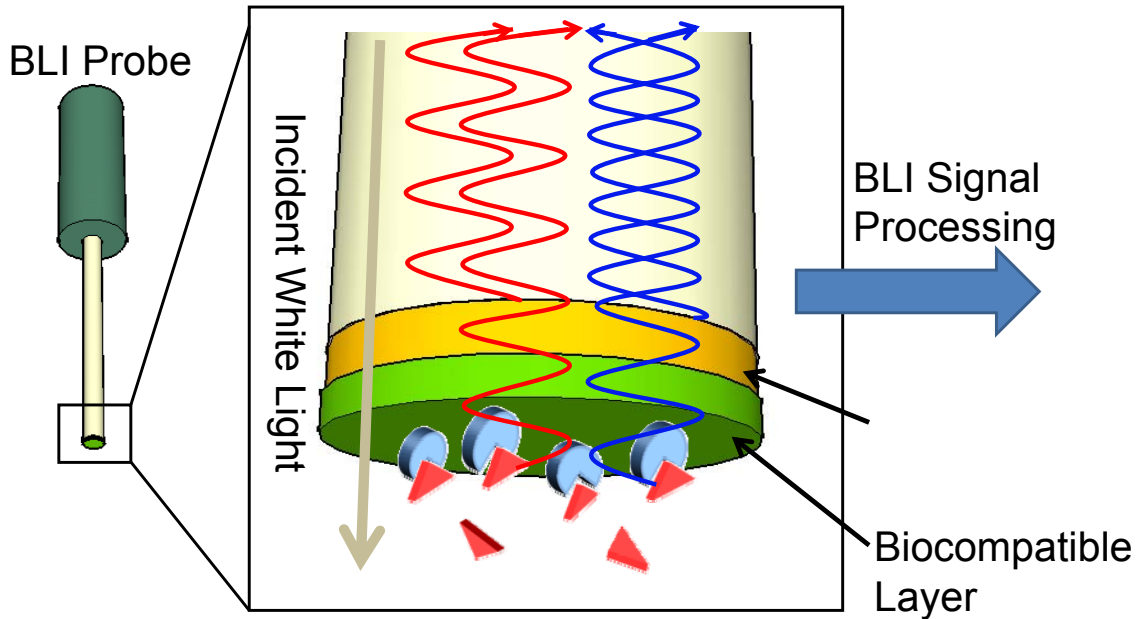


**Figure 1.5:** Block diagram of biolayer interferometer (BLI)

*Backscattering Interferometry:*

The subject of this dissertation, backscattering interferometry (BSI), was originally used to measure small refractive index changes in fused-silica capillaries[102] and has been developed in multiple configurations and for a wide array of applications, including as a highly sensitive universal solute detector in capillary electrophoresis,[103-105] as a non-invasive nanoliter temperature probe,[103, 106] a highly accurate flow sensor, [103, 104] as well as an ultrasensitive method for the detection of proteins[2, 6, 107-109]. BSI has more recently been employed to study molecular interactions label-free [2, 3, 6, 71] and has proven to be a versatile sensing technique. BSI is unique in that it can be used to investigate binding events in both a surface immobilized format (heterogeneous) and in free-solution. In fact, free-solution operation sets BSI

apart in the crowded arena of 'biosensors'. Not only does free-solution operation eliminate the time and monetary costs related to immobilization strategies, but also allows allowing binding partners to be monitored entirely in their native state. Furthermore, BSI has been shown to be compatible with complex matrices, negating the need for matrix purification and widens the scope of utility. Because BSI can be operated in either free-solution or surface-immobilized formats, any contribution of immobilization to binding perturbation may be measured directly[2, 52].

Despite the platform's unmatched versatility, BSI is an extremely simple optical train, requiring only a collimated coherent light source, a capillary or microfluidic chip (hemispherical or rectangular), and a detector. In the most common configuration of BSI, a microfluidic chip with a channel etched in glass is employed as the sample holder and the optics. BSI utilizes a red helium-neon (HeNe) laser ( $\lambda = 632.8 \text{ nm}$ ) to illuminate the chip in a simple optical train (Figure 1.6) consisting of a source, object and transducer. Specifically, the laser is coupled to a collimating lens through a single-mode fiber, producing a  $420 \text{ }\mu\text{m}$  diameter beam and a probe volume in the low nanoliter range. When the laser beam impinges the chip with the channel it reflects and refracts from the surfaces, interacts with the fluid contained in the channel, and the rays from the various light object and sample interactions produces a set of high contrast interference fringes. These fringes are monitored in a direct back-scatter configuration and at relatively shallow angles. If all other properties are held constant, (input beam position, temperature, etc.) the intensity distribution of

these fringes depends upon the refractive index (RI) of the fluid within the channel (Figure 1.6). Upon changing the solution in the channel, the spatial position of the fringes shift, which is monitored using a CCD array in combination with Fourier analysis,[110]. The fast Fourier transform (FFT) analysis enables the quantification of this positional shift as a change in spatial phase, calculated in the Fourier domain. Calibration of the system is accomplished by quantifying the phase change for standard solutions and building a response curve for this fringe shift vs. concentration.

Though BSI is one of the most sensitive RI detectors ever developed [110], there are certain challenges that must be overcome before it can have a major impact on measurement science. The high sensitivity of BSI that allows  $10^{-7}$  RI detection limits also makes BSI very susceptible to noise due to

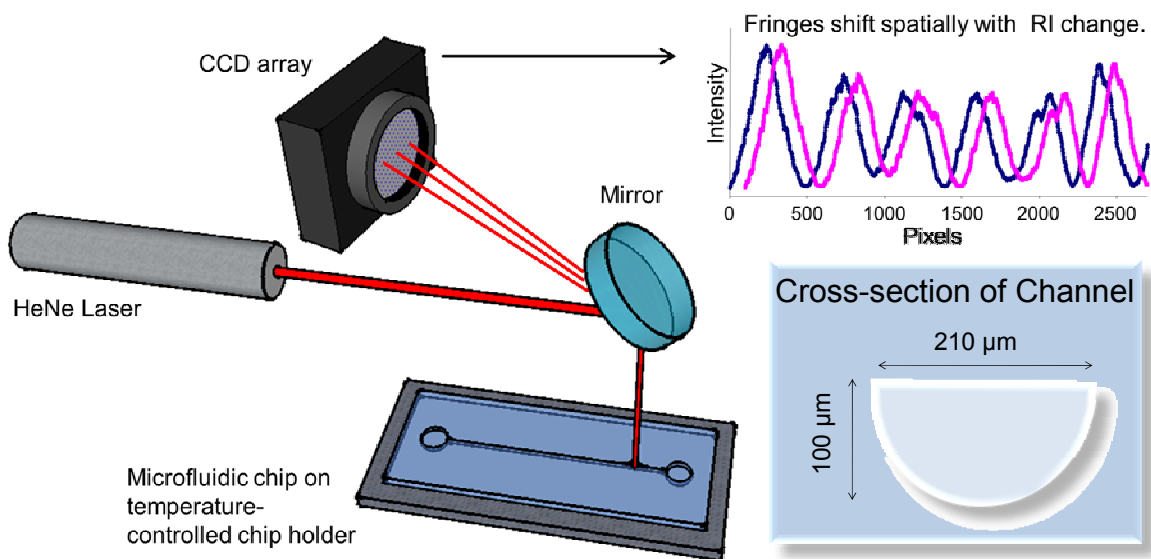


**Figure 1.6:** Block diagram of Backscattering Interferometer (BSI)

mechanical vibrations, laser pointing instability and small changes in temperature and pressure. Currently, the microfluidic chip is mounted on a temperature controlled aluminum block and the instrument resides in a room with relatively good temperature control, so as to mitigate environmental noise sources, particularly those associated with temperature fluctuations. A consistent injection methodology is the best way to minimize differences in pressure acting on each sample within the channel which can be achieved through an automated injection valve. By affixing the instrument to a high quality vibrationally isolated breadboard and a single-mode fiber coupler on the laser source, noise due to mechanical and laser pointing instabilities can be minimized. Furthermore, employing a fast Fourier transform algorithm that interrogates multiple fringes for allows for consistent and somewhat filtered signal transduction. However, the integration of an internal reference, described in chapter 7 and recommended for future instrument designs can significantly minimize the impact on performance by most sources of noise.

To make a binding affinity determination a thermodynamic equilibrium measurement is made by constructing a saturation isotherm plot [111]. Typically, a group of sample aliquots containing a constant concentration of one of the binding partners (receptor) are each mixed with a constant volume of increasing concentrations of the other binding partner (ligand) and allowed to reach equilibrium before being measured by BSI. A series of blanks, reference solutions and/or controls are also prepared to allow for corrections in signal due to changes in the bulk RI and non-specific binding signals. A typical reference



contains increasing concentrations of the ligand of interest in the absence of receptor. Once the solutions are prepared, the BSI measurement is performed by introducing each sample into the microfluidic chip sequentially and allowing the system to reach chemical equilibrium before recording the signal for 15 s. The difference between the phase change for the binding pair and the blank serves as the binding signal. A saturation isotherm is generated by taking this value and plotting it versus the respective concentrations of the ligand. A control assay must be performed to insure the signal is due to a specific molecular interaction. A series of controls are typically prepared to account for factors such as cross-reactivity and non-specific binding. A typical negative control series contains the ligand of interest incubated with an appropriate non-binding receptor to determine the level of non-specific binding in a particular system. A typical positive control consists of a ligand incubated with a well-established receptor that has previously been shown to bind.

Originally, BSI facilitated interaction assays in the heterogeneous mode, depending on the immobilization of one binding partner onto the surface of a microfluidic chip molded in PDMS[76, 107]. In early experiments, streptavidin was immobilized onto the channel surface and the fringe pattern was measured before and after introducing biotin into the channel. A good correlation was found between the BSI molecular interaction signal and fluorescence signal reported in a similar experiment. Next, a biotinylated protein-A (PA) surface allowed the monitoring of reversible IgG-PA interactions with femtomole detection limits[107]. New surface chemistry enabled a two-fold improvement on detection limits of the

protein A-IgG interaction without the use of a fluorescent label, and also allowed monitoring of the hybridization of complimentary strain of DNA at concentrations ranging from 5nM to 500 mM to a 30-mer of mActin. Assuming 100% surface coverage, the  $3\sigma$  limit of quantification was found to be 36 attamoles of DNA in the 500 pL detection volume. Further experiments showed that a 3 base pair mismatch could be detected, evidenced by a marked decrease in binding signal from that of the original complimentary strand – only 7 % of the signal generated by the binding of the complimentary strands was observed for the mismatched strand[76]. Here I report a broad range of unique applications uniquely enabled by BSI.

The first is the quantification of surface attachment perturbations to binding affinity can be measured by BSI. One of the novel aspects of BSI is that it can be used to measure free-solution as well as surface-immobilized molecular interactions. In other words the impact on the binding event due to immobilization can be quantified. Though it is very common for free-solution techniques to generally yield much lower binding affinity values (i.e. higher dissociation constant) than surface-immobilized techniques measuring the same system, little if any work has been done to uncover the reason behind this phenomenon. We report for the first time the systematic study of the effect of distance from a glass surface on binding affinity values (Chapter 2).

The second application covered in this dissertation and one of particular interest to the biosensing/diagnostics community is the quantification of aptamer-protein and aptamer-small molecule binding (Chapter 3), This research shows

the promise of using aptamers as an alternative to antibody-based disease detection and therapeutics, which commonly illicit an immune response, while highlighting the unique signal transduction mechanism of BSI which is changes in conformation and hydration upon the formation of a new chemical species (the result of binding). Because of their many benefits, and in light of the fact that certain seminal patents have recently expired, aptamers are now playing a significantly increased role in aspects of science where antibodies dominated.

A prime area of BSI investigation reported here is the implementation of BSI for use in viral disease detection (Chapter 4). Current methods for the detection of viral diseases, include cell cultures, ELISA (enzyme-linked immunosorbent assays), nucleic acid amplification tests (PCR and LCR), and direct immunofluorescence (DIF). These methods often require the patient samples to be sent off to a lab for analysis, which may take several days. This procedure causes a delay in treatment and, in some instances, the patient does not even return for treatment. The lack of a rapid test often results in the empirical use of antibiotics, which may be prescribed to a patient in error. If a method were available to accurately diagnose a disease in the doctor's office instead of having to send it off to a lab, the correct treatment could begin immediately. To test the applicability of BSI for disease diagnosis and therapy monitoring, respiratory syncytial virus (RSV), a common infection among children and the elderly, will be used as an example of BSI as a low-resource, quantitative real-time diagnostic device with competitive limits of detection.

Another important area of human-health research is in early cancer detection. Chapter 5 shows that the limits of quantification of BSI for lung cancer biomarker detection has been expanded into the picomolar range, many fold lower than current ELISA methodologies. Probably more importantly, through the study of the interaction between galectin-7 and cyfra 21-1 and their respective antibodies it is shown that BSI has the potential to speed biomarker validation. In the early stages of cancer, both of these protein biomarkers are present at levels far below ELISA detection limits, though well within the detection limits of BSI.

Chapter 6 shows BSI is also uniquely applicable to the study of mechanism of action for membrane bound neural receptors. Membrane-associated receptors are integral components of many cellular processes and disease pathogeneses. Direct and quantitative observations of ligand-protein interactions are notoriously difficult to perform due to the associated membrane and the instability of the protein when it removed from the membrane. Though assays exist to examine this class of molecular interactions (cell-adhesion assay, membrane protein microarrays, SPR)[112-114], targets of interest must typically undergo covalent modification and removal from the native membrane environment prior to observation. Here BSI will be used to observe the binding of non-native ligands to the CXCL12 receptor CXCR4, which was previously thought impossible. These studies show that not only do non-native ligands bind the receptor, but they are agents for allosteric modulation.

An improved embodiment of BSI was explored (Chapter 7), that capitalizes on a strategy to interrogate both the sample and reference solutions simultaneously. The goals of these efforts were to enhance sensitivity or S/N, increase throughput with the eye toward multiplexing while making BSI more robust and easy to use.

## CHAPTER 2

### COMPARISON OF FREE-SOLUTION AND SURFACE-IMMOBILIZED MOLECULAR INTERACTIONS USING A SINGLE PLATFORM

#### 2.1 Introduction

Quantification of the binding affinity, often expressed as a dissociation constant ( $K_d$ ), of biomolecular interactions is of broad interest to the scientific community. The determination of these values plays a pivotal role in determining mechanism of action for biological systems, must be quantified in the process of developing a diagnostic, and is central to the drug discovery process. The study of carbohydrate-lectin interactions spans a multitude of disciplines, from virology and neuroscience to glycomics and immunology[115-117]. In neuroscience, a kidney bean lectin PHA-L is used to trace the path of efferent axons[115]. Purified lectins can be used in biorecognition[116], such as blood typing, because various glycolipids and glycoproteins on an individual's red blood cells bind specifically to certain lectins. These principles of biorecognition can be applied to various diseases and have been used for *in vitro* inhibition of HIV-1[117]. Here we chose Concanavalin A (ConA) as a test system to compare solution-phase and surface immobilization binding assays because of its physiological importance and well-documented binding properties with various carbohydrates [5, 75, 118, 119]

Label-free techniques are becoming more widely accepted, yet with the exclusion of isothermal titration calorimetry (ITC), the measurement of a

biomolecular binding has historically required use of a reporter label[120, 121] or the necessity to tether one of the binding partners to the sensor surface[59, 122, 123]. Even though there is a question as to the degree of impact, it is generally recognized that the use of a label or surface immobilization perturbs the binding system[124-129]. These reports provided valuable insights, but it remains a difficult task to quantify the extent of perturbation due to labeling or immobilization because, in most cases, the interaction system cannot be studied in the presence *and* absence of the modification using the same experimental apparatus. Therefore it is somewhat problematic to determine if the differences in binding affinity have resulted from the label/tether or from the apparatus. Recently, we reported that the impact on DNA hybridization by fluorophore or immobilization can be quantified by a using BSI[52]. Here we expand on these observations, investigating the impact of tethering on binding affinity in the more challenging carbohydrate-lectin binding system.

With the exception of cell-based assays, the most commonly used label-free technologies employed today for biomolecular interaction measurements are ITC, surface plasmon resonance (SPR) and biolayer interferometry (BLI). ITC is capable of making label-free measurements in free-solution[66], but has relatively poor mass and concentration sensitivity and typically requires sample volumes that negate its use in many research endeavors, particularly those involving determinations on rare or precious samples[66]. SPR has gained considerable commercial success and boasts considerably lower limits of detection than ITC[130], but it requires one of the species to be tethered to the

surface, adding chemical complexity to the assay. Also, SPR is inherently mass sensitive and limited to interrogation at distances of a few hundred nanometers from the surface. While some researchers have found ways around these limitations[55, 63, 131], it remains a challenge to quantify interactions between a large molecule, such as ConA, tethered to the surface, and a small molecule, such as mannose or glucose, in solution.

Interferometric techniques have been used to measure molecular interactions and exhibit some advantages over SPR[73]. For example the Biolayer Interferometer (BLI) is a label-free device that can be used to perform specific protein quantitation, kinetics, and affinity analyses[55, 101, 132], and does not rely on large changes in mass for signal generation. The bench-top BLI only requires 4  $\mu$ L of sample[133] and functions by analyzing the interference pattern of white light reflected from two surfaces: a layer of immobilized protein on the biosensor tip, and an internal reference layer[133]. While valuable, BLI still requires one of the interacting species to be immobilized.

Backscattering Interferometry (BSI) is a relatively new label-free device which is unique in the capability to measure molecular interactions either in free-solution or in a tethered format[75, 111, 134]. To our knowledge BSI is the only label-free technique that allows for a direct comparison of the two measurements by performing both determinations on a single platform[52].

Quantifying the impact of surface immobilization is critical to effective drug development, disease diagnosis and mechanism of action studies, where *in vitro* surface-based interactions must ultimately be correlated with those occurring in



free-solution *in vivo* free-solution. Given ours and others results[135, 136] it is not surprising that the benchmark molecular interaction tools, ITC and SPR, commonly report a dissociation constant ( $K_d$ ) that differs by more than an order of magnitude[137].

ITC and SPR have been used in the past to study Con-A – sugar binding[66, 119] though ITC typically requires relatively large volumes of sample (1 mL of 100  $\mu$ M to 1 mM carbohydrate and 2 mL of 10 to 100  $\mu$ M lectin)[66] to elicit a quantifiable response and SPR requires that the carbohydrate be immobilized on the surface so that binding of the larger lectin can be detected[119, 138, 139]. Here we show that BSI can provide important information regarding how carbohydrate-lectin interaction studies are impacted by assay modality. For the first time, we quantified the affinity for this important system on the same platform, BSI, in both free-solution and with the 106 kDa lectin immobilized to the surface. As part of this study, we used BSI to quantify the binding affinity of monovalent carbohydrates to ConA without the use of reporter labels, in free-solution and using 8.5 ng of the protein in a 40 nL probe volume.

## **2.2 Methods**

### **2.2.1 Surface Immobilization Procedures**

The surface chemistry described herein (Appendix A, Figure 1) is well established and has previously been described in detail[52, 75, 140]. All reagents were obtained from Sigma Aldrich (St. Louis, MO) with the exception of

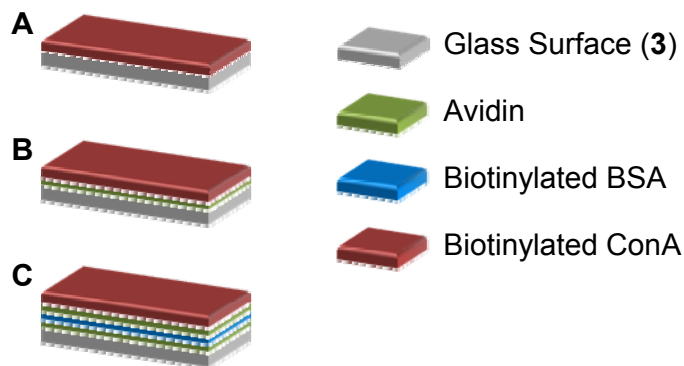


Figure 2.1: Biotinylated ConA immobilized on an ester-activated glass slide at various distances from the surface using (A) direct immobilization, (B) a single avidin spacer or (C) a multi-layer avidin/biotin-BSA/avidin spacer. [2]

biotinylated bovine serum albumin (Thermo Scientific, Rockford, IL) and carbohydrates (Arcos Organics, Geel, Belgium) Briefly, the surface of the channel was activated by cleansing with 10% potassium hydroxide (KOH) in methanol for 30 minutes (Surface 1). Then, mercaptopropyltriethoxysilane (MEPTES) was introduced for 1 hour, yielding a thiol-modified surface (Surface 2). Introduction of the bifunctional linker *N*-( $\gamma$ -maleimidobutyryloxy)succinimide ester (GMBS) for 30 minutes provided surface-tethered *N*-hydroxysuccinimide ester groups (Surface 3). Surface 3 was then used to capture the target protein through the binding of surface amine groups to the protein exterior during an overnight incubation at 3°C.

For the direct immobilization binding experiment (Figure 2.1A), ConA was introduced into the channel with Surface 3 under conditions in which it is expected to be a tetramer and incubated for 8 hours at 3°C. The channel was then rinsed thoroughly with sodium acetate buffer (pH 7.5) and the binding experiments were performed.

For the single-spacer experiment (Figure 2.1B), Surface 3 was incubated with avidin for 8 hours at 3°C, followed by one hour incubation with biotinylated ConA at room temperature to complete the surface modification.

For the triple-spacer experiment (Figure 2.1C), a layer of avidin was first introduced into the channel with Surface 3 and incubated for 8 hours at 3°C. BSA was immobilized in lieu of biotinylated ConA; the BSA acted as an inactive spacer layer. Next, a second layer of avidin was immobilized by binding to the additional biotin groups on the surface of the BSA for 8 hours at 3°C. Finally, biotinylated ConA was introduced into the channel under conditions in which it is expected to be a tetramer and incubated for one hour at room temperature.

### **2.2.2 Surface Characterization**

The thickness of each surface chemistry layer was measured using a Digital Instruments Multimode SPM tapping mode atomic force microscope (AFM) with uncoated silicon tip, where a glass slide containing two distinct regions was characterized in a single scan. One region of the slide contained the avidin-based surface chemistry of interest while the second region with Surface 3 (Appendix A, Figure 1) was used as a reference. The initial surface chemistry was carried out by sequentially submerging an entire 1 cm<sup>2</sup> silicon dioxide slide in KOH, MEPTES, and GMBS for 30 minutes, 60 minutes, and 30 minutes respectively, resulting in surface 3 as described above. Then, the slide was halfway submerged into a solution of avidin for the single-spacer setup, or subsequent solutions of avidin, biotin-BSA, and avidin for the triple-spacer setup

as described in the surface immobilization procedures section above. The AFM needle, with a 300 kHz resonant frequency, 40 N/m force constant, and 125  $\mu\text{m}$  cantilever length, was scanned perpendicularly to the border between the ester-activated glass and the adsorbed protein, covering an area of 50  $\mu\text{m}^2$ .

### **2.2.3 Immobilized Assay Procedures**

Once lectin immobilization was complete, a series of carbohydrate concentrations (0-100  $\mu\text{M}$ ) were sequentially introduced into the channel. Mannose and glucose were used due to their known binding properties to ConA. Galactose was used as a negative control[5]. For a given concentration, the sample was introduced into the channel and allowed to reach binding equilibrium for 15 seconds; then the BSI signal was recorded for 15 seconds. After the binding signal of each concentration of sugar was measured, the channel was rinsed with buffer until the signal returned to baseline, assuring that all carbohydrates from the previous sample were removed. Only then was the next concentration of carbohydrate measured. To compensate for changes in signal due to bulk RI changes, a series of blanks (carbohydrate in buffer) were measured in the absence of any surface chemistry. A saturation isotherm was generated by taking the difference between the binding signal and the signal of the blank.

## **2.2.4 Free-solution Assay Procedures**

The free-solution assay was carried out in an end-point format, where a series of vessels containing a constant concentration of biotinylated lectin (2  $\mu\text{M}$ ) mixed with increasing concentrations of carbohydrate (0-100  $\mu\text{M}$ ) were incubated at 3°C overnight, allowing the samples to reach equilibrium before being measured by BSI. A series of blanks were prepared containing increasing concentrations of the carbohydrate (0-100  $\mu\text{M}$ ) in the absence of lectin to allow for corrections in signal due to changes in the bulk RI. The BSI measurement was performed by introducing each sample into the microfluidic chip sequentially and allowing the system to reach equilibrium before recording the signal for 15 seconds. The difference between the phase change for the binding pair and the blank serves as the binding signal. A saturation isotherm was generated by taking this value and plotting it versus the respective concentrations of the ligand (carbohydrate).

## **2.3 Results and Discussion**

### **2.3.1 Free-solution Measurement**

In the past, we showed that it is possible to measure binding affinity of carbohydrates to lectins, even when the large or high molecular weight species is immobilized to the surface[75]. Here we show for the first time that BSI can be used to measure these biologically important molecular interactions in free-solution. Figure 2.2 shows the saturation isotherm produced by BSI for mannose, glucose, and galactose (non-binding control) binding to ConA.

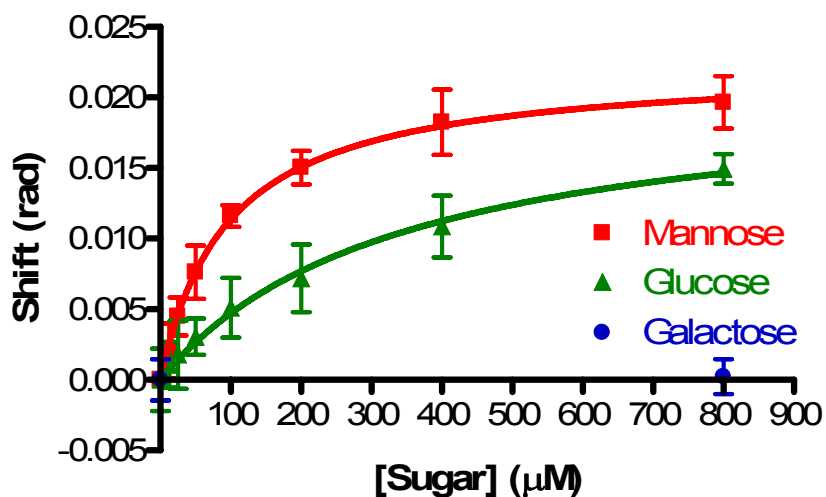


Figure 2.2: Mannose and glucose bind to ConA in free-solution with  $K_D$  values of  $96 \pm 4 \mu\text{M}$  and  $344 \pm 43 \mu\text{M}$ , respectively. Galactose, which does not bind ConA, is used as a negative control.[2]

Dissociation constant ( $K_d$ ) values were calculated to be of  $96 \pm 4 \mu\text{M}$  (mannose) and  $344 \pm 43 \mu\text{M}$  (glucose), with single-site rise to exponential plots having correlation coefficients of  $r^2 = 0.9988$  and  $0.9946$ , respectively. Compared to  $K_d$  values obtained by ITC ( $92 \mu\text{M}$  and  $290 \mu\text{M}$  for mannose and glucose) [4] the values from BSI compare favorably, and both methods give similar relative affinities, or  $K_d$  ratios between the two carbohydrates of 3.5 for BSI and 3.2 for ITC.

To our knowledge, ITC is the only other methodology which can perform such an assay in a label-free and free-solution format[141]. While ConA is not a precious target, there are numerous other lectins where it would be advantageous to perform the assay rapidly and with less than 40 picomoles total protein for the entire assay, as shown here, rather than with ITC which is time consuming and requires 40-2500 times more sample.

### **2.3.2 Surface vs. Free-solution: How tether distance impacts measured affinity for Concanavalin A**

ConA plays a key role in many biological processes, such interactions with immunoglobulins[142] and colorectal cancer biomarkers[143]. Because such in-vivo processes occur in solution (i.e. blood stream), we set out to understand how presentation environment, tethered or not, as well as how the tether linker length influences the binding affinity quantified by BSI. To do so we prepared chips with ConA attached directly and at varying distances from the channel surface depending on the number of avidin layers employed. Then we evaluated the binding affinity of these ConA systems to three carbohydrates, mannose, glucose and galactose.

For the surface-tethered experiments, ConA was immobilized directly to the surface (Figure 2.1A), slightly less than 10nm (Figure 2.1B) and twice that distance or about 20 nm (Figure 1C) from the surface. A starting distance of 7 nm from the surface was chosen because it is similar to the distance commonly used for SPR measurements of ConA[125, 144]. Two common methods to approximate a solution-phase binding environment with SPR are to attach either a biotin-avidin or poly(ethylene glycol) (PEG) linker to the surface[125, 145].

The thickness of the surface chemistry layers was evaluated using tapping-mode AFM where the tip was scanned across a section of an ester-activated silicon dioxide slide containing adjacent regions with the ConA immobilized according to our chip preparation procedure and a reference region

that had no surface modifications. As shown in Figure 2.3 we obtained excellent contrast between the two regions making it possible to quantify the thickness of the immobilized protein layers. Taking the difference in height between the two regions allowed the calculation of the thickness of the linker layer. For the single layer of avidin, as shown in Figure 2.3A, we obtained a value of  $7.17 \pm 1.08$  nm. Upon analysis of the multilayer motif samples containing avidin/biotinylated BSA/avidin (Figure 2.3B) we obtain an average height or thickness value of  $20.35 \pm 1.19$  nm. Relatively uniform coverage is indicated from the analysis and these values compare well to the expected layer thickness based on previously reported calculations which estimate the monolayer thickness of avidin and biotin each to be on the order of 7 nm[146].

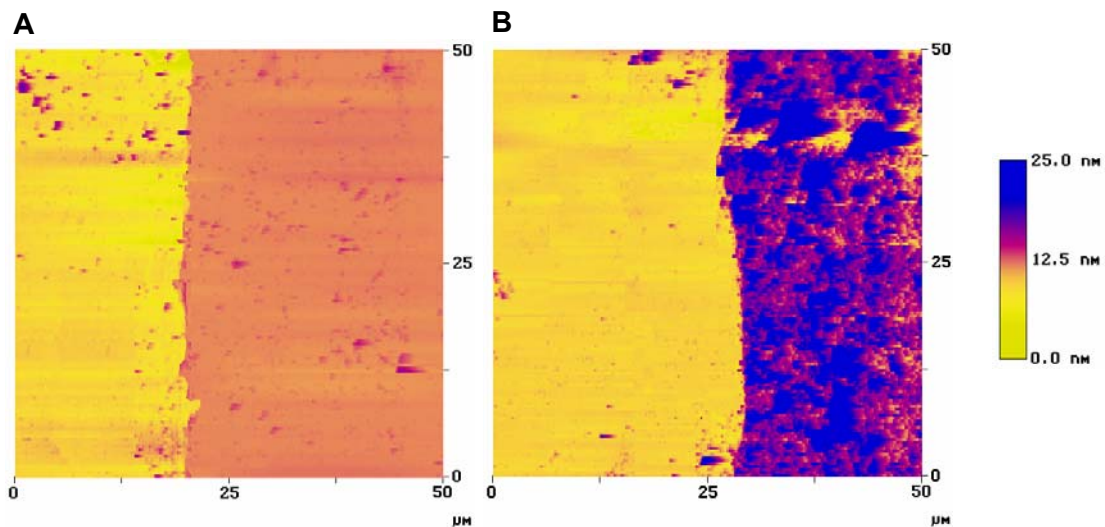


Figure 2.3: Tapping-mode AFM characterization of (A) a single layer of avidin, which was  $7.17 \pm 1.08$  nm thick and (B) multi-layer avidin/biotin surface chemistry which was  $20.35 \pm 1.19$  nm thick.[2]



First, it is illustrative to observe the impact of surface-tethering on affinity. When ConA was immobilized directly on the microfluidic channel (0 nm from the surface), the apparent Langmuir adsorption coefficient ( $K_{\text{ads}}$ ) calculated from the binding curve depicted in Appendix A, Figure 2A for mannose was  $6.76 \pm 0.29 \times 10^4 \text{ M}^{-1}$  ( $1/K_{\text{ads}} = 14.8 \pm 2.5 \text{ }\mu\text{M}$ ) whereas that of glucose was  $2.42 \pm 0.87 \times 10^4 \text{ M}^{-1}$  ( $1/K_{\text{ads}} = 41.4 \pm 14.8 \text{ }\mu\text{M}$ ). Note that as expected, the non-binding species galactose shows negligible signal throughout the concentration region tested (0 to 100  $\mu\text{M}$ ). While the absolute binding affinity was found to be lower (higher affinity) than the value typically reported in the literature, the ratio of binding affinities is 3:1 for the two carbohydrates, which is consistent with findings from other investigations[60, 75]. Next, we extended the ConA away from the surface by immobilizing it to the top of a single avidin layer and performed the binding assay with the same three carbohydrates (Appendix A, Figure 2B). Interestingly, at a distance of  $7.17 \pm 1.08 \text{ nm}$  from the channel surface, the ConA bound to mannose and glucose with  $1/K_{\text{ads}}$  values of  $48.5 \pm 4.5 \text{ }\mu\text{M}$  and  $145.4 \pm 43.0 \text{ }\mu\text{M}$  respectively. We are quite confident in the validity of these values, given that we previously reported the affinity for mannose to be  $41.8 \pm 5.4 \text{ }\mu\text{M}$  and  $155 \pm 88 \text{ }\mu\text{M}$  for glucose using BSI with the same chemical immobilization strategy.[75] It is also noteworthy that these determinations were performed nearly three years ago, on a different BSI instrument of the same design and by an entirely different user.

While the ratio of the affinity between mannose and glucose remains relatively constant at about 3, there is a significant increase in the  $1/K_{\text{ads}}$  values

for both ligands when they are tethered about 7 nm from the surface. This shift to lower affinity is not surprising considering that others have observed immobilization processes, when lacking fluidic characteristics, can often lead to an apparent affinity that is many orders of magnitude greater than free-solution ITC results[4, 75, 119]. To investigate this phenomenon further we immobilized ConA atop of two avidin layers that were separated by a layer of biotinylated BSA. As confirmed by tapping AFM, this tethering approach placed the ConA a distance of  $20.35 \pm 1.19$  nm from the surface. Given the literature on the impact of binding affinity on fluidity[4, 118] it was reasoned that immobilizing the lectin in such a manner, as we have here, would result in an environment that is closer to that of free-solution than with the single layer chemistry. As anticipated, the  $1/K_{ads}$  moved toward a value that approaches that of the free-solution determination, with an increase to  $57.7 \pm 5.0$   $\mu\text{M}$  for mannose and  $240.7 \pm 66.9$   $\mu\text{M}$  for glucose (Appendix A, Figure 2C). As noted above, in the free-solution experiment performed here, mannose and glucose bound to ConA with dissociation constant ( $K_d$ ) of  $96 \pm 4$   $\mu\text{M}$  and  $344 \pm 43$   $\mu\text{M}$ , for mannose and glucose respectively (Figure 2.2). Generally, a dissociation constant is calculated for free-solution interactions and Langmuir adsorption coefficient is calculated for surface binding, though when surface-based binding occurs on a monolayer, the two equations are assumed to be equivalent. Taken together with the fact that we used the same instrument (even the same chip) for the measurements, we can compare our tethered and free-solution studies to quantify the impact of immobilization. The results of our experiments are

Table 2.1: Summary of affinities with respect to distance from surface [2]

Distance of ConA from Surface (nm)	1/K <sub>ads</sub> (μM)		
	Mannose	Glucose	Galactose
0	14.8 ± 2.5 μM (92-200 μM)[4, 5]	41.4 ± 14.8 μM (lit. = 290 μM) [4]	No Binding
7.17 ± 1.08	48.5 ± 4.5 μM	145.4 ± 43.0 μM	No Binding
20.35 ± 1.19	57.7 ± 5.0 μM	240.7 ± 66.9 μM	No Binding
Free-solution	96 ± 4 μM (lit. = 90-470 μM)[11, 12]	344 ± 43 μM (lit. = 330-1800 μM)[11, 12]	No Binding

summarized in Table 2.1 and Figure 2.4, showing an interesting trend in the binding affinity as a function of distance from the channel surface. As the ConA is immobilized in a way which separates it from the surface the result is a significant decrease in binding affinity with lowest values being those obtained in free-solution.

It has previously been seen that 1/K<sub>ads</sub> values are lower than free-solution K<sub>d</sub> measurements[4, 75]. We postulate that as the receptor is moved closer to the channel wall, the surface adhesion effect is increased, resulting in an increase in the apparent binding affinity. The surface adhesion effects are due to the surface activity of proteins and their tendency to non-specifically bind to surfaces[147-149]. This effect is mitigated the farther the protein is from the surface, because the more fluid surrounds the protein, limiting the effects of solid-liquid interface adsorption[147, 150-152]. Furthermore, previous studies have shown that the conformation of adsorbed proteins varies depending upon

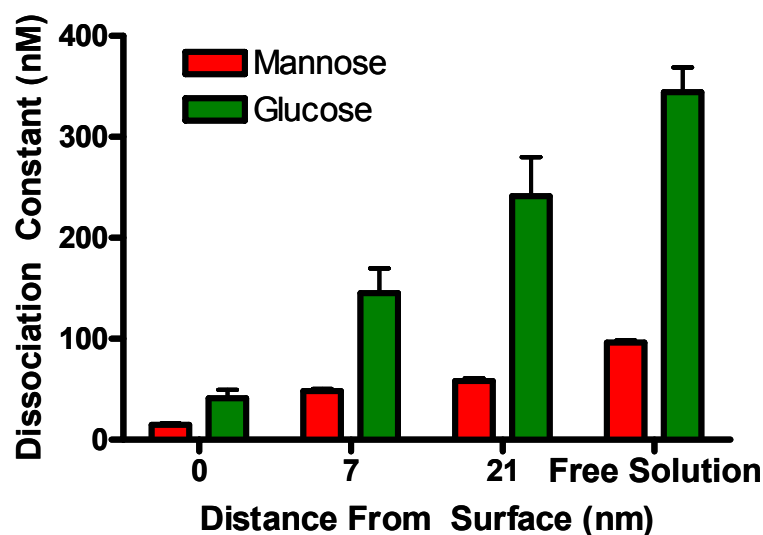


Figure 2.4: Comparison of  $1/K_{ads}$  vs. distance from the channel surface.[2]

surface characteristics, such as hydrophobicity,[149] which would certainly affect the binding affinity. Surface adhesion effects have also been reported previously for this binding pair with SPR[5]. Alternatively, it is possible that direct immobilization of ConA causes the protein to partially denature, resulting in an altered apparent binding affinity due to conformational changes at the binding site. In addition to the aforementioned distance-specific sources of binding affinity alteration, there is likely some shift in affinity that can be attributed to the attachment of biotinylated ConA to GMBS. However, we believe our relative surface-immobilized studies with respect to length still have validity toward illuminating how distance impacts these measurements.

It is important to note that although the surface-immobilized  $1/K_{ads}$  values are substantially higher than in free-solution, the relative order of affinity of each

pair of carbohydrates remains the same. These findings suggest that although the absolute  $1/K_{ads}$  values are altered in the surface-immobilized experiments, the relative binding affinities of mannose and glucose remain reasonably constant.

## **2.4 Summary and future directions**

We have shown that BSI is a unique molecular interaction assay technology allowing for the quantification of binding under significantly different physical conditions (tethered and free-solution) and that the effect of these environments influences the affinity. To our knowledge, this is the first report that shows a single platform can facilitate the direct measurement of the impact of surface immobilization on carbohydrate-lectin binding affinity.

Whether the distance, fluidity, or both are the cause of these variations is difficult to discern without a much more extensive investigation. Even so, BSI has been shown to be a simple, yet highly effective label-free, optical sensor that can rapidly report on protein binding events in both free-solution and surface-tethered modes on the same platform. BSI enables binding pairs to be rapidly screened and validated in free-solution before being subjected to time and resource intensive surface immobilization. Once immobilized, BSI quantifies how immobilization changes the binding properties of the assay. An understanding of how protein immobilization affects binding will ultimately allow for a more complete translation between in-vivo biological processes and in-vitro diagnostic assays.

The ability of BSI to measure molecular interactions at various distances from the surface will help to build a better understanding of how the fringe pattern is created, and whether particular fringes (and frequencies) within the pattern report or signal certain regions within the channel. For example, if a region of the fringe pattern and/or frequency can be identified that does not produce a signal from the channel surface, sources of noise due to undesirable analyte adsorption to the walls during a free-solution binding event can be mitigated. Additionally, if the BSI signal that arises due to changes at the channel surface is concentrated in a particular region of the fringes, interrogation of that region will allow for higher sensitivity for surface-immobilized assays.

This work was published in *Analytical Chemistry* in 2012[10]:

## CHAPTER 3

### PROBING ALLOSTERIC APTAMER-PROTEIN INTERACTIONS WITH BACKSCATTERING INTERFEROMETRY

#### 3.1 Aptamers as potential therapeutics

Multivalent binding interactions form the foundation of many important biological functions found in nature. For example, ethanol binds to the allosteric site of GABA<sub>A</sub> and glycine receptors[153] to up-regulate activity, while influenza viruses exploit multivalent protein-carbohydrate interactions to enter host cells. Multivalent binding is also critical for *in vitro* molecular diagnostics, and [154]the most widely used methods, such as the enzyme-linked immunosorbent assay (ELISA) and its variants,[155, 156] are “sandwich” assays that target multiple epitopes to achieve specific detection of analytes.

The capability to accurately measure multivalent binding interactions is important for diverse biotechnological applications, and numerous analytical methods have been developed along these lines. For example, few mode fiber surface plasmon resonance (FMF-SPR) and planar optical waveguides[157, 158] are useful for the capture and detection of cancer biomarkers in a sandwich assay format, while lipid bilayer sensors[157] enable measurement of multivalent interactions between antibodies and membranes. Though powerful, the above methods require either chemical labeling of the target or surface immobilization of affinity reagents, which can alter the characteristics of molecular interactions[52,

159]. Thus, there remains an urgent need for a label-free analytical measurement technique that can measure binding reactions in solution.

In this chapter the capability to rapidly screen multivalent aptamer-target binding in a manner that could aid in the development of reagents for sandwich assay methods such as ELISA is demonstrated. This rapid assay is performed with small quantities of analyte in free-solution, without any labeling or tethering, by simply forming aptamer-protein complexes and then measuring the binding affinity for a second aptamer using BSI. As a model, we have applied this technique to measure the binding of human  $\alpha$ -thrombin by a pair of well-characterized aptamers (Bock[7, 160] & Tasset[9, 161]) that interact with distinct regions of the protein. We found that the  $K_d$  values of each aptamer were in agreement with those found in the literature. Surprisingly, we also observed that the two aptamers exhibit allosteric effects—that is, the formation of a single aptamer-thrombin complex results in a significant change in the binding affinity of the second aptamer.

### **3.2 Methods**

All binding experiments were performed in solution without immobilization or labeling of molecules, and utilized end-point measurements as previously described[74, 77, 110, 111]. BSI assays were performed as difference measurements, with binding curves derived from a comparison of the sample signal, a blank and a control. This allows specific binding to be quantified even in the presence of a high background bulk RI. Results presented in this chapter represent the difference between the binding sample or the control sample signal



and an aptamer-only blank. Subtracting the blank allows for compensation of changes in bulk RI as the concentration is increased during the assay. The blank signal was similar in all experiments, about 0.04 radians.

The Bock aptamer (5'-GGTTGGTGTGGTTGG-3'), Tasset aptamer (5'-CAGTCCGTGGTAGGGCAGGTTGGGG TGAAGTCGTGGAA-3'), and randomized 80-mer (5'-AGCAGC ACAGAGGTCAGATG–Random[40]–CCTATGCGTGCTACCG TGAA–3') and 100-mer (5'-AGCAGCACAGAGGTCAGATG–Random[80]–CCTATGCGTGCTACCGTGAA–3') negative control sequences were synthesized by Integrated DNA Technologies (Coralville, IA). For negative control aptamer samples, each individual strand contained a unique, randomized sequence. Human  $\alpha$ -thrombin was purchased from Haematologic Technologies, Inc. (Essex Junction, VT). All other chemicals were obtained through Sigma-Aldrich (St. Louis, MO). We used a 50 mM tris(hydroxymethyl)aminomethane (TRIS) buffer (pH 7.5) containing 100 mM NaCl and 1 mM  $MgCl_2$  for all dilutions. Each aptamer was denatured at 100 °C for 10 minutes, rapidly cooled in an ice bath for 10 minutes and finally allowed to reach room temperature. We incubated 2 nM thrombin at 10 °C overnight with aptamers prepared at a range of concentrations (0-800 nM) by serial dilution. After incubation, we brought the samples to room temperature over a 30 minute period prior to BSI analysis.

### 3.3 Results

#### 3.3.1 BSI Measurement of equilibrium binding constants of aptamers

We measured the binding affinity of Bock and Tasset aptamers for thrombin in solution using an end-point assay[111]. As negative controls, we used random DNA sequences that were 80 and 100 nucleotides in length. For the BSI measurement, we drew 1  $\mu$ L of the aptamer-thrombin sample into the microfluidic channel. We then stopped the flow and collected 30 seconds of fringe position data for each aptamer concentration, after which we eluted the sample and repeated the process for increasing aptamer concentrations. To minimize possible measurement errors arising from long-term drift of the instrument, we performed the entire assay sequentially in triplicate. To do so, we first ran the control and/or blank solutions in order of ascending concentration, and then evaluated the binding pair for the same series of ligand concentrations. This dataset constitutes an entire, single determination of  $K_d$ . This procedure was repeated three times to generate the binding curves displayed in Figure 3.1. Since the assay is performed

Table 3.1: Comparison of aptamer-thrombin binding affinities obtained using BSI[6]

<b>Binding Species</b>	<b><math>K_d</math> (Literature)</b>	<b><math>K_d</math> (BSI)</b>
Bock - Thrombin	1.4 – 6.2 nM <sup>[7, 8]</sup>	5.96 $\pm$ 0.57 nM
Bock –Tasset Complex	Not Available	0.87 $\pm$ 0.18 nM
Tasset – Thrombin	0.5 – 1.0 nM <sup>[9]</sup>	3.84 $\pm$ 0.68 nM
Tasset – Bock Complex	Not Available	1.9 $\pm$ 0.2 nM
Aptamer – Self Complex	Not Available	Negligible Binding

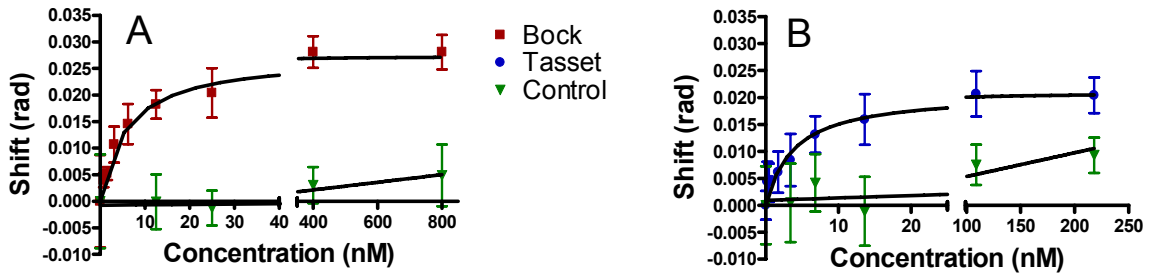


Figure 3.1. Measurement of dissociation binding constants of aptamers to thrombin using the single channel BSI setup: (A) Bock aptamer binding to thrombin shows a  $K_d$  value of  $5.96 \pm 0.57$  nM and  $B_{MAX} = 0.027$  radians; (B) Tasset aptamer binding to thrombin yielded a  $K_d$  value of  $3.84 \pm 0.68$  nM and  $B_{MAX} = 0.021$  radians; Error bars on all plots were derived from three independent experiments. Control data were generated using random 80-mer and 100-mer sequences for plots A and B respectively.[6]

in this manner, the error bars seen on the binding curves represent the assay reproducibility of the method, and are thus a conservative estimate of binding affinity.

Using Graphpad Prism software and a single site binding fit, we determined  $K_d$  values for Bock and Tasset aptamers to be  $5.96 \pm 0.57$  nM and  $3.84 \pm 0.68$  nM, respectively. These values compare reasonably well to literature values of 1.4–6.2 nM for Bock[4, 8, 160] and 0.5–1.0 nM for Tasset[9] (Table 3.1). It is well established that different methods can yield a range of  $K_d$  values, and the slight discrepancy between experimental and literature  $K_d$  values for the Tasset aptamer can most likely be attributed to the fact that literature values were generated using the fundamentally different nitrocellulose filter-binding technique.

### 3.3.2 Multivalent interactions affect exosite binding characteristics

After establishing the affinity for each aptamer, we evaluated the use of BSI to study multivalent binding interactions and explore whether allosteric interactions exist in this system. To do so, we first formed the Tasset-thrombin complex and then measured the affinity of the Bock aptamer for the complex. We formed the Tasset-thrombin complex by incubating 500 nM Tasset aptamer with 2 nM thrombin at 10 °C overnight to saturate the binding site. Then, we performed an end-point assay with increasing concentrations of Bock aptamer to obtain the binding curve (Figure 3.2A). Finally, we measured the binding affinity of the Tasset aptamer to the Bock-thrombin complex in the same manner (Figure 3.2B).

To ensure that the BSI signals originated from aptamer-thrombin interactions and not aptamer-aptamer interactions, we performed a measurement in which aptamer-thrombin complexes were formed and then incubated with increasing concentrations of the same aptamer. We reasoned that if the majority

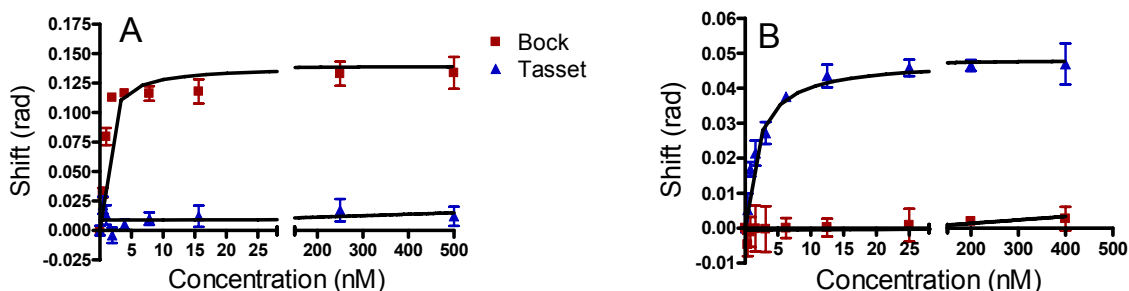


Figure 3.2: Measurement of aptamer binding to pre-formed aptamer-protein complexes: (A) Bock aptamer binding to Tasset-thrombin complexes yields a  $K_d$  value of  $0.87 \pm 0.18$  nM and  $B_{MAX} = 0.1391$  radians. Tasset does not bind Tasset-thrombin complex; (B) Tasset aptamer binding to Bock-thrombin complexes yields a  $K_d$  value of  $1.9 \pm 0.2$  nM and  $B_{MAX} = 0.048$  radians. Bock does not bind Bock-thrombin complex.[6]

of binding sites on thrombin are occupied during formation of the complex, the introduction of excess aptamers should only produce a refractive index (RI) change similar to that generated by the blank. The difference in BSI response for the aptamer complex–complementary aptamer and the blank, as measured by the slope, was approximately  $1 \times 10^{-5}$  radians for both aptamers (Figure 3.2). This level of signal is nearly three orders of magnitude lower than a typical binding signal, and is therefore considered negligible, indicating that no appreciable binding took place after formation of the complex. As noted by others [9, 162, 163], the Bock and Tasset aptamers do not bind to each other. In any case, we perform binding investigations as end-point assays, where first complex formation is allowed to progress over a relatively long incubation period (overnight) further insuring excess unbound aptamer will self-associate or become unreactive to other aptamers[162]. Once the thrombin-single aptamer complex is formed we introduce the second denatured aptamer which is allowed to bind to the second thrombin exosite.

Fitting these curves to a single site binding analysis, we measured the  $K_d$  of Tasset aptamer binding to the Bock-thrombin complex to be  $1.9 \pm 0.2$  nM. Similarly, we measured the  $K_d$  of Bock aptamer binding to the Tasset-thrombin complex to be  $0.87 \pm 0.18$  nM. These  $K_d$  values are considerably lower (indicating higher affinity) than for the individual aptamer-thrombin measurements, as summarized in Table 3.1.

### **3.3.3 Computational structural modeling**

To explain these apparent allosteric interactions, we created a computational model using the AMBER 10 and RosettaDock programs as described in Appendix B. The model suggests that the binding sites of the two aptamers, which reside at opposite ends of the substrate-binding cleft, may be connected by a framework of rigid secondary-structural elements. While preliminary, these results are in reasonable agreement with similar studies that have found evidence for allosteric linkage between exosites I and II using fluorescently-labeled hirudin and a prothrombin fragment[163].

### **3.4 Summary and future directions**

In this work, we report the first use of BSI to measure the binding interactions among multiple DNA aptamers to a protein in solution. As a means of calibration, we first confirmed that the  $K_d$  values obtained with BSI for the Bock and Tasset aptamers against human  $\alpha$ -thrombin are in reasonable agreement with those reported in the literature. Importantly, when we preformed the Tasset-thrombin complex, we observed a seven-fold increase in Bock aptamer affinity for this complex compared to binding to thrombin alone. Similarly, we observed a two-fold increase in affinity for Tasset aptamer binding to Bock-thrombin complex compared to thrombin alone. As negative controls, we verified that the Tasset and Bock aptamers have negligible binding to Tasset-thrombin and Bock-thrombin complexes, respectively. Although we have not conclusively identified the origin of this phenomenon, our preliminary modeling efforts suggest that a rigid secondary

structure framework contributes to allosteric linkage between exosites 1 and 2, as has been observed with other species[163].

We have demonstrated the capability to measure binding interactions of multiple aptamer ligands with a single target in solution without labels using BSI. Using this work as a foundation for allosteric interaction characterization, future work will focus on studying other binding systems such as ion channels and G-protein coupled receptors (GPCR). GPCRs are extremely valuable in medicine, yet their function and cross reactivity with non-native ligands is far from being fully understood. In order to increase the sensitivity and reproducibility of multivalent measurements, we are currently optimizing the technique to maximize the signal difference arising from changes in conformation, waters of hydration and/or charge density produced by the binding events.

This research has also expanded the mechanistic understanding of BSI signal generation and will be useful in designing multi-probe biomarker detection assays that use structural modifications as a way to optimize binding signal and improved detection limits. I believe that advances in quantifying allostery and using BSI for quantification will be beneficial in many areas of bioanalytical technology, especially with regard to assay design and optimization for molecular diagnostics.

This work was published in *Analytical Chemistry* in 2011[6].

## CHAPTER 4

### THE EFFECT OF HYBRIDIZATION-INDUCED SECONDARY STRUCTURE ON RNA DETECTION USING BACKSCATTERING INTERFEROMETRY

#### 4.1 Introduction

The expression of single-stranded RNA is an essential part of the life cycle of human pathogens. RNA is found in great abundance during critical stages of infection. Some virus infections produce  $10^3$ – $10^4$  detectable RNA molecules per virion [164, 165]. Additionally, a high degree of pathogen specificity can be found in sequences of expressed RNA. Pathogen species and strains can be identified based solely on the detection of RNA sequences as short as 16 nt [166, 167]. Because of their abundance and species-specificity, RNA biomarkers are especially useful for pathogen detection and diagnosis of illnesses that result from pathogen infection. We have developed an interferometric method for RNA detection that is based on specific interactions with unlabeled oligonucleotide probes in solution. Many methods have been developed to detect RNA biomarkers. Reverse transcription followed by polymerase chain reaction (RT-PCR) is a common technique used to quantify RNA. Because of its sensitivity, it has become the gold standard for RNA detection. PCR-based methods, however, typically require purification, denaturation, and time consuming amplification and labeling. Fluorescence based methods, such as microarrays or molecular beacons, are also commonly used for detecting RNA targets using oligonucleotide probes [168, 169], yet they often lack the sensitivity needed for



diagnostic applications. Other nucleic acid probe-based methods developed for RNA detection include the biobarcode-assay[168], cantilever array sensors[170] and surface plasmon resonance (SPR)[171]. These methods require complex probe synthesis procedures, nucleic acid labeling or immobilization, or specialized instrumentation and are deficient in terms of speed, sensitivity, convenience and/or cost. There is, therefore, a need for methods that are simple, rapid and sensitive for RNA detection. Backscattering interferometry (BSI) is a technology that circumvents the limitations of other detection methods as it has a simple instrumental design, does not require molecular labeling or amplification, and can be performed in solution using microliter volumes in complex matrices. BSI has been used to successfully monitor binding interactions of a variety of biological molecules with high sensitivity[6, 52, 70, 71, 73, 74, 76]. Though BSI has been used to quantify protein biomarkers via antibody–antigen interactions[74], the work presented here represents the first report of its use for detecting and quantifying RNA biomarkers.

Nucleic acid probes of various lengths and chemical compositions can be designed to complement any sequence of a target nucleic acid; therefore, the design space of nucleic acid probes is extremely large compared to other types of probes, such as antibody-antigen or even aptamer–ligand interactions, which require specific and constrained tertiary structures for target recognition. Additionally, commercial synthesis of oligonucleotides is widely available and is able to produce virtually any sequence of natural or chemically modified nucleotides. Compared to other biomolecular probes (e.g. antibodies), nucleic

acids also have relatively modest chemical complexity and are uniformly charged. These properties reduce variations in RI that may result from the interactions of the probes with the solvent, making them ideal probes for biomarker detection using BSI. Furthermore, nucleic acids are not 'sticky' like proteins, reducing artificial signals from non-specific interactions, such as binding to the channel wall. An important property of BSI in the context of biomarker detection is its large dynamic range. The optical properties of the interferometer are such that the fringes continue to shift (i.e. produce a signal) as long as a change in RI occurs and that the RI of the fluid differs from that of the microfluidic chip. Consequently, the dynamic range of BSI can be expanded as long as there are analytes available to bind and change the RI. BSI sensitivity can therefore be dramatically enhanced without reaching signal saturation. This property is in contrast to detection assays that are dependent on light intensity, in which photometers can become saturated with extreme amplification methodologies. Oligonucleotide probes that are designed to produce the maximum change in RI upon binding the RNA target will, therefore, provide maximum BSI signal and optimize sensitivity. In this report, we have investigated the utility of BSI for label-free detection of a specific viral RNA biomarker sequence in solution. We focus on the respiratory syncytial virus (RSV) nucleocapsid (N) gene RNA, a biomarker with which our laboratories have had considerable experience[164, 172, 173]. A systematic evaluation of a subset of oligonucleotide probe design parameters was conducted to determine interactions and characteristics of nucleic acid probes that enhance the sensitivity of BSI for detecting this RNA biomarker.

## **4.2 Materials and methods**

### **4.2.1 Preparation of the synthetic RNA target**

The RNA target used in these studies is a synthetic ~1300 nt positive-sense RNA molecule of the RSV strain A2 N gene. The RNA was prepared as previously described[164]. Briefly, a pGBKT7 vector containing the RSV N gene insert was amplified in *Escherichia coli* strain DH5a, purified using a Qiagen Plasmid Midi Kit, linearized with the BssHIII restriction enzyme, reverse transcribed using the Ambion T7MEGAscript transcription kit, and treated with DNase I. The integrity and length of the RNA product was confirmed using denaturing agarose gel electrophoresis. Aliquots of the RNA were stored at a concentration of ~80nM in Tris-EDTA buffer at -80°C until they were used. The RNA mismatch targets used in these studies were commercially synthesized at a 50 nmole scale and desalted by Sigma-Aldrich. The sequences of the full-length RNA target and the mismatch targets used in these studies are provided in Appendix C.

### **4.2.2 Synthesis of the oligonucleotide probes**

The DNA oligonucleotide probes used in these studies were commercially synthesized at a 200 nmole scale by Sigma-Aldrich and purified using reverse phase cartridge purification. Locked nucleic acid (LNA) oligonucleotide probes were synthesized at a 250 nmole scale by Exiqon and purified with high performance liquid chromatography. Each lyophilized oligonucleotide was resuspended to a concentration of ~100 mM in molecular grade water (Fisher)

and stored at -20°C until they were used. The sequence of each oligonucleotide probe used in these studies is provided in Appendix C, Table 1.

#### **4.2.3 Quantification of relative nucleic acid hybridization**

The relative amount of nucleic acid hybridization was quantified using a SYBR Green assay. Samples were prepared in triplicate with 1nM of the synthetic RSV N gene RNA, 10nM of the probe or probes, and a 1:9000 dilution of SYBR Green I (Life Technologies). Samples for the blank measurements were prepared in triplicate without RNA or without the DNA probes. For the LNA:RNA and DNA:RNA hybridization comparison, samples were prepared in triplicate using 60nM LNA or DNA, 20nM RNA complement of the same length, and a 1:9000 dilution of SYBR Green I (Life Technologies). A standard curve of double-stranded DNA of the same sequence and length was used to approximate the percent hybridization in the LNA:RNA and DNA:RNA samples. Prior to the addition of SYBR Green I, each sample was heated to 90°C for 5 min and cooled slowly to room temperature over the course of 1 h. Fluorescence measurements were recorded using a BioTek Synergy H4 Hybrid 96-well plate reader using an excitation wavelength of 497nm and a detection wavelength of 520 nm. The values were normalized by subtracting signal of the samples from the background signal generated in the RNA-alone or the DNA-alone blank samples.

#### **4.2.4 Preparation and evaluation of surrogate nasal wash samples**

HEp-2 cell lysates were prepared in a manner previously described [164]. Briefly, cells were cultured to a confluent monolayer in a cell culture flask, harvested and resuspended in a cell lysis/RNA preservation solution (4M

guanidinium thiocyanate, 25mM sodium citrate [pH 7.0] 0.5% N-lauroylsarcosine [Sarkosyl], 0.1M 2-mercaptoethanol), and stored at -80°C. The surrogate nasal wash samples were prepared by diluting the cell lysates into phosphate buffered saline at  $1 \times 10^5$ ,  $5 \times 10^4$ ,  $1 \times 10^4$  and 0 cells/ml concentrations and spiking each with the synthetic ~1300 nt RSV N gene RNA biomarker at a final concentration of ~16 nM. For evaluation of the RNA target in the surrogate nasal wash samples using BSI, the samples were split into two halves. One half of each sample was used for total RNA extraction, and the other half was left unextracted. Total RNA extraction was performed using a self-contained continuous tubing extraction cassette as previously described[164]. Briefly, each sample was added to an RNA binding solution containing silica-coated magnetic beads. The beads were mixed with the sample for 5 min and then drawn through a series of RNA extraction solutions. Total RNA was eluted into water, and quantification of the synthetic ~1300 nt RSV N gene RNA biomarker was performed using BSI. To validate the BSI results, quantitative reverse-transcription polymerase chain reaction (qRT-PCR) was performed on the same sample set. Each sample was extracted and evaluated in triplicate for BSI and qRT-PCR determinations. qRT-PCR was performed as described previously [164].

#### **4.2.5 RNA folding analysis**

The folding state of the synthetic RSV N gene RNA was predicted using the RNA Folding Form of the mfold software package available online

(<http://mfold.rna.albany.edu/?q=mfold/RNA-Folding-Form>). The full length sequence of the target (1331 nt, sequence available in Appendix C, Figure 1) was used as the input, and the default settings were used. The five structures predicted to have the lowest energy were used to identify the folding state at the probe binding sequences. The number of consecutive unpaired bases for each of these sequences were averaged from the five predicted structures and plotted against the slope of the linear range of the BSI response curve. The five lowest energy mfold RNA folding structures are provided in Appendix C, Figure 2.

#### **4.2.6 Nucleic acid secondary structure determination**

Circular dichroism (CD) spectra were collected using an Aviv CD spectrometer model 215 (Aviv Biomedical, Inc.). To compare the LNA:RNA, DNA:RNA and DNA:DNA hybrids, solutions were prepared in 40 ml volumes Nucleic Acids Research, 2013 3 Downloaded from <http://nar.oxfordjournals.org/> at Vanderbilt University - Massey Law Library on April 8, 2013 containing 30 mM of DNA, RNA and/or LNA strands in Tris-buffered saline. Prior to collecting CD spectra, each sample was heated to 90°C for 5 min and cooled slowly to room temperature over the course of 1 h. For the A-form to B-form transition study, a solution of 80% 2,2,2-Trifluoroethanol (TFE) containing 385 mM Tris-HCl, 38.5 mM EDTA, 5mM NaCl and 12 mM of each DNA strand was prepared. Prior to adding the TFE, the solution was heated to 90°C for 5 min and cooled slowly to room temperature over the course of 1 h. TFE was added stepwise accompanied by immediate mixing to avoid DNA precipitation while transitioning to A-form DNA.

The concentration of TFE was diluted to 77.5, 75, 72.5 and 70% to by adding the appropriate volumes of a solution containing 385 mM Tris-HCl, 38.5 EDTA, 5mM NaCl and 12 mM of each DNA strand. At each TFE concentration, 60 ml of the sample was removed and CD and BSI measurements were immediately performed. Blank measurements were collected from solutions prepared at each TFE concentration and containing 385 mM Tris-HCl, 38.5 EDTA and 5mM NaCl, with no DNA. All CD spectra were collected from 320nm to 200nm wavelengths at 25.0°C in a 1.0mm path length quartz cuvette using a 0.5nm wavelength step, a 1.0nm bandwidth, and a 1 s averaging time. Spectra were averaged from at least three separate scans, smoothed and normalized using CD-215 software version 2.90 provided by the manufacturer.

## **4.3 Results**

### **4.3.1 Enhanced BSI sensitivity using 22-mer probe length**

The design space of oligonucleotide probes targeting the ~1300 nt RSV N gene RNA biomarker sequence is extremely large. Oligonucleotides of virtually any length and sequence complementary to the target could be used, and a variety of chemically modified nucleotides could be substituted for natural nucleotides. Because an exhaustive study of all the potential probe designs is not feasible, we conducted a systematic evaluation of a subset of oligonucleotide probe design parameters. The first probe investigated was RSVN(242–263), a 22-mer DNA probe with a sequence chosen based on previous success as a primer for PCR studies aimed at amplifying RSV N gene cDNA. BSI

measurements using the RSVN(242–263) 22-mer probe produced a linear response proportional to the concentration of the RSV N gene RNA with a LOD of 3.73nM target RNA (Figure 4.1A and Table 4.1). As a negative control, a scrambled sequence of the same 22-mer was evaluated under the same conditions and yielded negligible signal. Postulating that probe length would impact BSI signal, probes RSVN(242–256), RSVN(242–285) and RSVN(242–329) were tested, which are 15, 44 and 88 nt in length, respectively, and start from the same position in the target RNA as the 22-mer probe. Each of these probe lengths resulted in slightly less signal and poorer detection limits than the 22-mer probe. To relate the BSI signal to a net increase in base pairs, the relative hybridization of these probes to the RNA target was determined using a SYBR Green assay (Figure 4.1B). The signal generated from the intercalation of SYBR Green dye in the 15-mer, 44-mer and 88-mer probe:target hybrids was

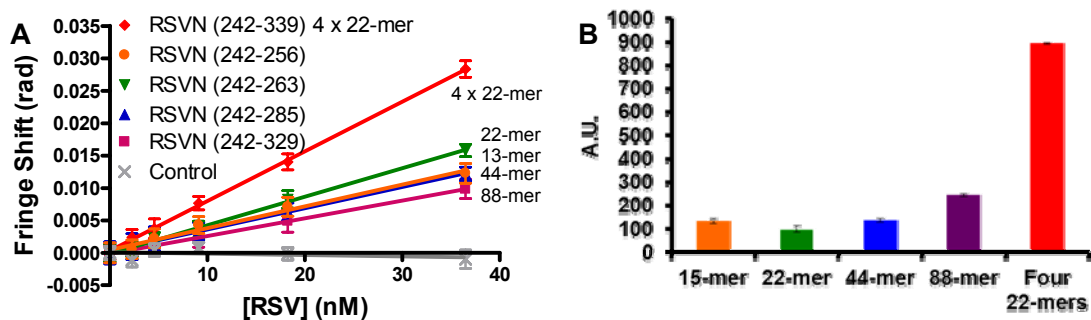


Figure 4.1. Comparison of the BSI binding response and net hybridization upon adding the 15-mer, 22-mer, 44-mer, 88-mer or four consecutive 22-mer DNA probes to the RNA target. (A) The probe length that produces optimal BSI signal is 22nt. Four short 22-mer DNA probes have improved signal over one 88-mer spanning the same target sequence. A scrambled negative control sequence produced negligible signal. (B) Net hybridization of the four consecutive 22-mers is significantly greater than any of the four probe lengths.[3]



slightly greater than that of the 22-mer probe:target hybrid. Interestingly, we discovered that by dividing the 88-mer probe into four contiguous 22-mer probes, the slope of the BSI response was significantly increased, resulting in a LOD of 2.04nM target RNA, or  $\sim 4.1 \times 10^5$  molecules. This enhancement in sensitivity was reflected by the increase in the net hybridization of the four consecutive 22-mers compared to the 15-mer, 22-mer, 44-mer and 88-mer probes (Figure 4.1 and Table 4.1). These results indicate that of the probes tested, the optimal length is 22 nt for BSI detection and that the BSI signal can be enhanced using multiple probes of that length.

Table 4.1 – Summary of probe:RSV assay results[3]

Probe	Slope (x 10 <sup>-5</sup> )	LOD (nM)
RSVN (242-263)	44	3.73
RSVN (242-256)	30	26.7
RSVN (242-285)	33	5.16
RSVN (242-329)	27	8.96
Four consecutive DNA probes	77	2.04
Four Distributed DNA probes	250	2.54
Nine distributed DNA probes	627	0.624
RSVN (264-285)	246	5.78
RSVN (286-307)	25	68.35
RSVN (308-329)	359	4.52
RSVN (1070-1091)	84	15.03
RSVN (800-821)	52	35.63
RSVN (755-774)	27	146.56
RSVN (755-774) L	175	2.15
Four distributed LNA probes	349	1.05

#### 4.3.2 Enhanced BSI sensitivity using multiple distributed probes

Next we investigated the influence on assay sensitivity of distributing the probes along the ~1300 nt RNA target sequence. Because the four consecutive probes were designed to bind contiguous sequences of the target RNA, it was hypothesized that the conformation of the target RNA secondary structure prevented the probes from fully hybridizing and that distributed sequences would improve signal. By distributing the four probes along the length of the target RNA,

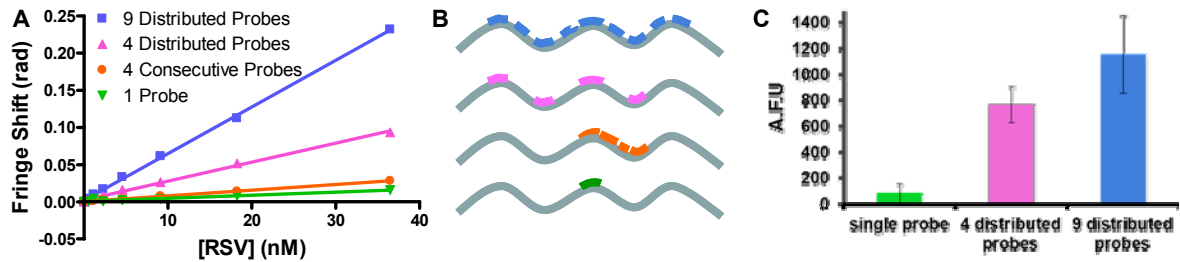


Figure 4.2. Comparison of the BSI binding response and net hybridization of various numbers and distributions of probes to the RNA target. (A) Increasing the number and distribution of distinct probes improves sensitivity. (B) Illustration of the relative positions of the DNA probes along the RNA target. (C) Hybridization studies confirm that increased number of probes bound correlates with increased binding signal.[3]

the slope of response was improved more than 3-fold over the four contiguous sequences (Figure 4.2A and Table 4.1). Furthermore, increasing the total number of probes to nine further improved sensitivity, providing a LOD of 624 pM, or  $1.5 \times 10^5$  molecules target RNA. Accordingly, studies evaluating the net hybridization of the single probe versus the four and nine probe combinations revealed increased hybridization with the increased number of probes (Figure 4.2C), further validating that BSI signal is at least partially the result of a net change in hybridization.

To further demonstrate that the increased signal from the nine-probe cocktail was a result of an increase in the number of available binding sites, as opposed to the effect of having a higher concentration of probes present, a saturation binding isotherm was constructed for both the single probe and the nine-probe cocktail. For this assay, the concentration of the target RNA was held constant while the probe concentration was varied from 0–100 nM. The signal at saturation ( $B_{max}$ ) for the single probe was 0.087 radians, whereas the signal for

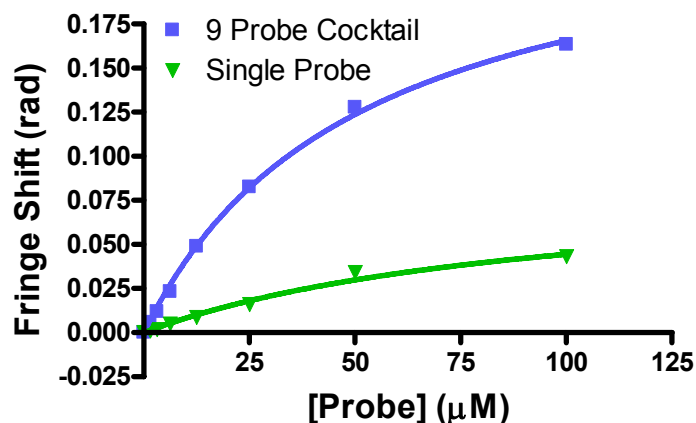


Figure 4.3. Saturation curves of target RNA incubated with either a single 22-mer probe or a mixture of nine distributed probes. The mixture of nine probes saturates at a higher level than the single probe.[3]

the nine distributed probes was 0.25 radians, a 2.9-fold overall increase in signal (Figure 4.3). This result indicates that the sensitivity improvement observed in the nine-probe system is the result of an increased number of available binding sites; therefore, a greater number of binding events can occur before target saturation is reached. This may not be surprising as BSI signal magnitude is directly related to the number of binding events [71]. These data are consistent with these previous observations and indicate that the greatest BSI sensitivity over a large dynamic range is achieved by maximizing the number of available target RNA binding sites.

#### 4.3.3 Target specificity is maintained in RNA samples extracted from complex matrices

To evaluate the specificity of BSI using the 22-mer RSVN(242–263) DNA probe, six 22-mer RNA targets containing 0, 1, 3, 5, 7 and 10 mismatched

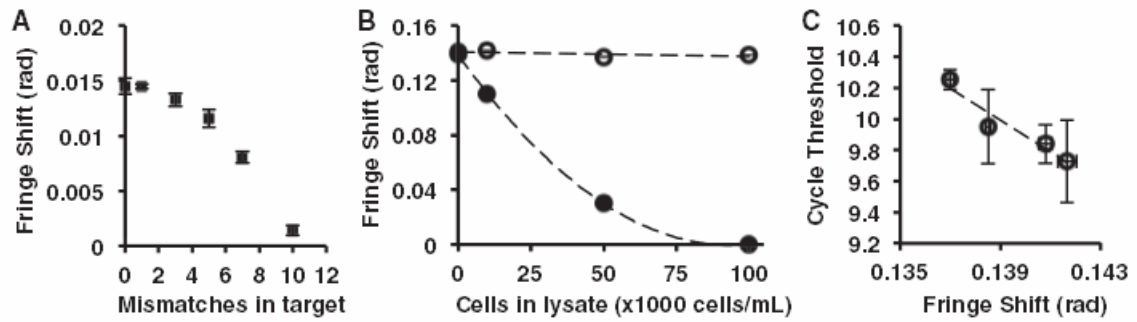


Figure 4.4. Evaluations of BSI specificity for (A) mismatched targets or (B) RNA targets in complex samples using a single 22-mer probe. (A) BSI signal drops off moderately when probing for RNA targets with increasing numbers of mismatched nucleotides. (B) BSI signal is consistent when probing for the 1300nt RNA biomarker in a sample of total RNA extracted from HEP-2 cell lysates of increasing concentrations (open circles), whereas BSI signal diminishes in unextracted samples of increasing background concentration (closed circles). (C) qRT-PCR cycle threshold values for the extracted samples correlate with the BSI fringe shift values ( $R^2 = 0.92$ ). [3]

nucleotides distributed throughout the sequence were tested in an end-point assay format (Figure 4.4A). With an increasing number of mismatched nucleotides in the target sequence, BSI signal dropped off significantly, resulting in essentially no signal using the RNA target containing 10 mismatched bases in the sequence. The signal produced using the RNA target sequences containing 1 and 3 mismatches was statistically equal to that of the 0 mismatch target ( $P=0.5$  and  $0.14$ , respectively). The signal from the targets containing 5, 7 and 10 mismatches was statistically different from the 0 mismatch control ( $P<0.05$ ).

To examine the specificity of BSI in samples containing a high background non-target molecules, we tested BSI for detecting the synthetic ~1300 nt RNA target spiked into surrogate nasal wash samples containing increasing background concentrations of HEP-2 cell lysate (Figure 4.4B). In extracted

samples (i.e. samples of total RNA isolated from the cell lysate background), the signal produced was consistent despite the increase in the total background RNA extracted from the samples. Notably, cycle threshold values of qRT-PCR analysis of the extracted RNA samples correlated strongly with the fringe shift values of BSI (Figure 4.4C), suggesting that the quantitative potential of BSI for extracted RNA biomarkers at this concentration is equivalent to qRT-PCR. In unextracted samples (i.e. samples of RNA spiked into cell lysate background), BSI signal diminished with increasing cell lysate concentration, resulting in no distinguishable signal in the highest concentration of cell lysate evaluated (Figure 4.4B). Taken together, these data suggest that BSI detection of RNA is tolerant of some mismatched nucleotides in the target sequence, yet specificity is retained in total RNA extracts from complex cell lysate samples.

#### **4.3.4 RNA target folding affects BSI binding signal**

During the process of testing a variety of oligonucleotide probe sequences, we observed that probes of similar length (i.e. 20–22 nt) and nucleotide content, but composed of different nucleotide sequences, yielded significantly disparate BSI binding responses. Because BSI sensitivity is produced in part by changes in conformation [71], we surmised that the probes were not only interacting at the primary sequence level of the target RNA (i.e. base pairing), but that probe binding signal was also impacted by the complex folding state of the RNA target. To investigate the effects of RNA target folding on BSI response, mfold software was used to predict secondary structure motifs in the regions complementary to the probes that would account for the variation

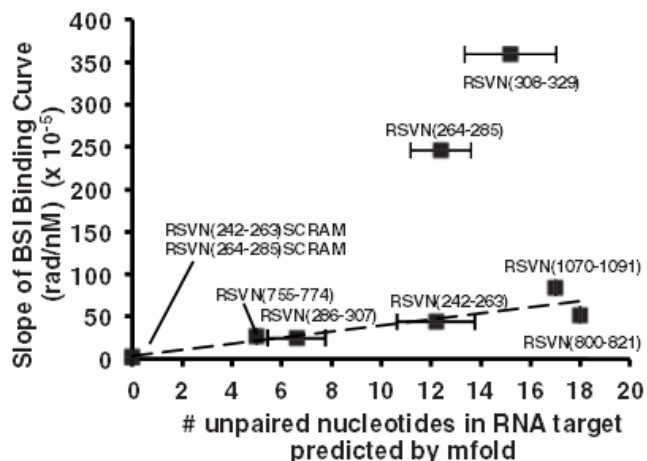


Figure 4.5. DNA probes designed to bind different regions of the RNA target generate a range of BSI binding responses. With the exception of two probes, binding response correlates positively with the number of nucleotides predicted to be unpaired in the RNA target ( $R^2=0.86$ ). x-axis values are averages of predicted unpaired nucleotides in the five lowest energy folding structures of Mfold  $\pm$  standard error.[3]

in probe binding. Specifically, the software was used to identify regions of the RNA target that are predicated to be open loops, or sequences that would be available to bind a complementary oligonucleotide probe. Although mfold cannot predict RNA folding with absolute certainty, with the exception of two probes tested, we found a positive correlation between the number of unpaired nucleotides in the open loop regions of the predicted structure of the RNA target and the BSI signal produced by the probe complementary to that sequence (Figure 4.5). In line with probe design software for microarray oligonucleotide sequences[167], probes designed to bind RNA target sequences predicted to be single-stranded would result in the greatest net change in hybridization and produce the greatest change in BSI signal. Probes RSVN(264–285) and

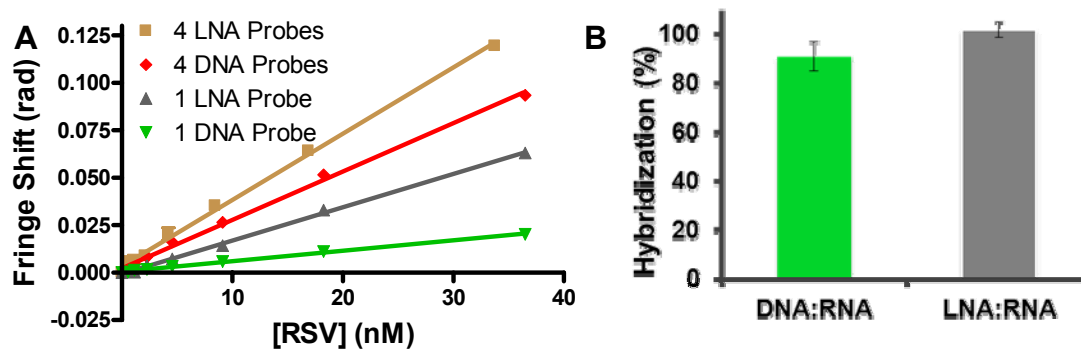


Figure 4.6. Comparison of the BSI binding response and net hybridization of LNA and DNA probes of the same sequence to target RNA. (A) LNA probes improve the BSI signal. (B) DNA:RNA hybrids and LNA:RNA hybrids produce virtually the same net hybridization. [3]

RSVN(308–329), however, produced a much higher signal that does not appear to fit this model. One possible explanation for the large signal of these probes, compared to the other probes, is that tertiary structure rearrangements or allosteric changes in the RNA target may be occurring upon probe binding. We have observed similar binding-order related signal enhancements in other systems, particularly with thrombin binding aptamers[6]. These observations cannot be fully explained due to limitations in the current model, but are under investigation.

#### 4.3.5 Enhanced BSI sensitivity using LNA probes

With some knowledge of the probe length and spacing parameters that yield good signal in BSI for optimized hybridization, we explored LNAs, a category of oligonucleotides with unique structure and binding characteristics. LNA oligonucleotides have much greater binding affinities for their targets when



compared to DNA or RNA of similar length and sequence[174]. The first LNA probe we used, RSV(242–263)L, was the same sequence and length as the 22-mer DNA probe used in our initial experiments, except that every third nucleotide in the sequence contains a methylene group bridging the 2' oxygen and the 4' carbon of the ribose ring, 'locking' the sugar into the 3'-endo conformation. With these simple structural modifications, a 4-fold improvement in sensitivity was achieved over the DNA probes, resulting in a LOD of 2.15nM of target RNA (Figure 4.6A and Table 4.1). Using a mixture of four distributed LNA probes, identical in sequence and length to the four distributed DNA probes, a LOD of 1.05nM target RNA was achieved. These results compare favorably to the 1.5-fold improvement in LOD observed when increasing the number of DNA probes from one to four (Table 4.1). Interestingly, this improvement in signal and sensitivity was not attributed to an increase in the net hybridization of the probe to the RNA target. Although the increased affinity of LNA for the RNA target would generally shift the binding equilibrium toward the bound state, both LNA and DNA probes hybridize to approximately the same number of RNA targets (Figure 4.6B). This result is likely because the LNA and DNA probes are added to the RNA target in such excess that, despite the increased affinity of LNA for the target RNA, the total number of LNA and DNA probes bound to the RNA target was nearly equivalent. Because there is not a significant increase in net hybridization when using LNA probes, we concluded that hybridization alone did not account for the 4-fold improvement in BSI signal using the LNA probe.

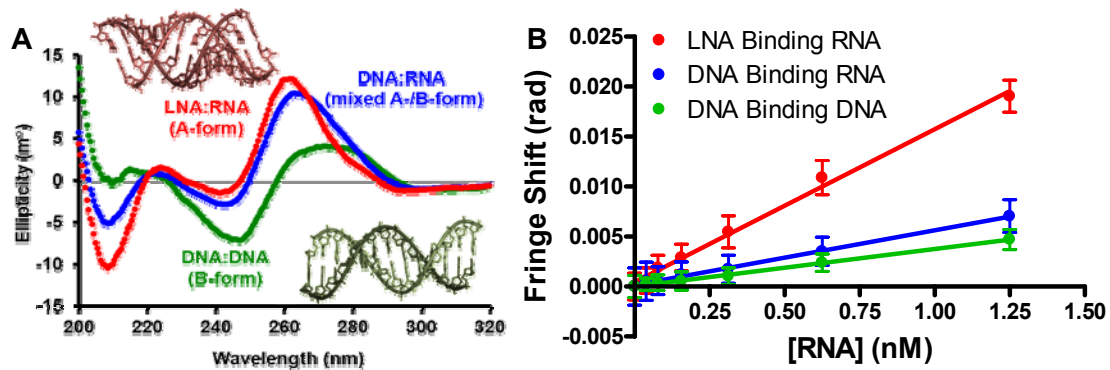


Figure 4.7. Relative degree of A-form nucleic acid character of the DNA:DNA, DNA:RNA and LNA:RNA hybrids corresponds with BSI signal. (A) The CD spectrum of the DNA:DNA duplex (green) corresponds to B-form secondary helical structure with a maximum near 280nm, a deep minimum near 250nm. LNA:RNA hybrid (red) produces a spectra corresponding to A-form secondary structure with a maximum near 270nm and a shallow minimum near 245nm. The DNA:RNA hybrid produces a spectra that is intermediate of A-form and B-form. (B) BSI binding curves of LNA:RNA, DNA:RNA and DNA:DNA.[3]

Therefore, we explored the possibility that the improvement in sensitivity was the result of the unique structural characteristics of LNA:RNA hybrid.

#### 4.3.6 Induced A-form secondary structure improves BSI sensitivity

It has been established that LNA:RNA hybrids primarily form A-form secondary helical structures, whereas DNA:RNA hybrids consist of a mixture of A-form and B-form character[175]. Since the net hybridization measured for DNA versus LNA probes binding the RNA target was approximately equivalent but the BSI signal of the LNA probes was significantly greater than that of the DNA probes (Figure 4.6A and B, respectively), we hypothesized that the induced A-form helical character of the LNA:RNA hybrid was responsible for the greater RI change upon formation compared to the DNA:RNA hybridization. Accordingly, we

evaluated nucleic acid hybrids of the same length and sequence that exhibit a range of secondary structures using CD and BSI. To reduce the background noise from the unbound regions of the ~1300 RNA target, the RNA and DNA complements used in these studies are the same length as the LNA and DNA probes (22 nt). Based on the CD spectra, we verified that the LNA:RNA hybrid resulted in a characteristic A-form secondary structure, the DNA:RNA hybrid resulted in a secondary structure consisting of a mixture of A- and B-form, and the DNA:DNA duplex resulted in a characteristic B-form secondary structure (Figure 4.7A). These same hybrids were then evaluated using BSI. The LNA:RNA interaction produced the largest RI shift ( $1.53 \times 10^{-2}$  rad/nM), followed by the DNA:RNA interaction ( $5.48 \times 10^{-3}$  rad/nM), and the DNA:DNA interaction produced the smallest RI shift ( $3.75 \times 10^{-3}$  rad/nM) (Figure 4.7B). These data indicate that the BSI signal or slope reflects the extent to which the hybridized product displays A-form secondary structure. These observations are consistent with the hypothesis that BSI signal can be maximized using oligonucleotide probes that induce the greatest net change in the nucleic acid secondary structure.

To further validate that the formation of A-form secondary structure is responsible for the observed increase in BSI signal, as opposed to the differences in the primary structures of the nucleotide subunits, we performed BSI measurements on a DNA:DNA duplex matching the sequence of the RSVN(242–263) probe at various stages of a TFE-induced B-form to A-form transition. Incubation with high concentrations of TFE is a well-established method for converting B-form secondary structure in DNA:DNA duplexes to A-

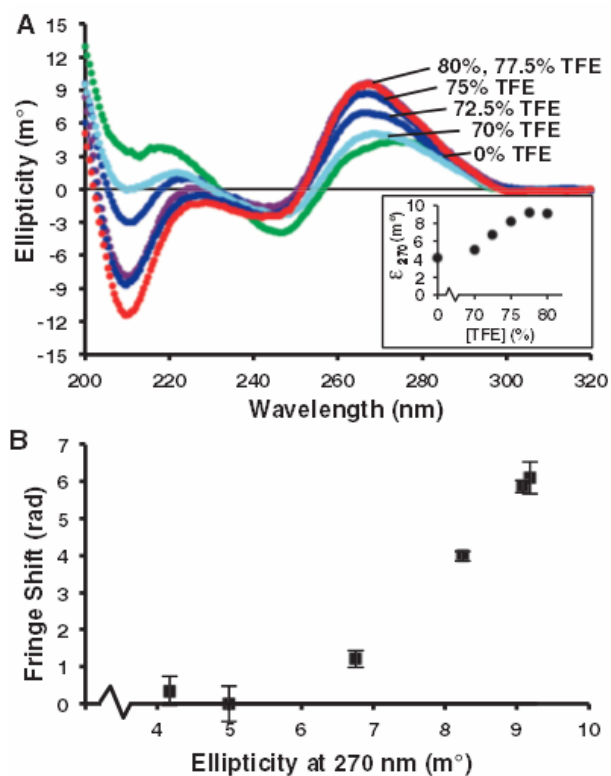


Figure 4.8. Relative degree of A-form character corresponds to increased BSI signal. (A) CD spectra of the DNA duplex demonstrate a shift from A-form to B-form structure with decreasing concentrations of TFE. Inset: A-form to B-form transition monitored at 270nm. (B) Ellipticity at 270nm correlates positively with the shift in the RI as detected by BSI.[3]

form[176, 177]. TFE was titrated into a solution containing a DNA:DNA duplex and the secondary structure transition was confirmed by CD analysis (Figure 4.8A). BSI signal magnitude increased as the DNA:DNA duplex adopted a more A-form character as monitored by the ellipticity at 270 nm. These data validate the BSI signal enhancing effect of induced alterations to the helical geometry of the nucleic acid hybrid (Figure 4.8B).

#### **4.4 Discussion**

In this study, we have demonstrated the application of BSI for the detection of a RSV N gene RNA biomarker in solution using unlabeled nucleic acid probes. These studies have shown that induced secondary structure formation is a major contributing factor to signal generation for detecting RNA with oligonucleotide probes by BSI. Several factors are important in obtaining a maximum signal to noise ratio. The number of binding events are an important factor, yet as we have previously shown with protein binding systems[71], the nature of the binding event (i.e. the resulting structure) also plays a critical role in BSI signal magnitude. The first and most obvious source of secondary structure formation is the net helical duplex formation that occurs when a nucleic acid probe hybridizes to the RNA target.

We found that the sensitivity of the assay is greatest when multiple, short probes are employed, distributed along the length of the RNA target (Figure 4.2 and Table 4.1), which results in the maximum number of binding events (Figure 3C). In comparison to a single 22-mer DNA probe which detects RNA target concentration at a sensitivity of  $4.4 \times 10^{-4}$  radians/nM (LOD=3.73 nM); four DNA

probes produce a 5.7-fold increase in sensitivity, or  $2.50 \times 10^{-3}$  radians/nM (LOD=2.54 nM); and nine DNA probes produce a 14.3-fold increase in sensitivity, or  $6.27 \times 10^{-3}$  radians/nM (LOD=624 pM) (Table 4.1). As one would expect, the increase in signal is directly proportional to the number of probes available to bind the RNA target.

Experiments aimed at studying the effects of probe length demonstrated that BSI signal magnitude was greatest using a probe length of 22 nt (Figure 4.1). Interestingly, though they contain the same number of base pairs, four contiguous 22-mer probes yield an appreciably larger signal than a single 88-mer probe. We postulate that steric hindrance resulting from the native structure of the ~1300 nt RNA target prevents the longer probe from binding as effectively as the four shorter probes. Additionally, in a multi-probe assay, it may be the case that some probes bind at a higher kinetic rate than others, altering the conformation of the target RNA and thus creating more favorable binding conditions for subsequent probes. We also found that while four short, adjacent probes create more binding signal than a single long probe, sensitivity is improved even further by distributing the probes along the length of the target. This may be explained by the potential for probes that target sequences immediately adjacent to prevent the other probes from binding because of the induced secondary structure and rigidity of the probe-bound sequences.

BSI was also effective in detecting the synthetic ~1300 RNA target from total RNA extracted from surrogate nasal wash samples of increasing background complexity (Figure 4.4B and C), demonstrating the specificity of BSI

for detecting target RNA, as the target only made up a portion of the total RNA extracted from the sample. In contrast, when using unextracted samples, BSI signal diminished with increasing background cell lysate concentration. We hypothesize that the complex bimolecular content present in unextracted cell lysate samples has a signal-suppressing effect on BSI as a result of aggregate non-specific interactions. These results demonstrate the potential for BSI to be used as a diagnostic tool for quantifying specific RNA biomarker sequences that have been extracted from complex samples. Despite the successful detection of a specific RNA target from a background of total RNA extract, BSI displayed moderate specificity using a series of mismatched RNA targets (Figure 4.4A). As the focus of this initial work has been centered on improving the sensitivity of BSI, there are many factors for optimization of specificity to be examined in future work.

It was determined that individual probes of similar nucleotide content and length did not produce a similar level of BSI signal. We found that the discrepancy in BSI signal produced from the various probe sequences can be partially explained with RNA folding predictions of the RNA target. For most RNA sequences, secondary structures are significantly more stable than tertiary structures and are more likely to contribute to the native structure of the RNA target[178]. Therefore, only the secondary structure of the RNA target was evaluated in these studies. Using mfold software to predict the folding state of the RNA target, we found that probes targeting sequences predicted to have mostly unpaired nucleotides (i.e. open loops) generally produced more signal than

probes targeting sequences predicted to be mostly double stranded. Two probes, however, produced exceptionally high signal compared to probes targeting regions of similar predicted secondary structure. Alterations in the tertiary structure of the RNA target induced by probe binding may explain the comparatively large signal changes produced by these probes. Future studies will be aimed at investigating the role of tertiary structure in BSI signal generation.

It was also found that the integration of 'locked' nucleotides into the DNA probe nearly quadruples the sensitivity of BSI (Figure 4.6 and Table 4.1). LNA has been widely used for nucleic acid probing applications[179-181]. It has been reported that LNA has exceptional binding affinity for complementary RNA or DNA targets while maintaining or even improving sequence specificity[174]. Because BSI detects changes in the RI that are induced by the binding of two molecules, the signal enhancement produced by LNA oligonucleotides could potentially have thermodynamic, structural and/or solvation explanations. Perhaps the most important characteristic of LNA oligonucleotides is the high thermal stability when duplexed with RNA. Melt temperatures of LNA:RNA hybrids can increase by  $\sim 5^{\circ}\text{C}$  per locked nucleotide incorporated into the sequence[179]. Because of this high affinity for RNA, a higher proportion of LNA oligonucleotides should bind complementary targets compared to DNA of identical sequence and length. However, the amount of DNA and LNA probe used in these studies is in great excess relative to the number of available targets, which is intended to drive binding toward probe saturation. The



hybridization studies confirmed that the relative amount of bound LNA probes is nearly the same as DNA probes at equilibrium (Figure 4.6B), indicating that the thermodynamic explanation is probably not the greatest contributor to the BSI signal enhancement.

The RI of a solution can also change when solutes undergo changes in structural conformation. When binding RNA, a single LNA nucleotide can perturb the surrounding DNA nucleotides to adopt the C30-endo conformation. Consequently, LNA:RNA hybrids form homogeneous A-form helical secondary structures, whereas DNA:RNA hybrids generally form a heterogeneous mix of both A-form and B-form. Our secondary structural analysis of the nucleic acid hybrids using CD confirmed that the LNA:RNA hybrids formed A-form helical structure, whereas the DNA:RNA hybrid forms a mixture of A-form and B-form helical structures (Figure 4.7A). As another point of reference, we studied a DNA:DNA duplex with distinct B-form character as confirmed by CD. The increased sensitivity of BSI for detecting A-form hybrids, compared to the A-form and B-form mixed hybrid or the B-form duplex, indicates a structural basis for RI perturbation (Figure 4.7B). This was further validated through the measurements conducted on the TFE-induced A-form character of the DNA:DNA duplex, which resulted in increased BSI signal (Figure 4.8).

In addition to structural changes, the exchange of the water molecules that hydrate the soluble molecules upon binding is thought to influence the RI, which would have direct implications for BSI signal generation. It has been predicted based on NMR structure measurements of LNA:RNA hybrids that the number of

water molecules interacting with the minor groove may be increased compared to DNA:RNA hybrids[182]. The structure of an A-form hybrid may produce a larger BSI signal than B-form due to this exchange of waters of hydration from the solvent to the molecules, accounting in part for the improved BSI sensitivity when using the LNA probe. Continued efforts are aimed at identifying the role of waters of hydration on the shift of RI that occurs when an oligonucleotide probe hybridizes to an RNA target.

#### **4.5 Summary and future directions**

The results of these studies outline a set of optimal characteristics of nucleic acid probes for BSI detection of a viral RNA biomarker. It was determined that multiple nucleic acid probes, 22 nt in length, designed to target regions distributed across the RNA target resulted in the greatest BSI signal. These studies also indicate that the folding of the RNA target as well as the formation of the secondary structure geometry contributes substantially to BSI sensitivity for RNA detection. There is evidence that mfold software can be used to identify regions of unpaired nucleotides in RNA targets that are likely to produce high signal upon binding. Additional studies aimed at determining tertiary structure contributors to signal enhancement along with the secondary structure predictions of mfold could be useful for the rational design of oligonucleotide probes for BSI detection. Additionally, it was determined that the induction of altered helical geometry of nucleic acids upon probe binding significantly improves BSI signal. We found that this can be achieved using LNA probes or a high background concentration of TFE, which promote formation of A-form

structure in nucleic acids. Future work will focus on strategies to further enhance BSI sensitivity and specificity for RNA biomarkers, which could pave the way for a clinically relevant BSI assay for the detection of viral RNA in patient samples.

Building on this work, the next steps are to further improve RSV n-gene RNA assay sensitivity to enable us to use BSI in diagnostic assays at clinically relevant detection limits. The work in chapter 2 demonstrates that the BSI signal and the binding affinity are improved, at least for the lectin-sugar system, when performed in a surface-bound assay format as opposed to free-solution. I postulate that by capturing the RNA target with an immobilized probe, the assay sensitivity will be improved by at least 2-fold. Additionally, by interrogating the target with as many rationally designed secondary probes as possible, and by inducing large conformational changes, detection limits will be further improved. Finally, performing the assay in an integrated sample-reference configuration (Chapter 7) is predicted to improve detection limits by an order of magnitude. This design will automatically compensate for laser beam alignment instability, mechanical vibrations, and temperature induced refractive index changes that are less controllable with the current BSI instrument. By combining the aforementioned assay optimization techniques with a sample-reference instrument design, it is predicted that the cumulative improvements in RNA detection limits will enable the detection of RSV n-gene RNA at concentrations that are low enough that treatment would be clinically effective.

This work was published in *Nucleic Acids Research* in 2013[3].

## CHAPTER 5

### IMPROVING THE CURRENT LIMITS OF DETECTION OF NON-SMALL CELL LUNG CANCER BIOMARKERS VIA BACKSCATTERING INTERFEROMETRY

#### 5.1 Introduction

Lung cancer is the number one cancer killer among men and women in the world. In the US, lung cancer kills more men and women than colorectal, prostate, and breast cancer combined[183]. Although advances have been made in diagnosis and treatment strategies in the last decade, the prognosis of patients with lung cancer remains poor, with a 5-year overall survival of 16%[12, 184]. *This is mainly due to a lack of sensitive and specific early detection methods.* As a result, more than 70% of patients are not diagnosed until the disease has progressed to an advanced stage where it is no longer curable[183]. In response to this critical need, the search for diagnostic strategies for early lung cancer detection has been intensified in recent years.

Currently, the most common method of lung cancer diagnosis is through a computed tomography (CT) scan. Screening by CT is not without its problems, however. In these tests, lung nodules of indeterminate significance are discovered in over 25% of the individuals screened. The vast majority of these nodules (96%) are benign, but are very difficult, if not impossible, to distinguish from malignant growths. Invasive and expensive follow-up diagnostic tests, including transthoracic needle aspiration, bronchoscopy or thoracotomy, are

often required to determine the nature of nodules identified by chest CT, delaying initiation of treatment.

Current detection techniques and assay content do not perform adequately to provide clinically relevant diagnostic information. Many methods have been developed to detect biomarkers, or molecules relevant to disease, including ELISA, Illumina's "BeadArray" methods, label-free techniques including surface plasmon resonance (SPR), quartz-crystal microbalance, wave-guided interferometry[80, 87, 185] and of course mass spectrometry (MS)[186, 187]. For clinical diagnostics, these methods suffer from one or more deficiencies in terms of speed, sensitivity, convenience, cost and/or accessibility[186].

Validation of promising biomarkers is currently a slow process, because of assay development bottlenecks and sample consumption limitations. There is a definite need for an easy-to-use, quantitative technology that is sensitive, specific, rapid and requires minimal sample. Such a method would likely be useful for the detection of response to therapy. BSI satisfies the requirements of being compatible with complex matrices[70, 74] while being a simple, isothermal, highly sensitive, label- and enzyme-free technology. It uses a unique form of signal transduction that circumvents the limitations of other methods. Capitalizing on a unique resonant cavity interferometric approach, BSI provides femtomolar sensitivity without labels and it uses nanoliter sample volumes. BSI's highly modular nature allows a wide array of interactions (antibodies to DNA to small molecules) to be quantified. Our BSI methods have shown to give a minimum sensitivity improvement over existing '*immuno*'assays of 10-50 fold,

while constraining the sample quantity to 1  $\mu$ L or less.

## **5.2 Materials and methods**

### **5.2.1 Biomarker Calibration Curve Construction**

A calibration curve was constructed for each biomarker in order to determine the BSI lower limit of detection. All reagents used were obtained from a commercial ELISA kit (DRG International and DuoSet for cyfra 21-1 and galectin-7 assays respectively). Increasing concentrations of recombinant protein (0-10 ng/mL) spiked in 20% human serum were incubated with a constant concentration of antibody for 1 hour at room temperature to allow for complete binding to take place. A series of blanks were similarly prepared, except buffer was used in lieu of antibody. Once equilibrium was reached, 1  $\mu$ L of sample was injected into the BSI channel and measured for 30 seconds. The corresponding blank was immediately measured after the sample and subtracted from the sample signal. All samples and blanks were measured in triplicate each day on five separate days. Cyfra 21-1 data was fit to a linear calibration curve and plotted as a function of LOG[cyfra 21-1]. For comparison, a cyfra 21-1 calibration curve was constructed in 20% plasma.

Galectin 7 data was fit to a 3<sup>rd</sup> order polynomial and plotted as a function of concentration. Curve fit functions were chosen based on the best R-squared value. A 3<sup>rd</sup> order polynomial function was chosen based on the non-linear response. Calibration curves for both biomarkers were also constructed as a benchmark with spiked 20% human serum using a commercial ELISA kit. The

ELISA calibration curve was created using triplicate determinations, following the manufacturer's recommended procedure. Lower limits of detection were calculated by determining the lowest concentration at which the signal to noise ratio is 5 or higher. An alternative calculation was performed using the following equation:

$$\text{LLOD} = 3\sigma / \text{initial slope}$$

where  $\sigma$  = the standard deviation of all 15 trials run over 5 separate days. The results of both methods were in close agreement.

### **5.2.2 BSI Patient Serum Sample Analysis**

Serum samples were collected from individuals with and without lung cancer from our Lung SPORE repository. Serum samples were prepared following a standard operating procedure, aliquoted and stored at  $-80^{\circ}\text{C}$  until analysis as described previously [188]. For galectin 7 analysis, ten samples were from patients with no sign of lung cancer (controls, N=4), or NSCLC histology (stages IA-III A) of either squamous cell carcinoma (SCC, N=3) or adenocarcinoma subtypes (ADC, N=3), (Table 1). Control individuals were proven without evidence of lung cancer at one year follow up. All serum samples were obtained from individuals matched for age, gender and smoking history. For Cyfra 21-1, a total of 15 samples were used for analysis from control (N=7) and SCC patients (N=8), (Table 1). Patient serum samples were diluted 1:5 with

PBS buffer and mixed with antibody. The samples were left to incubate at room temperature for 1 hour before being measured by BSI. A blank was also prepared by mixing diluted patient samples with buffer in the absence of antibody. The difference in shift between the sample and the blank was recorded and fit to the appropriate calibration curve to calculate the biomarker concentration. Patient serum samples were also analyzed using a commercial ELISA kit which was performed according to the manufacturer's specified procedure.

## **5.3 Results and discussion**

### **5.3.1 Improving current limits of detection**

Early detection of lung cancer is the best tool for efficacious treatment. Cyfra 21-1 is a NSCLC blood-based biomarker with a concentration that correlates to disease progression[16, 32, 189, 190] However, Cyfra 21-1 concentrations in healthy individuals are 2.4 ng/mL [189], which are below the ELISA detection limit, currently 10 ng/mL [13]. The BSI lower limit of quantification for Cyfra 21-1 was determined to be 230 pg/mL in serum and 585 pg/mL in plasma using the signal to noise method described in the experimental section. Interestingly, at this quantification limit there are approximately 14,000 molecules of the lung cancer biomarker in the 4 nL of human serum probed by the laser. Figure 5.1A illustrates a clear advantage over the standard ELISA assay, also showing the day-to-day reproducibility. Without immobilization and



labeling chemistry, the BSI assay was shown to be *24-fold more sensitive than ELISA*.

Galectin-7 has been recently discovered by shotgun proteomic analysis of stage I NSCLC fresh frozen tissues [188] and was chosen because currently available ELISA kits are unable to quantify Galectin-7 low level expressing patients, yet should serve as an early disease marker. Using the detection antibody alone, the BSI lower limit of quantification for Galectin-7 was 39 pg/mL. Since the BSI signal is both proportional to the number of binding events and agnostic toward interaction species, the use of multiple probes (or even different types of probes) is predicted to improve the quantification limits and specificity. We compared the performance of BSI for Galectin-7 detection using just the capture Ab and then both the capture and detection Ab from a DuoSet® human Galectin-7 ELISA kit. Then we compared these results to ELISA. Using both antibodies, the limit of quantification was decreased nearly 4-fold to 13 pg/mL. In our hands the ELISA limit of quantification was 500 pg/mL. The blue line in Figure 5.1B shows the BSI response using only the capture Ab from the kit and should be compared to the green line which displays the ELISA output. The addition of the second antibody, red line in Figure 5.1B, provides an additional species which is also able to bind the analyte, and since the BSI signal is proportional to the number of binding events, a significant improvement in sensitivity in 20% serum is realized. Furthermore, the entire BSI serum assay consisting of a 10 point calibration curve measured in triplicate was performed using just 36  $\mu$ L as opposed to 200  $\mu$ L required by a commercial ELISA kit.

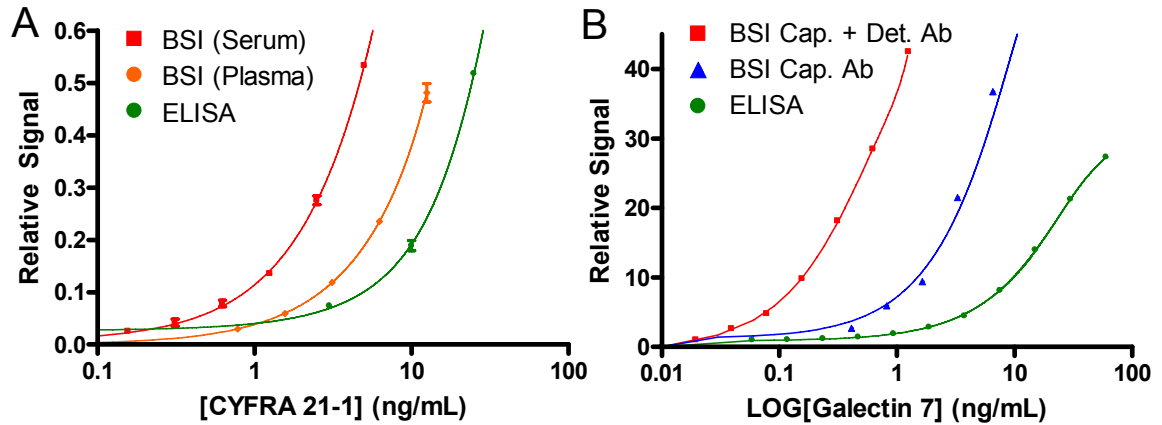


**Figure 5.1:** BSI out-performs ELISA for the detection cyfra 21-1 (A) and galectin-7 (B). For galectin-7, the response is improved by using both Ab pools. (Error bars shown for repeat triplicate determinations over a 5 day period)

### 5.3.2 Patient serum sample analysis

Having demonstrated that that BSI could readily detect biomarkers at levels below current ELISA detection limits, we chose to perform assays on clinical samples. In this case, previously characterized, patient serum samples spanning a range in disease progression were provided in a blinded fashion. Patient serum samples were diluted to 20% and analyzed. The concentration of each patient sample was calculated using the response curve from Figs 5.1A and 5.1B for Cyfra 21-1 and Galectin-7 respectively. Each patient serum sample was measured in triplicate on 5 separate days, for a total of 15 determinations. The intraclass correlation coefficient (ICC), a reliability index, was calculated to evaluate the reproducibility of the measurements on both Cyfra and Galectin. The results (0.93 for Cyfra and 0.96 for Galectin) showed that the variation of the measurements on the same sample is significantly lower than the variation of the

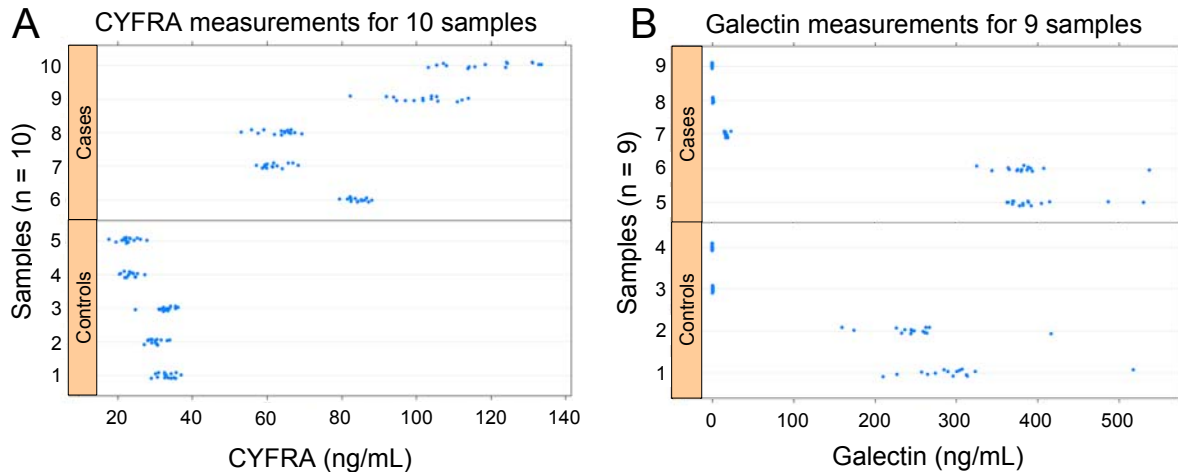


Figure 5.2: Raw patient sample data for cyfra 21.1 (A) and galectin-7 (B) measured each day in triplicate for 5 days. The 15 measurements of the same sample are closer to each other relative to the measurements of different samples

measurement of two different samples, which indicated that the measurement is reliable (Figure 5.2).

Cyfra 21-1 is a well characterized biomarker [13, 14, 188] and serves as a good target to evaluate the performance of BSI vs. ELISA to quantify a protein biomarker for lung cancer in patient samples. As shown in Figure 5.3A, the concentration of the Cyfra 21-1 biomarker determined by BSI in this blinded study corresponded well with those provided by the ELISA measurement. Over all the Cyfra 21-1 values obtained by BSI were within 8.5% difference of the ELISA values. The lines on the plot show the threshold for quantifying the biomarker with confidence and clearly indicate that BSI has the potential to enable the analysis of much lower Cyfra-21-1 values in patient samples. This advantage could allow disease to be detected at much earlier stages or

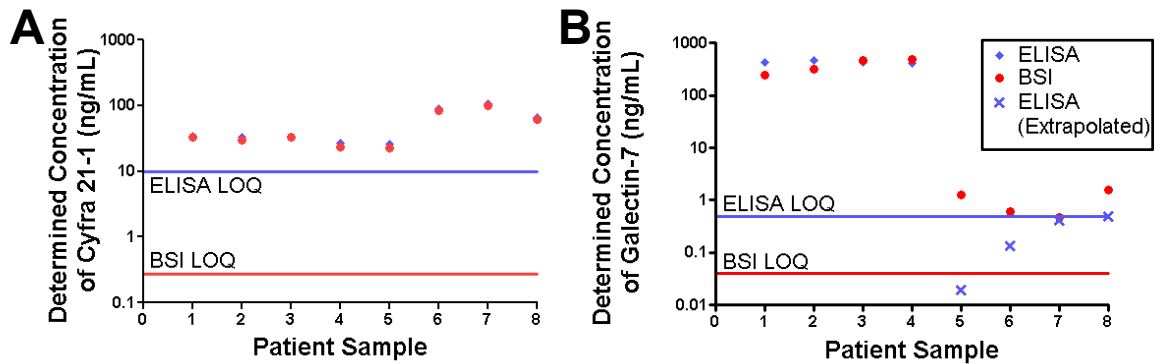


Figure 5.3: Cyfra 21-1 concentrations in patient serum samples measured by BSI compare favorably to plasma concentrations measured by ELISA (A). BSI measures all galectin-7 patient serum samples, half of which are below the ELISA limit of detection (B). Samples were a from patients with no sign of lung cancer (control) or NSCLC histology, stages IA-IIIa (case). Concentration values below the limit of quantification were extrapolated from the calibration curve and bear no statistical relevance.

therapeutic response to be monitored with greater confidence, significantly improving clinical outcomes[188].

Galactin-7 was also quantified by BSI in a small group of blinded patient samples and compared well with ELISA results. As shown in Figure 5.3B, we were able to determine the Galactin-7 concentration in several patients where the ELISA results are below the minimal detectable quantity. Measurements made by ELISA where biomarker concentrations were below the limits of quantification were calculated using extrapolation and are should not be considered reliable. However, it is in this region that we are confident that the high sensitivity of BSI will provide the opportunity to enhance the value of using biomarker assays to guide patient management. The analogy with the CRP (C-reactive protein) assay developments is helpful to illustrate the potential of our approach. The CRP assay was developed and has typically been used grossly as a marker of

Table 5.1: Comparison of BSI and ELISA performance

	Limit of Quantification (ng/mL)		% CV at LOQ	
	BSI	ELISA	BSI	ELISA
<b>Cyfra 21-1</b>	<b>0.230</b>	<b>4.0</b>	<b>14.7%</b>	<b>9.0%</b>
<b>Galectin-7</b>	<b>0.013</b>	<b>0.50</b>	<b>14.8%</b>	<b>7.1%</b>

**LOQ calculated by  $3\sigma/\text{slope}$  ( $\sigma$  = average standard deviation over 15 trials)**  
**% CV calculated by standard deviation over 15 trials / signal for each concentration**

inflammation. Recognizing that atherosclerosis is an inflammatory disease, researchers wanted to quantify the inflammatory response in patients with various cardiovascular (CV) risk. Dramatic improvements in the sensitivity of the assay (20-fold increase) led to the high sensitivity CRP assay (hsCRP) allowing the testing of this rather abundant protein during inflammation, at very low concentrations in individuals with various degree of CV disease[191, 192]. Association studies between CRP values as determined by hsCRP and CV risk have now been proven and this assay is now broadly used in the clinic for CV risk assessment [193, 194]. Being able to capitalize on the high sensitivity of BSI for Cyfra 21-1 will have to be tested in a representative lung cancer patient cohort, yet preliminary results show promise for improving the management of this disease.

#### 5.4 Summary and future directions

It was shown that BSI can be used to quantify NSCLC biomarkers in complex matrix at concentrations that are up to 40-fold lower than commercially

available ELISA assays (Table 5.1). Because of the assay is free-solution and label-free optimization takes days instead of weeks or months, saving valuable resources and significantly expediting the biomarker validation process. BSI also enabled the characterization of patient serum samples with results that are in excellent agreement with ELISA which is the current gold standard in disease diagnosis.

I believe these results indicate that the application of BSI to a larger number and types of lung cancer candidate biomarkers, as well as other types of diseases could improve diagnosis, risk assessment, and response to therapy in the clinical setting. Future efforts should be focused on optimizing BSI as a user friendly instrument and further improving sensitivity and specificity. This could be accomplished by using different antibody motifs, other probes, such as aptamers, and refining assay configurations to reduce non-specific binding to the BSI chip.

Additionally, having shown that BSI possesses the analytical sensitivity necessary to analyze biomarkers at detection limits below the current gold standard, future efforts should be focused on the analytical validation of other biomarkers where patient biomarker expression is below ELISA detection limits. Analytical validation determines the suitability of a particular technology to characterize biomarkers, whereas clinical validation determines the medical relevancy of a particular biomarker. Once BSI has been further proven as an analytical validation tool, work towards demonstrating its utility in clinical validation can begin.

## CHAPTER 6

### **BACLOFEN AND OTHER GABA<sub>B</sub> RECEPTOR AGENTS ARE ALLOSTERIC MODULATORS OF THE CXCL12 CHEMOKINE RECEPTOR CXCR4**

#### **6.1 Introduction**

CXCR4 is a G protein-coupled receptor (GPCR) that selectively binds CXCL12 (stromal-cell derived factor: SDF-1 $\alpha$ ). This chemokine and its receptor have been found to play important roles in several processes involved in ischemic stroke and its subsequent repair [195], brain tumor pathogenesis [196], HIV encephalopathy [197], Multiple Sclerosis and stem cell migration [198]. CXCR4 is widely expressed in a variety of cell types including leucocytes, where it promotes migration, recruitment and activation [199-203], neurons, where it modulates electrical activity [204-206], and various cancers and metastases [207] where it is involved in tumor progression [208-210]. CXCR4 also binds the human immunodeficiency virus (HIV-1) viral envelope glycoprotein gp120 [211, 212]. Thus, CXCR4 is an important therapeutic target for stroke, inflammation, neuromodulation, cancer, and in the prevention of HIV infection. CXCR4 couples to the G family of proteins activating multiple G-protein dependent and independent pathways [213, 214]. In neurons, CXCR4 stimulation has been shown to activate a G-protein Inward Rectifier K<sup>+</sup> (GIRK), a voltage-gated K channel Kv2.1 associated to neuronal survival, and to increase high voltage activated (HVA) Ca<sup>2+</sup> currents [205, 215].

The  $\gamma$ -aminobutyric acid type B (GABAB) receptor is also a GPCR activated by  $\gamma$ -aminobutyric acid (GABA), the chief neuro-inhibitory neurotransmitter in mammalian systems. GABAB receptors are obligatory heterodimers with 2 homologous subunits (GB1 and GB2) required for functioning, are widely expressed and distributed in the central nervous system [216] and can activate diverse intracellular pathways [217, 218]. GABAB receptors are also expressed on cells of the immune system with a possible link to the inflammatory response [219, 220]. As a consequence, there is a rich pharmacology aimed at targeting GABAB receptors, with numerous compounds currently being used with the presumption that they are highly selective for these receptors [221]. Given that CXCR4 and GABAB have co-expression on immune cells and neurons, and the evidence for possible cross-talk between these receptors, we hypothesized that ligands binding GABAB are involved in allosteric or direct interaction with CXCR4. Here we describe the experiments that test our hypothesis. While somewhat unexpected, we observed that GABAB agents such as baclofen, the antagonists CGP55845 and 54626 and GABA can directly bind the chemokine receptor CXCR4.

## **6.2 Materials and Methods**

Binding assays with BSI were performed as described previously [70]. Briefly, lipoparticles containing CXCR4 (Integral Molecular), stored at 4°C, were used and binding was measured by BSI in the typical endpoint format [70]. Ligand binding to the lipoparticle was accomplished by incubating a fixed amount



of lipoparticle solution with varying concentrations of ligands (CXCL12, GABA, GABAB modulators, baclofen and dopamine) for 1 hour at room temperature. Solutions containing the same concentration of ligand and a null lipoparticle (lipoparticles without a receptor expressed) were used as reference samples to account for any non-specific binding to the particle. Dopamine was used as a non-binding negative control ligand and did not show any binding signal. For each sample, a solution of ligand and the null lipoparticle was introduced into the channel and the BSI signal was measured. The channel was rinsed and the solution containing the ligand and the CXCR4 lipoparticle was introduced into the channel and the signal measured. This procedure was repeated iteratively for increasing ligand concentrations. Data was collected with program written in-house using LabView (National Instruments). The binding signal was calculated as the difference in phase between the null lipoparticle-ligand solution and the CXCR4 lipoparticle-ligand complex. The background signal due to the presence of the receptor was subtracted from all measurements. This corrected binding signal was plotted versus concentration to form a saturation binding isotherm and the affinity was calculated by fitting to a square hyperbolic function using GraphPad Prism software.

### **6.3 Results and Discussion**

CXCR4 and GABAB often co-express in the same cell type [204], have complementary functionality and may be involved in cross-talk [222]. We describe two new examples of such interaction, one involving chemotaxis the

other involving ionic current modulations, in which agents historically believed to act selectively on GABAB receptors also affect the CXCR4 system. Furthermore, we provide evidence that these ligands specifically bind to CXCR4 and quantify the binding affinity for these interactions.

Binding specificity of the native pairs CXCR4/CXCL12 binding using red blood cell “ghosts” with human SUP-T1 lymphoma T cells expressing CXCR4 and BSI has been previously reported [70]. Here, we expressed the CXCR4 receptor using lipoparticle technology: protein directly incorporated into virus-like particles with a lipid bi-layer surface that provides concentrated protein (50-200 pM/mg) in the native conformation [223]. Equilibrium dissociation constants were calculated using saturation analysis. The reference was lipoparticles devoid of the receptor and to further demonstrate that the refractive index (RI) change is specific (not due simply to the introduction of the binding pairs), we used dopamine as a control. In no experiment did we measure an RI change for the control.

In figure 6.1A the saturation isotherm is presented for the measurement of the binding of native ligand CXCL12, also called SDF for CXCR-4, which gave a KD of 0.49 nM ( $\pm$  0.16 nM). This value is in excellent agreement with previously published report [223]. Next, for the first time, we have measured binding of the two GABAB antagonists CGP55845 and CGP54626 (Figure 6.1B, C) calculating KD values of 11nM ( $\pm$ 0.5 nM) and 35 nM ( $\pm$ 6.2 nM) respectively. Finally, and again for the first time, we measured binding of two GABAB agonists to CXCR4,

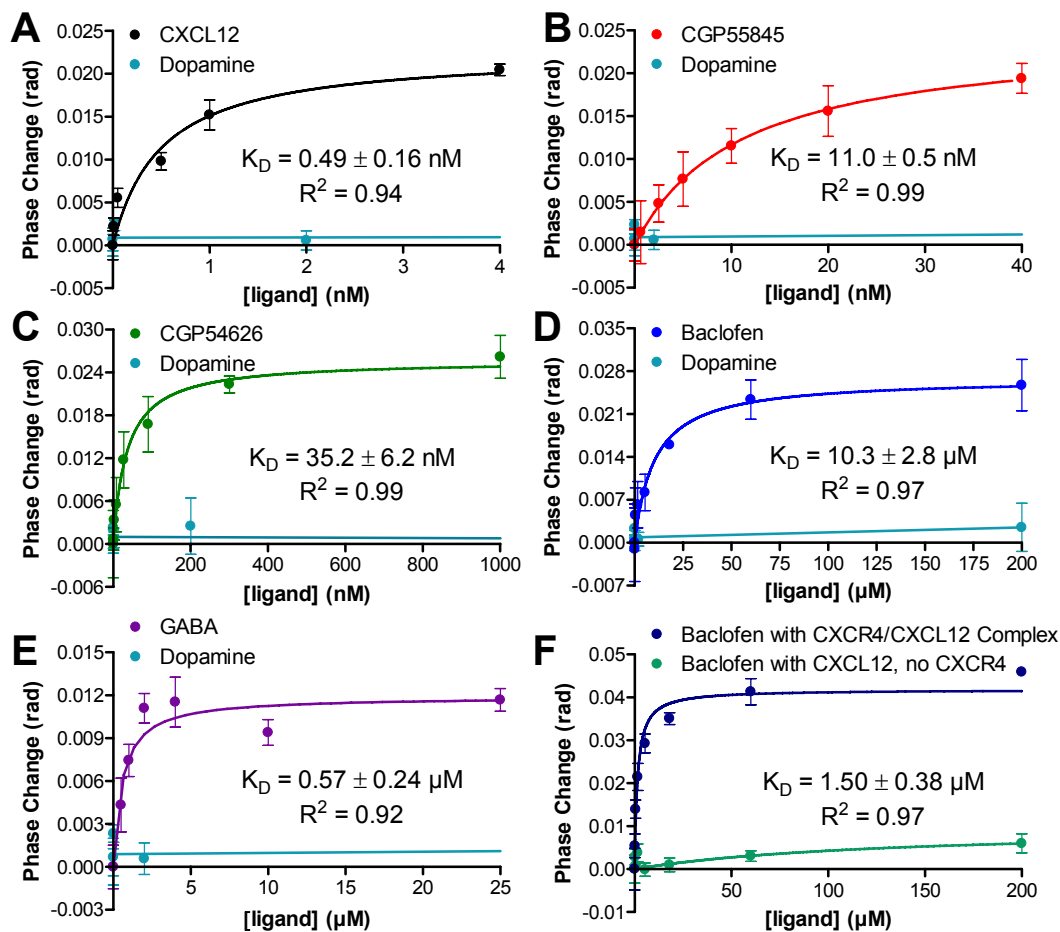


Figure 6.1 Representative plots of BSI signal versus ligand concentration for the determination of binding constants for CXCR4 to the following ligands: CXCL12 (A), CGP 55845 (B), CGP 54626 (C), Baclofen (D), and GABA (E). Dopamine was used as a non-binding control ligand for all five plots. The binding of baclofen to the CXCR4-CXCL12 complex (0.2 nM CXCR4 +20 nM CXCL12) is represented in (F)[1]

baclofen and GABA (Figure 6.1D, E) calculating KD values of  $10.3 \pm 2.8 \mu\text{M}$  and  $0.57 \pm 0.24 \mu\text{M}$ .

To confirm that this binding is at a different site from that of the native ligand CXCL12, we pre-incubated the lipoparticles with CXCL12 (SDF) and performed a binding assay using baclofen ligand. Figure 6.1F shows that baclofen is still binding CXCR4 even when CXCL12 is bound and the affinity and

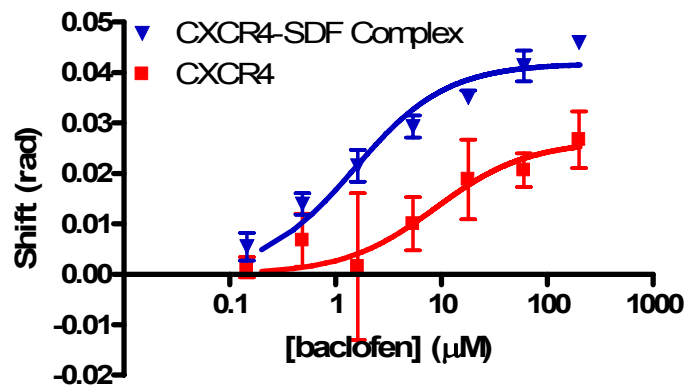


Figure 6.2: The binding of baclofen to CXCR4 is enhanced when SDF is already bound to the allosteric site

signal magnitude for baclofen with the receptor is enhanced by CXCL12 binding (Figure 6.2). To demonstrate that the observed binding was not due to CXCL12 interacting with baclofen, CXCL12 and baclofen were incubated in the absence of CXCR4, with no observed binding signal (shown in Figure 6.1F). These results are proof in principle that GABAB ligands directly bind CXCR4, and at a site distinct from the active site. Our study demonstrates that GABAB agonists and antagonists directly bind CXCR4 by allosteric action. This finding has important physiological implications for the immune and nervous systems and is also highly relevant in pointing a novel molecular target to baclofen, a drug widely used in human health.

BSI assays showed a direct interaction of GABAB receptor antagonists and agonists with CXCR4, with KD values that are in the range of previously established electrophysiological results. The Tag-lite competition ligand-binding assay (data not shown) demonstrated that GABAB receptor antagonists/agonists do not interact at the ligand binding domain for CXCL12 on CXCR4. This result is

corroborated by the difference in Hill numbers observed in the concentration-response curves between CXCL12 on one side (close to 2) and the GABAB agents on the other side (Hill number close to 1). This difference indicates a separate mode of action. It is hard to speculate on the site and mechanisms of interaction of GABAB agents on CXCR4 and these questions will be the topic of future studies. Using Tag-lite technology Forster's radius ( $R_0$ , distance equivalent to 50% transfer efficiency) of 9 nm of the CXCR4-Terbium cryptate-GABABd2 labeled ligand pair, indicates that the allosteric site is likely far from the CXCL12 binding pocket. Another way to test this would be using the crystal structure of the receptor in the presence of the GABAB receptor antagonists/agonists to determine where these compounds interact on the chemokine receptor. Silencing CXCR4 expression through siRNA technology would also provide some clue on the relevance of GABA-CXCR4 interactions in mammalian cells and whether a heterologous dimerization may be occurring. Other mechanisms of interactions between GABAB and CXCR4 are currently under investigation, and will address the question as to whether the mechanism involves direct interaction or activation of a second messenger cascade.

#### **6.4 Summary**

The ability to monitor interactions with lipoparticles containing ion channels and GPCR receptors was once speculation. However, this study demonstrates the utility of BSI to measure such interactions with high sensitivity. Because BSI does not require labels or surface immobilization, all measurements

reflect the native state of the systems studied. GABA ligand, once thought to bind exclusively to the GABA receptor, was shown to bind with CXCR4 as well. Furthermore, an allosteric interaction between various ligands (SDF and baclofen) binding CXCR4 was identified for the first time.

#### **6.4.1 Physiological implication**

This study shows that GABA is able to block the effect of CXCL12 on CXCR4. Thus, it is likely that when the GABAergic system is activated, GABA released in the brain will antagonize the effect of CXCL12 on its receptor CXCR4, and thus could influence the chemokine neurotransmission as well as the inflammatory response in the central nervous system. We now demonstrate that there is reciprocal cross talk between these two systems as it has previously been shown that CXCR4 stimulation by CXCL12 can increase presynaptic GABA release [205]. Indeed, in dopaminergic neurons of the rat substantia nigra, it has been previously shown that CXCR4 stimulation by CXCL12 induces an increase of release of presynaptic neurotransmitter, particularly of GABA [224]. It has also shown that CGP55845 (500 nM) blocks the outward G protein-coupled inwardly-rectifying potassium channel (GIRK) current induced by CXCL12 (recorded in the presence of glutamate receptor blockers). At that time, we interpreted this result as an effect mediated through GABAB receptor stimulation by GABA spilling over following CXCL12 presynaptic stimulation and increase in GABAB release. However, in view of the present results, we can reinterpret our data. Indeed, the

GIRK currents might have been activated by the stimulation of postsynaptic CXCR4 by CXCL12, which was then blocked by CGP 55484.

CXCR4 activation by CXCL12 has been shown to increase presynaptic neurotransmitter release and particularly GABA release in several neuronal populations [205, 225, 226]. If GABA can in turn block the effects of CXCL12, this could represent a negative feedback loop for presynaptic chemokine release. Indeed, when applying CXCL12 for several minutes, a transient increase in the frequency of spontaneous postsynaptic currents sPSCs is frequently observed, followed by a reduced activity (see Figure 3 in [224]). This reduction could be due to an antagonistic effect of GABA, although desensitization of CXCR4 itself cannot be excluded. Similarly, it has been shown that elevated concentrations of CXCL12 exert opposite effect than lower concentrations on the electrical activity of some neuronal populations that receive GABA inputs [205]. The antagonistic effect of GABA released pre-synaptically in response to CXCL12 could contribute to these biphasic effects. In the future, it will be of interest to search for putative effects of GABAB receptor ligands on CXCR7, the other receptor for CXCL12 [227], as well as on other chemokine receptors.

#### **6.4.2 Putative applications in cancer treatment and inflammation**

Baclofen treatment was demonstrated to reduce the incidence of some carcinogen induced gastrointestinal cancers in rats [228] as well as human hepatocarcinoma cell growth [229]. By contrast, baclofen promotes human prostate cancer cell migration [230]. As CXCR4 is highly expressed in cancer

cells, baclofen may have been acting through CXCR4 in these examples. Similarly, it has been shown that GABA can affect cell proliferation and have anti-inflammatory properties on fibroblasts, although the mechanism of action of GABA was not elucidated [231]. We suggest that GABA may have acted through the CXCR4 receptor, as CXCR4 is expressed on fibroblasts [226]. Baclofen is currently used for the treatment of *spasticity* in patients with spinal cord injury, cerebral palsy, traumatic brain injury, multiple sclerosis and other disorders [232-234]. Recently, it has been used in the treatment of alcohol dependence and withdrawal [235]. The allosteric effects of such agents at CXCR4 likely contribute to these beneficial effects as CXCR4 often co-localizes with GABAB receptors. As a conclusion, this study opens new perspectives on the putative use of baclofen and other GABAB agents acting at CXCR4 for their therapeutic potential to treat quite a broad range of diseases, such as ischemic stroke, brain tumors, HIV encephalopathy, Multiple Sclerosis, as well as affecting stem cell migration [222] and other cancers.

#### **6.4.3 Key observations and Future directions**

The discovery that CXCR4 interacts with ligands that were once thought to interact exclusively with GABA<sub>B</sub> further brings into question the paradigm that “ligands are exclusive for a particular receptor and cross reactivity is relatively uncommon”. What this research also shows is that BSI can be effectively used to study other non-native ligand-receptor interactions, particularly those that could possibly bind CXCR4.



Going forward I recommend expanding on these investigations, initially with GP120 which is a glycoprotein expressed on the surface of the HIV envelope. Preliminary studies conducted in the laboratory of Alice Guyon have indicated that Gp120 may interact with the GPCR CXCR4. Characterizing the binding interaction that takes place between Gp120 and CXCR4 could have important implications for understanding the HIV infection process.

The first step I recommend would be to obtain an understanding how non-traditional ligands, such as the GABA ligand and commercial pharmaceutical, baclofen, influence the Gp120 binding site on CXCR4. These studies could provide insight into the mechanism of action for Gp120 and CXCR4 and subsequently lead to methods to enhance HIV treatment.

In light of the findings of this chapter, which highlight the fact that many ligands once thought to bind a single receptor exclusively are in fact more promiscuous, a study should also be undertaken to determine whether or not CD4, a recombinant protein reactive with HIV-1 gp120, binds with any specificity to CXCR4. Overall these studies could provide valuable insight into the mechanism of HIV-1 infection.

This work was published in The Journal of Neuroscience in 2013[1].

## CHAPTER 7

### A SINGLE CHANNEL SAMPLE-REFERENCE BACKSCATTERING INTERFEROMETER FOR IMPROVED PERFORMANCE

#### 7.1 Introduction

The ability for BSI to make fast, precise, inexpensive measurements in a label-free manner makes it an ideal candidate as a clinical diagnostic instrument. Furthermore it has shown promise in drug discovery, biomarker validation, and environmental sensing. However, there are still considerable challenges that prevent widespread use in such a setting. Currently, the BSI optical train is built on an open bread-board, relying on specialized equipment to maintain a precise room temperature at all times. Furthermore, the need to measure samples and blanks separately and sequentially decreases the signal to noise ratio of an assay due to variations in manual injection reproducibility, and fluctuations in temperature and/or pressure over short time periods. It also doubles the amount of time for an assay to be performed. While efficacious, BSI currently has limited throughput because of the manual injection method employed. The development a multiplexed version of BSI that is capable of measuring sample and blanks simultaneously would not only allow for compensation for environmental noise such as temperature fluctuations in real-time, but also improve throughput by increasing the number of unique measurements made at once.

## 7.2 Previous BSI multiplex strategies

The precursor to a multiplexed BSI instrument can be found in the dual-capillary and two-channel configurations which allowed for simultaneous sample and reference measurements, but in different 'interferometers'. In the capillary design[236], two capillaries were positioned in a holder so that they are touching each other, but tilted at an angle relative to laser beam. Both tubes are illuminated with the same laser and the resulting interference patterns are interrogated above and below the plane of the incoming source. In the chip-based design the channels are separated by ca. 1 mm and a calcite beam splitter is employed to split the laser beam into two equal intensity, parallel beams. These two beams are aligned (off-set) in a manner that allows the two channels to be interrogated simultaneously without the interference patterns overlapping each other. Each design allows for S/N improvements of ten-fold or greater with a limit of detection on the order of  $1 \times 10^{-9}$  RIU [237] possible from the capillary system. Yet, both designs have limitations principally related to alignment challenges and difficulty in balancing the two different interferometers so that they provide compensation.

## 7.3 Single Channel Sample Reference BSI

To circumvent the limitations of the dual-capillary and two-channel designs, I configured the BSI instrument so that *both* the sample and reference regions can be adjacent to each other and so that the capillary or microfluidic chip can be

interrogated with the same laser beam. The **Single Channel Sample-Reference BackScattering Interferometer (SCSR-BSI)**, is illustrated in Figure 7.1.

SCSR was configured with a Melles Griot HeNe laser with the beam is expanded along the capillary/channel, with a cylindrical lens (F.L. = 25 cm) to 0.8 x 4.0mm (Figure 7.1). The expanded beam illuminates a 4mm section of polyimide-coated fused silica capillary tubing (O.D. = 360  $\mu\text{m}$ , I.D. = 150  $\mu\text{m}$ ) which is attached to a black anodized aluminum block to provide thermal stability. In order to completely immobilize the capillary to prevent strain or movement, adhesive is applied to each end of the temperature controlled block, permanently affixing the capillary to the block. A sample injection port (Upchurch Scientific) was used to introduce analytes and was immobilized by clamping it to a 4ft x 3ft optical breadboard (Newport Corp). The temperature of the capillary and aluminum block is controlled by an ILX Lightwave Peltier thermoelectric cooler, (model LDC 3722B).

A length of 0.9 mm for both sample and reference regions was chosen with a separation distance of 0.1 mm. The resulting fringe pattern is evaluated using a cross correlation algorithm[238]. Because the regions are adjacent and are part of a continuous channel of fluid, the separation distance of the two regions can be adjusted to a negligible distance, thus optimizing thermal continuity between the sample and reference. Also, in this BSI configuration, since a *single* capillary (channel) is employed, there is a high probability that the interferometers used for the S/R measurement are optically and physically uniform, therefore having similar response functions.

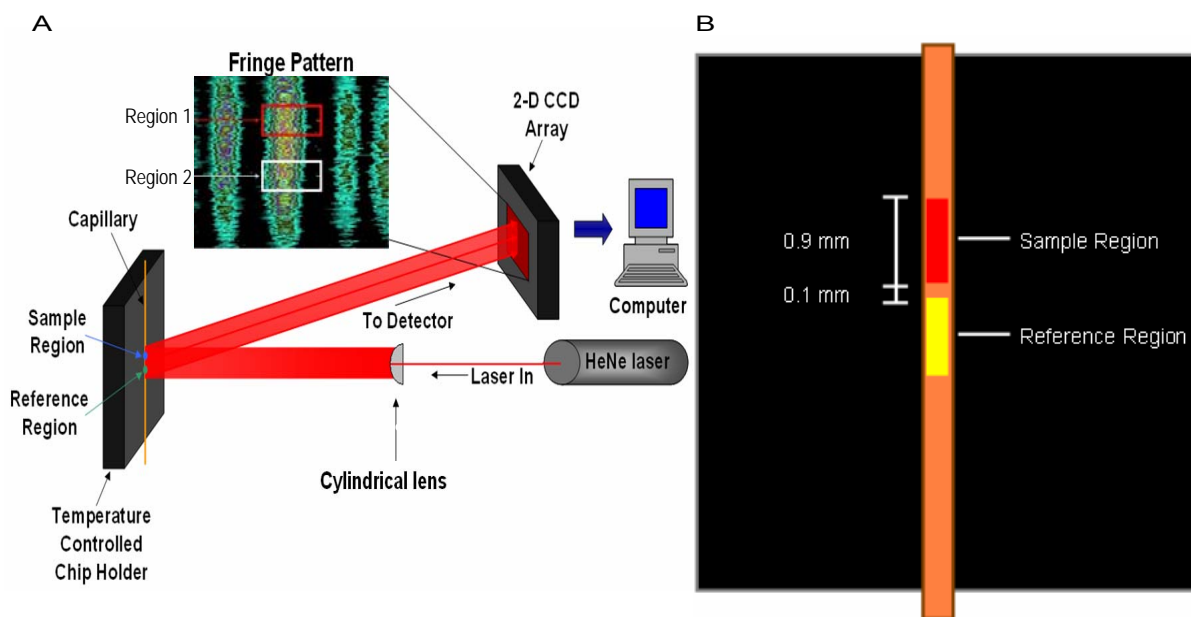


Figure 7.1: Block diagram of the SBM-BSI optical train (A) and closeup of sensing region (B)

#### 7.4 Results:

The following preliminary experiments show that the elongated fringe pattern of SCSR-BSI responds uniformly to random noise and changes in temperature and concentration. This is a requirement for reference compensation to be effective.

To evaluate SCSR-BSI noise compensation, long and short term noise was evaluated by introducing water into the capillary, and allowing it to reach thermal equilibrium with the capillary holder. Once equilibrium was established, the baseline was set to zero and the fringe position was monitored in two regions of the elongated backscatter fringe pattern for various lengths of time

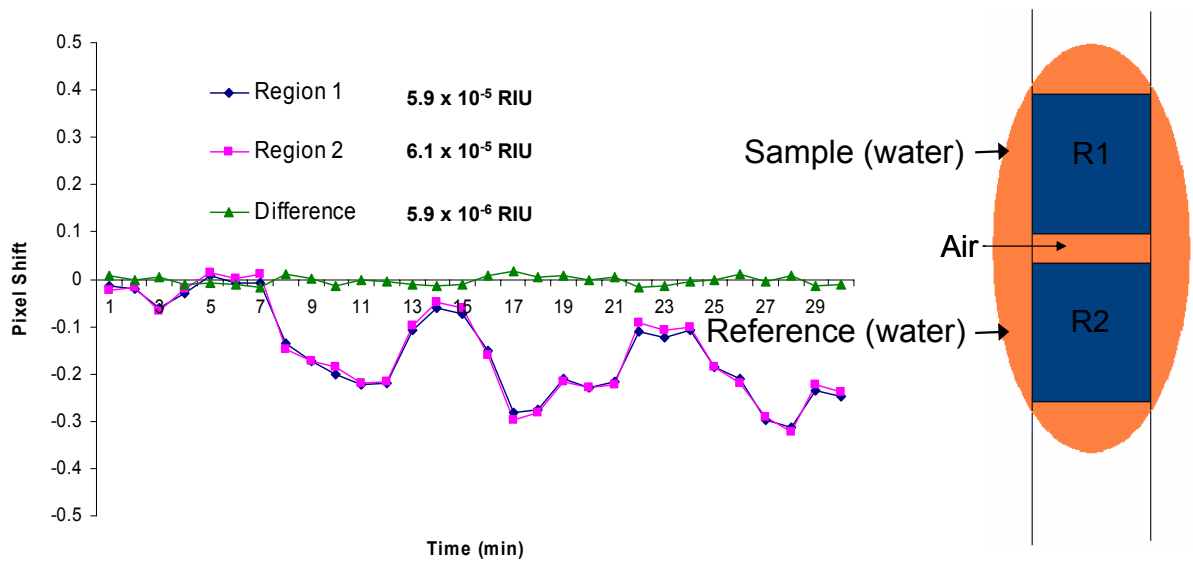


Figure 7.2: Plot of instrumental noise covering an average assay evaluation time of 30 minutes.

ranging from 15 seconds to 30 minutes (Figure 7.2). The position of each region was measured using a cross-correlation algorithm.[238]

Any excursion from the baseline corresponds to instrumental or environmental noise, with the magnitude of this noise defining the threshold of performance. Compensation was carried out by simply subtracting the BSI signal of the reference region (R1) from that of the sample region (R2) at each data point in real time. Approximately 100 data points were collected each second. As shown in figure 7.2, the individual regions report changing conditions with time, leading to both short-term and long-term noise in the instrument. Quantitatively, the long-term noise or drift (i.e. standard deviation) of regions 1 and 2 during a 30 minute interval, representative of the length of time required to perform a complete assay, was 0.097149 pixels and 0.101237 pixels or  $5.9 \times 10^{-5}$  RIU and  $6.1 \times 10^{-5}$  RIU respectively. Compensation provided an improvement of an order

of magnitude in system noise, the difference in standard deviation being 0.009659 or  $5.9 \times 10^{-6}$  RIU.

To further evaluate the performance of SCSR-BSI, calibration curves were generated by simply changing the temperature of the flow cell and the fluid therein. In this determination the temperature controller was set to 24.0°C, a 4 mM glycerol sample was introduced and allowed to equilibrate for one minute before the position of regions 1 and 2 of the elongated fringe were recorded. The temperature was then increased by 0.5°C and the system was allowed to equilibrate for 30 seconds at which time another image was recorded. This process was repeated to cover a two degree temperature range from 24.0-26.0°C as shown in Figure 7.3. Given the fact that the CRC handbook provides a

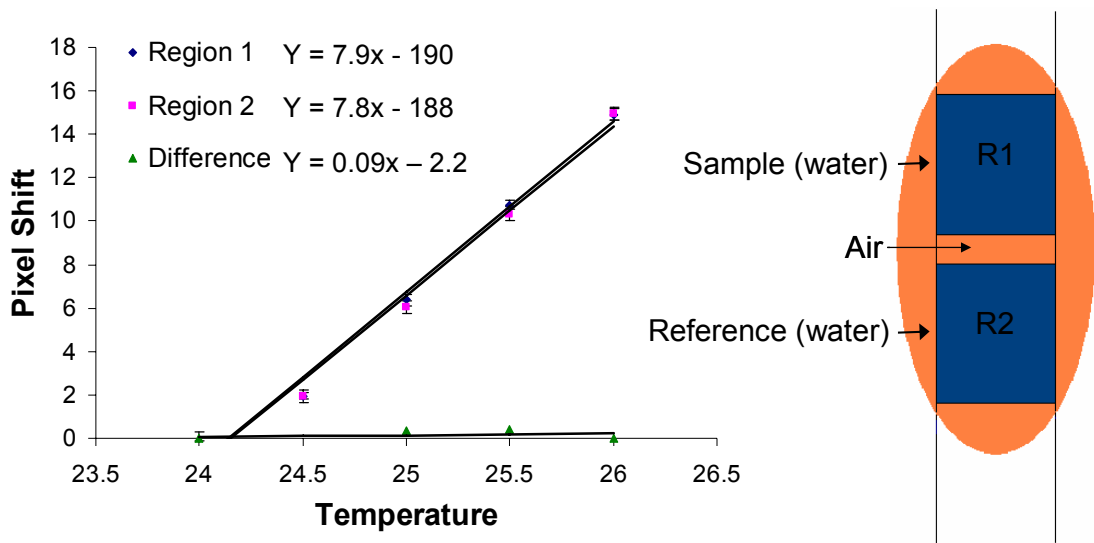


Figure 7.3: Calibration curve of two separate regions of the capillary using a 4 mM solution of glycerol at temperatures ranging from 24-26 °C

$dn/dT$  value for glycerol of  $3.2 \times 10^{-4}$  RIU/ $\Delta^\circ\text{C}$ , the uncompensated signal yielded an RI change  $6.4 \times 10^{-4}$  RIU over a two degree temperature change. Also taking into account that the SCSR-BSI yielded a 7.8 pixel shift over the same temperature range, we can correlate the instrument signal to refractive index. So, if a  $6.4 \times 10^{-4}$  RIU shift correlates to a 7.8 pixel shift, the SCSR-BSI instrument measures  $8.2 \times 10^{-5}$  RIU per pixel. However, taking the difference of these two sampling regions of the same capillary afforded compensation of nearly two orders of magnitude, or  $7 \times 10^{-6}$  RIU over the course of the experiment, which took roughly 30 minutes to perform. This experiment shows that the sample and reference configuration compensated for relatively large changes in refractive index of the solution, in this case as generated by changes in temperature.

Expanding on these studies, analyte calibration curves for the sample and reference regions were created. Glycerol was chosen as the analyte because the refractive index at various concentrations is well known, has been shown to change linearly with respect to concentration and allows S/N ratio and detection limits to be reported in RIU sensing techniques and configurations of BSI. A calibration curve (Figure 7.4) was created using aqueous solutions of glycerol ranging in concentration from 0.0 - 5.0 mM. In this case, solutions of glycerol were introduced into region 1 of the capillary, and water, used as a reference, was introduced into region 2 of the capillary. Glycerol and water aliquots were separated by a small air bubble. Detection was performed by interrogating regions 1 and 2 of the fringe pattern (Figures 7.1 & 7.4), 0.1 millimeters apart and



0.9 mm long. Finally, the position of each region as a function of concentration was measured for 15 seconds.

The calibration curve produced by the SBSR-BSI under conditions meant to evaluate environmental compensation. Here the limits of quantification for regions one and two were  $4.8 \times 10^{-6}$  and  $5.4 \times 10^{-6}$  RIU respectively. These values compare favorably to limits of quantification typically obtained using a single-channel configuration. As desired, Figure 7.4 shows that both regions of the elongated fringe pattern have nearly identical slopes of response vs. concentration (0.29 pixels/mM glycerol). The response of the compensated signal is 3.4 pixels/ $\mu$ M glycerol, which corresponds to  $1.105 \times 10^{-8}$  RIU. In other

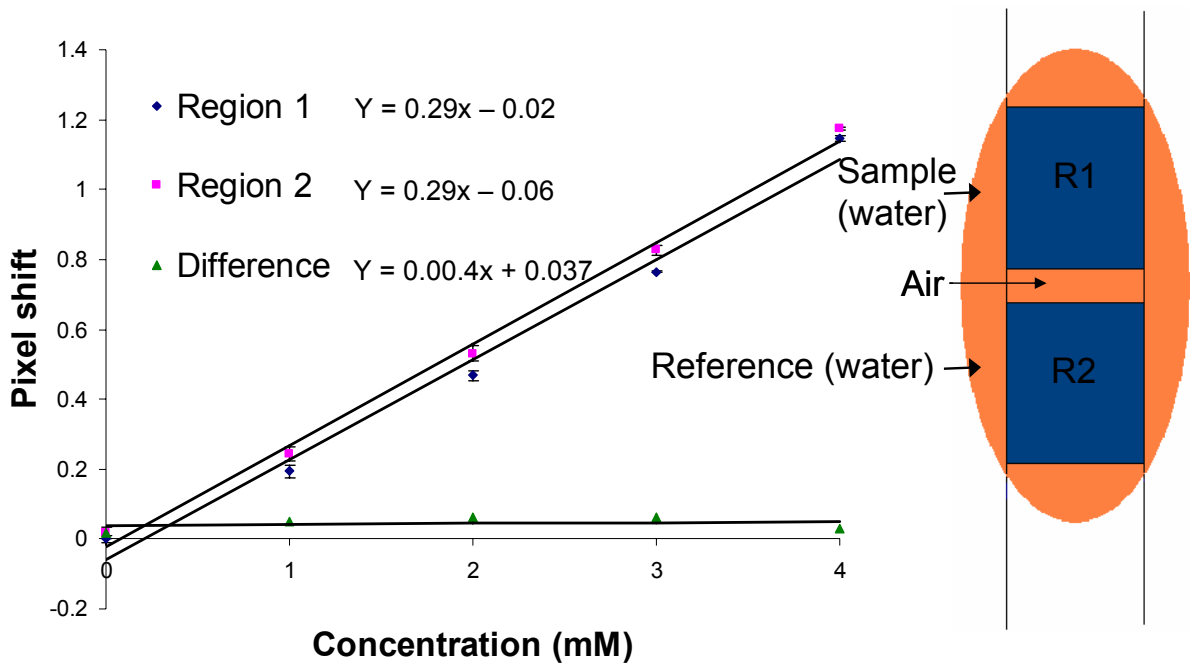


Figure 7.4: Glycerol calibration curve interrogating two separate regions of the elongated fringe pattern.

words, this configuration of BSI would allow the detection of a ca.  $1 \times 10^{-8}$  change in refractive index, which for glycerol would be 1.1  $\mu\text{M}$  glycerol and for a protein like Cyfra 21-1 it would be roughly 1  $\mu\text{M}$ . This experiment illustrates that the interrogated regions along the capillary/channel in the SCSR-BSI configuration respond uniformly to changes in concentration.

In the experiments described above I evaluated the system for long term (30 min) and short-term noise (15 seconds) and for uniformity of response to temperature and concentration by having the two regions being interrogated containing the same sample. Here I investigate performance of SCSR-BSI in a manner identical to that used when performing an assay. Now the two zones of fluid are of a different composition, eg. solutions with and without the analyte. Region 1 contained a sample of glycerol and region 2 contained water used to make the glycerol solution, the reference. As before, injections were made by injecting a small aliquot of reference solution, followed by an air bubble, and finally an aliquot of the sample. The position of the fringes for both sample region and the reference was quantified and the difference was determined for all concentrations in triplicate. To challenge the system and evaluate performance under a worst-case situation, the analysis was performed *without active temperature compensation*.

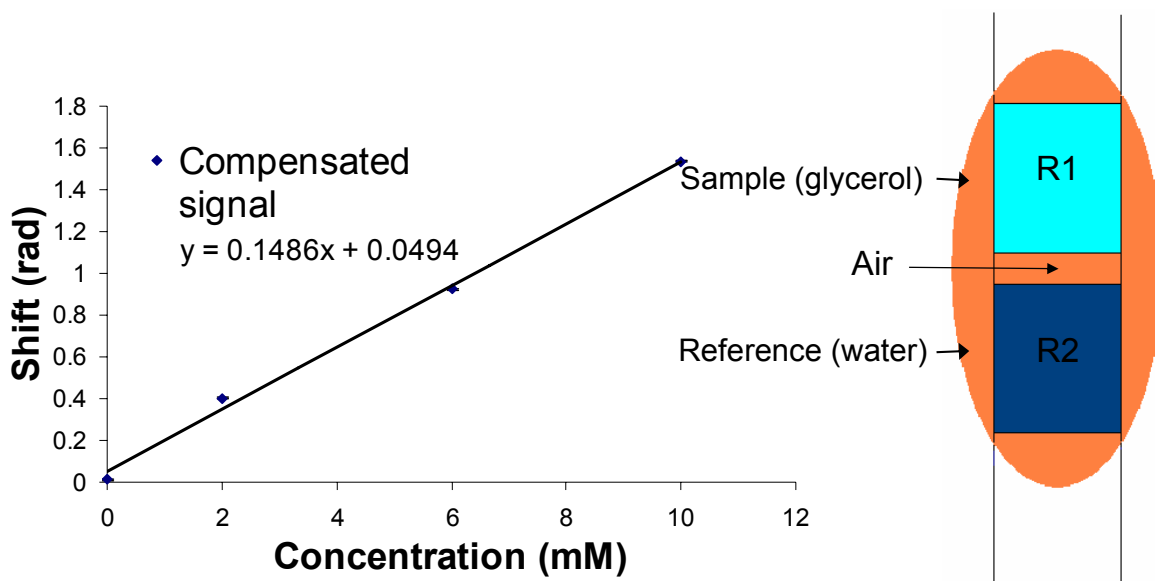


Figure 7.5: Calibration curve where region 1 contains water as a reference and region 2 contains varying concentrations of glycerol. Limit of quantification =  $8.2 \times 10^{-7}$  RIU without temperature compensation

The resulting calibration curve, shown in figure 7.5, is linear ( $R^2=0.998$ ) with a response of 1344 pixels/RIU. The  $3\sigma$  limit of quantification was found to be  $8.2 \times 10^{-7}$  RIU over a 30 minute timeframe *without temperature compensation*. These values are competitive with the standard non-multiplexed format without the necessity of precise temperature control or vibrational isolation. A large hurdle to developing a commercially available, user-friendly device is the ability to operate the instrument in a setting where precise light and temperature control are not feasible. The fact that SCSR-BSI operates with good sensitivity and S/N makes it ideal for a bench-top clinical setting.

## **7.5 Summary and future directions**

Though preliminary, the results presented in this chapter illustrate the benefits the SCSR-BSI design showing that a high level of compensation for short and long-term noise can be obtain in real-time. The new BSI design allows for the sample and reference to be interrogated at one time, decreasing assay time considerably. Furthermore, the design significantly relaxes the need for active temperature control, paving the way for deployment of the device in a wide variety of environments such as the near-patient setting. Finally, and importantly, the optical train is simpler than previous two capillary/channel designs, facilitating ease of alignment and optimal instrument performance.

Continuing work has focused on employing novel beam elongation optics that maintain collimation and sample introduction methods that mimic the nanodrop spectrophotometer, allowing for samples to be directly introduced into a microfluidic chip. Furthermore, space multiple (i.e. multiplex) operation should now be relatively easy to accomplish with BSI by simply expanding the beam further and designing a fluidic method that facilities the introduction several sample/reference pairs.

It should be noted that the limit of quantification, sensitivity and other performance values were measured on the instrument in an open room subject to many sources of noise such as stray light from computer monitors, air current and room temperature fluctuations. Encasing the instrument within a box will help to isolate it from the noise sources that are present in the ambient

environment. No doubt these modifications will improve the signal to noise ratio of the instrument and allow for lower analyte concentrations to be quantified.

For SCSR-BSI to become fully effective, sample introduction must be improved so that multiple aliquot plugs can be introduced reproducibly, and in a user-friendly manner. As a first step towards that end, a chip was created that contains a channel that is separated by a small hole that passes completely through the channel. Through capillary action, a drop can be lowered onto an inlet hole at either end of the channel, allowing the sample to be drawn up to but not beyond the hole in the middle. This design, however, limits the instrument to a single sample and a single reference aliquot per determination. To further increase the throughput, or number of samples analyzed per unit time or simultaneously, a system that can introduce droplets in a fashion that is tunable in the number and size of sample plug is needed. This process must be done without inter-sample mixing, in a volume-constrained manner, with each sample separated in some chemically inert way, e.g. a by a drop of oil or air. Several methods show promise, microfluidic droplet production and manipulation and digital microfluidics, which uses small electrical currents to manipulate the movement and size of drops. The end result should be fully automated, which will enable researchers to simply load analytes into individual reservoirs, allowing the instrument to draw up, mix, and analyze samples automatically.

## CHAPTER 8

### CONCLUSIONS

Backscattering interferometry is a distinctive and versatile instrument that employs a simple optical train to perform highly sensitive, label-free molecular interaction measurements. The unique design of BSI allows for measurements to be performed in either a heterogeneous (surface-immobilized) or homogeneous (free-solution) format in a wide variety of complex matrices.

Surface-immobilized studies performed in this dissertation (Chapter II) measured the relative binding affinities of several carbohydrate – lectin pairs. Because BSI is not mass sensitive, these measurements were performed with the 100kDa lectin attached to the surface, rather than the sugar as needed in other techniques [239, 240]. Additionally, single or multiple layers of avidin provided spacing between the channel surface and the binding sites in order to create a system that more closely resembles the native environment. Finally, the binding affinity of each carbohydrate-lectin pair was measured in free-solution. This study is significant in that it provides a direct comparison to heterogeneous measurements and unprecedented insight into the effect that immobilization has on binding affinity.

Beyond the surface-based lectin studies, a large portion of this work focused on capitalizing on the exceptional sensitivity of BSI in the simpler homogeneous format, detecting tens of thousands of molecules and monitoring

interactions with picomolar to low nanomolar detection limits in complex matrix such as cell lysate and human serum (Chapters IV and V). Additionally, BSI has made it possible to detect disease-specific biomarkers at concentrations previously unattainable by gold standard methods such as ELISA, while consuming significantly less sample volume.

The ability of BSI to perform measurements in complex matrices suggests that it may be possible to use BSI as a serum biomarker detector in a clinical setting. This potential use was tested using human serum samples from patients with non-small cell lung cancer (Chapter V). A panel of samples was tested using commercially available antibodies and showed sensitivity, selectivity, and accuracy when compared with traditional clinical tests. While additional investigations are needed before BSI can be used in clinical testing, its potential for the use in performing rapid diagnostic tests have been clearly demonstrated.

BSI was also been used to measure the interaction of many different aptamers and their small molecule ligands or protein (Chapter III). The binding affinities for the pairs were determined and the specificity of the aptamers was also demonstrated. The ability of BSI to measure aptamer interactions is important because of their growing applications. Antibody interactions currently play a large role in biological and biochemical research and the replacement of antibodies with aptamers in these fields is growing. Therefore a method to characterize the interactions between aptamers and target molecules quickly and efficiently is needed. BSI fits this need well, demonstrating the ability to

accommodate free-solution, label-free binding assays using only a small amount of sample.

BSI was also applied to the study of allosteric interactions, a phenomenon that is best measured in the native state [2, 6, 52, 241](Chapters III and VI). Despite the fact that modifications affect or even inhibit allostery, current methods require some type of labeling or immobilization of one of the binding partners. Here we were able to not only quantify the allosteric effect of several interactions in a free-solution, label-free environment, but identify ligands which were originally thought to be GABA-specific that bind to the CXCR4 receptor. The ability to study allosteric interactions in this challenging format can provide accurate insight into many important neurological pathways, and BSI has illustrated that this is now possible.

In addition to studying unique and challenging binding systems, efforts were made to refine the BSI optical train so that it is more robust, temperature-insensitive and capable of measuring multiple interactions simultaneously with an integrated internal reference. This work showed that decreased the total assay time, increased sensitivity by over an order of magnitude, and real-time temperature compensation over large temperature variations (Chapter VII) was possible.

BSI is unique, powerful approach to biosensing and has enabled previously impossible molecular interactions studies. BSI works in free solution and with little *a priori* knowledge of the binding pair, allowing this technique to perform novel binding affinity determinations on uncharacterized molecules. BSI



had already been shown to be a sensitive technique for quantifying molecular interactions and the work presented here extended the limits, showing that low picomolar detection limits could be attained in human serum. The range of unique applications that BSI is capable of has also been broadened beyond expectations. The ability to monitor interactions with lipoparticles containing ion channels and GPCR receptors was once speculation, but has now been proven possible as seen in the work reported in this thesis. Further experimentation is needed to fully understand the source of the BSI signal with respect to the changes that occur within biomolecules during the binding process, though properties such as the dipole moment, waters of hydration, and conformation are likely sources. BSI has the ability to shift the paradigm when attempting to quantify affinity, determine immobilization perturbation, or screen for binding. As the technology continues to develop, the potential for BSI, whether used in a laboratory for the development of new and better drugs, in a doctor's office for the diagnosis of diseases, or in the field to study environmental contaminants, is extensive.

## APPENDIX A

### Concanavalin A surface immobilization chemistry:

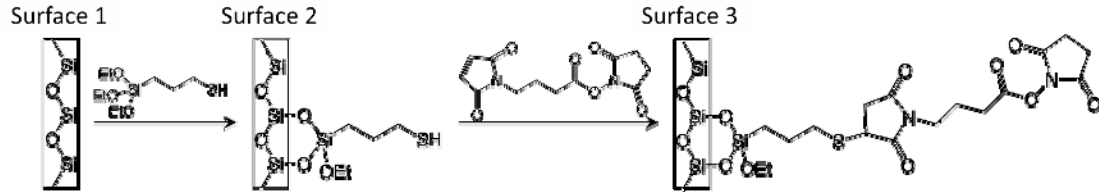


Figure A.1: First, the glass channel is cleaned with 10% KOH in methanol (Surface 1), then a thiol-modified surface (Surface 2) is created using MEPTES. Finally, the surface is activated with GMBs to yield tethered *N*-hydroxysuccinimide ester groups (Surface 3), which are used to immobilize a protein. [10]

### Free-solution Binding Determinations

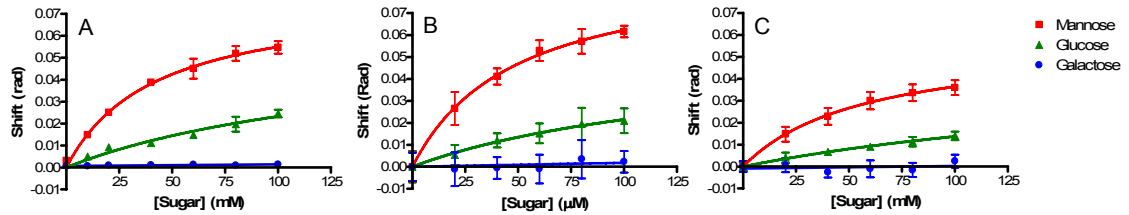


Figure A.2: (A) Mannose and glucose bind to ConA which has been directly attached to the channel surface with  $1/K_{ads}$  values of  $41.8 \pm 7.8 \mu\text{M}$  and  $154.9 \pm 88.3 \mu\text{M}$ , respectively. (B) Mannose and glucose bind to surface-immobilized ConA  $7.17 \pm 1.08 \text{ nm}$  from the surface with  $1/K_{ads}$  values of  $48.5 \pm 4.5 \mu\text{M}$  and  $145.4 \pm 43.0 \mu\text{M}$ , respectively. (C) Mannose and glucose bind to surface-immobilized ConA  $20.35 \pm 1.19 \text{ nm}$  from the surface with  $1/K_{ads}$  values of  $57.7 \pm 5.0 \mu\text{M}$  and  $240.7 \pm 66.9 \mu\text{M}$ , respectively.[10]

## APPENDIX B

### B.1 Computational model of thrombin-aptamer interactions[6]

We created a model to understand the allosteric effect of binding by the two aptamers to thrombin. Starting from the 2.9-Å resolution X-ray crystal structure of the Bock-thrombin complex (1HUT.pdb), we added a model of the Tasset aptamer, following the procedure of Tasset *et al.* 1997[9]. We built the aptamer structure by modeling the G-quadruplex of Tasset (sequence: AGTCCGTGGTAGGGCAGGTTGGGGTACT) on the corresponding coordinates from the Bock structure (sequence: GGTTGGTGTGGTTGG). The 11 additional nucleotides of Tasset at the 5' and 3' termini, which do not have corresponding structure in the Bock aptamer, were modeled as a duplex (B-form DNA) and relaxed using 1 nanosecond of annealing in AMBER 10 with the ff99bsc0 force field and the generalized Born continuum solvent model. This structure was then docked to the complex using the cross-linking data, which imply a contact between residue Phe245 and nucleotide T12. The phosphate backbone was positioned to contact the positively-charged surface patch formed by Arg126, Lys236, Lys240 and Arg93. We refined the docking pose using RosettaDock in all-atom dock\_pert mode to determine the lowest-energy configuration.

The model suggests that the binding sites of the two aptamers, which reside at opposite ends of the substrate-binding cleft, are connected by a framework of rigid secondary-structural elements. Previous studies have found evidence for allosteric linkage between exosites I and II using fluorescently-labeled hirudin and a prothrombin fragment. It is possible that the allostery observed here between the Bock and Tasset aptamers is mediated by the same mechanism, which we postulate to be transmission of motional signals through the rigid structure inside the protein from one exosite to the other.

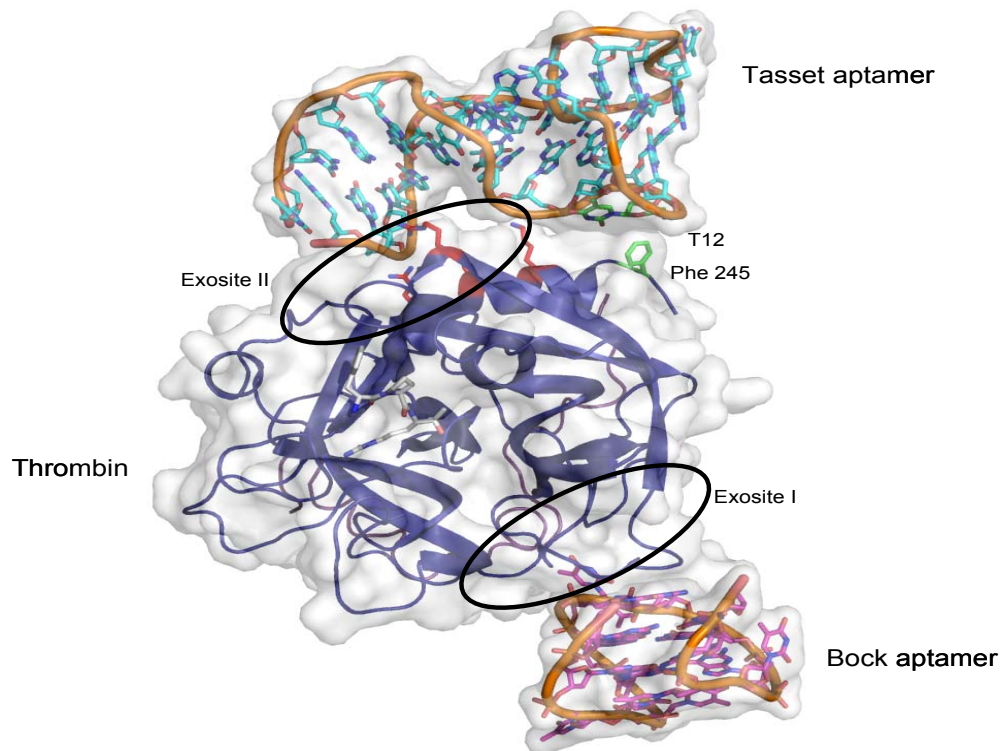


Figure B.1: An illustration for inter-site communication in thrombin. Human  $\alpha$ -thrombin is shown with blue ribbons in standard orientation. The inhibitor PPACK, displayed in gray sticks, occupies the central active-site cleft. Exosites I (fibrinogen recognition exosite) and II (heparin-binding site) are indicated with ovals. The Bock DNA aptamer is shown in magenta at exosite I, using the coordinates of the 2.9-Å resolution Bock-thrombin complex from Padmanabhan et al. 1993 (1HUT.pdb). A model of the Tasset DNA aptamer is shown in cyan, positioned according to Tasset et al. 1997 to maintain a contact between the cross-linked residue Phe245 with nucleotide T12 (highlighted in green), and to appose the phosphate backbone with four positively-charged surface residues (in red) near exosite II.[6]

## APPENDIX C

### C.1 Sequences of the full-length RNA target and the mismatched target used in nucleotide detection [3]

Full length respiratory syncytial virus (RSV) N gene RNA sequence used in these studies (5' - 3'). Regions complementary to the probes used in these studies are underlined and colored.

CAAAAACCCCUCAAGACCCGUUUAGAGGCCCAAGGGGUUAUGCUAGUU  
AUGCGGCCGCUGCAGGUCGACGGAUCCUCAAGCUCUACAUCAUUAUCU  
UUUGGAUUAAGCUGAUGUUUGAUAGCCUCUAGUUCUUCUGCUGUCAAGU  
CUAGUACACUGUAGUUAUCACACCAUUUUUCUUUGAGUUGUUCAGCAUUA  
GCCUUUGCUGCAUCAUUAAGAUUCUUGAUUCCUCGGUGUACCUCUGUACU  
CUCCCAUUAUGCCUAGGCCAGCAGCAUUGCCUAAUACUACACUGGAGAAG  
UGAGGAAAUUGAGUCAAAAGAUAAUAAUGAUGCUUUUGGGUUGUCAAUUA  
AUGGUAGAAUCCUGCUUCACCACCCAAUUUUUGGGCAUUAUCAUAAACCU  
CAACAACUUGUUCUUCUUCUGCUUGCACACUAGCAUGUCCUAAUAAUA  
UUUUUAACUGAUUUUGCUAAGACUCCCCACCGUAACAUCACUUGCCCUGC  
ACCAUAGGCAUUCAUAAACAUAUCCUGCAAAAUCCCUUCAACUCUACUGC  
CACCUCUGGUAGAAGAUUGUGCUAUACCAAAAUGAACAAAACAUCUAUA  
AAGUGGGGAUGUUUUUCAACACUUCAUAGAAGCUGUUGGCCUAUGUCCU  
UGGGUAGUAAGCCUUUGUAACGUUUCAUUUCAUUUUUUAGGACAUUAUUA  
GCUCUCUAUACACGGCUGUAAGACCA GAUCUGUCCCCUGCUGCUAAUU  
UAGUUAUUAACUAAUGCUGCUAUACAUAUUAUCAUCCACAUAUCAGGA  
GAGUCAUGCCUGUAUUCUGGAGCUACCUCUCCAUUUCUUUUAGCAUUU  
UUUUGUAGGAUUUUCUAGAUUCUAUCUCAAGUUGAUUUUGAAUUUCAGUU  
GUUAAGCUUGCCAUGUUAACACUUCAAAUUAUCAUUUCUUUUCCAUAUAAU  
GUCUUGACGAUGUGUUGUUAUCAUCUACUCCAUUUGCUUUUACAUGAUUAU  
CCCGCAUCUCUGAGUAUUUUUAUGGUGUCUUCUCUCCUAACCUAGACA  
UCGCAUUAACAUAACCUAUUAACCCAGUGAAUUUAUGAUUAGCAUCUUCU  
GUGAUUAUAACAUGCCACAUAACUUAUUGAUGUGUUCUGCACAUCAUA  
AUUAGGAGUAUCAAUACUAUCUCCUGUGCUCCGUUGGAUGGUGUAUUUG  
CUGGAUGACAGAAGUUGAUCUUUGUUGAGUGUAUCAUUAACUUGACUU  
UGCUAAGAGCCAUAUUGAAUUCGGCCUCCAUGGCCAUUAUGCAGGUCCUC  
CUCUGAGAUCAGCUUCUGCUCCUCCAUGAUGGCGGCUCGCC

Grey: RSVN(1070-1091)

Teal: RSVN(957-983)

Light purple: RSVN(843-872)

Brown: RSVN(800-821)

Red: RSVN(755-774)

Light blue: RSVN(603-622)

Light green: RSVN(531-551)  
Light brown: RSVN(425-444)  
Pink: RSVN(308-329)  
Purple: RSVN(286-307)  
Blue: RSVN(264-285)  
Green/Orange: RSVN(242-263)  
Orange: RSVN(242-256)  
Orange/Green/Blue: RSVN(242-285)  
Orange/Green/Blue/Purple/Pink: RSVN(242-329)  
Tan: RSVN(193-214)  
Maroon: RSVN(4-29)

RNA target sequences containing mismatched nucleotides (5' - 3'). Mismatched nucleotides are indicated in bold font.

0 mismatches: UAUCCCGCAUCUCUGAGUAUUU  
1 mismatch: UAUCCCGCAU**G**UCUGAGUAUUU  
3 mismatches: UAUC**G**CGCAU**G**UCUGACUAUUU  
5 mismatches: UAUC**G**CG**G**AU**G**UC**A**GACUAUUU  
7 mismatches: **U**UUC**G**CG**G**AU**G**UC**A**GACU**A**AUU  
10 mismatches: **U**UUC**G****G****G**AU**G**AC**A**CACUA**A**AUU

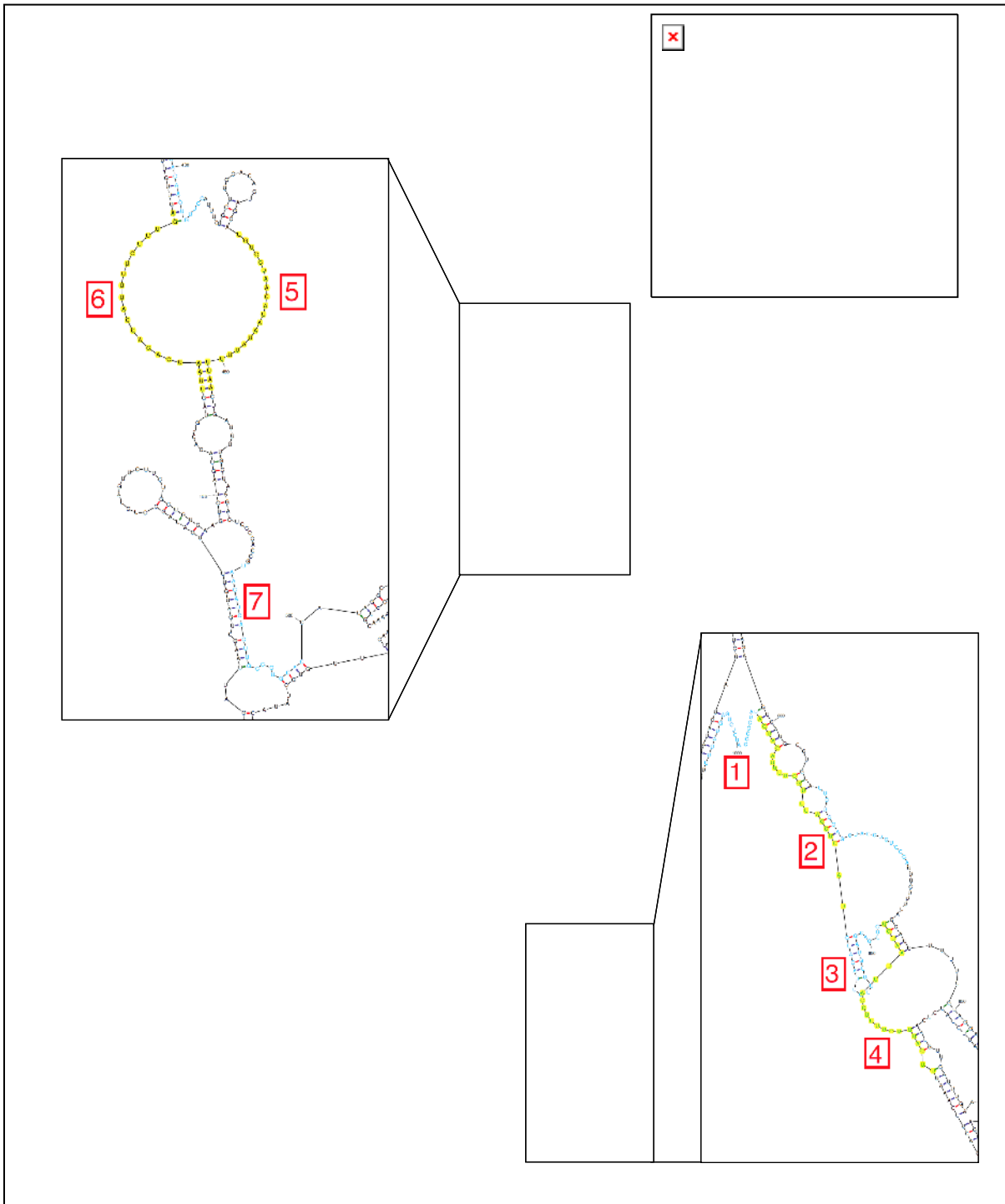
**Table C.1: Sequence of each oligonucleotide probe used in RNA detection[3]**

	Probe name*	Probe length (nucleotides)	Sequence (5' – 3')	
varying DNA probe length	RSVN(242-258)	15	AAATACTCAGAGATG	
	RSVN(242-263)	22	AAATACTCAGAGATGCGGGATA	
	RSVN(242-285)	44	AAATACTCAGAGATGCGGGATATCATGTAAAA-GCAAATGGAGTA	
	RSVN(242-329)	88	AAATACTCAGAGATGCGGGATATCATGTAAAA-GCAAATGGAGTAGATGTAACAACACATCGT-CAAGACATTAATGGAAAAGAAATGAA	
4 consecutive DNA probes	RSVN(242-263)	22	AAATACTCAGAGATGCGGGATA	
	RSVN(264-285)	22	TCATGTAAAAGCAAATGGAGTA	
	RSVN(286-307)	22	GATGTAACAACACATCGTCAAG	
	RSVN(308-329)	22	ACATTAATGGAAAAGAAATGAA	
9 distributed DNA probes	4 distributed DNA probes	RSVN(242-263)	22	AAATACTCAGAGATGCGGGATA
		RSVN(425-444)	20	TGGGAGAGGTAGCTCCAGAA
		RSVN(603-622)	20	ACCCAAGGACATAGCCAACA
		RSVN(755-774)	20	GTGCAGGGCAAGTGATGTTA
	RSVN(4-29)	28	GCTCTTAGCAAAGTCAAGTTGAATGA	
	RSVN(193-214)	22	ATAGGTATGTTATATGCGATGT	
	RSVN(531-551)	21	TGGTCTTACAGCCGTGATTAG	
	RSVN(843-872)	30	GGAACAAGTTGTTGAGGTTTATGAATATGC	
	RSVN(957-983)	27	CTTCTCCAGTGTAGTATTAGGCAATGC	
	4 distributed LNA probes	RSVN(242-263)L	22	AA+ATA+CTC+AGA+GAT+GCG+GGA+TA
RSVN(425-444)L		20	TG+GGA+GAG+GTA+GCT+CCA+GAA	
RSVN(603-622)L		20	AC+CCA+AGG+ACA+TAG+CCA+ACA	
RSVN(755-774)L		20	GT+GCA+GGG+CAA+GTG+ATG+TTA	
Other DNA probes	RSVN(800-821)	22	TTAAAAATATTATGTTAGGACA	
	RSVN(1070-1091)	22	TCAAAGAAAATGGTGTGATTAA	
	RSVN(242-263)SCRAM	22	AAATAAAGGGTATCCGGTCGAA	
	RSVN(264-285)SCRAM	22	AGATGAGAGAATAGTTTCCAAA	

\*The probe name includes the position of the complementary sequence of the respiratory syncytial virus (RSV) nucleocapsid (N) gene in reference to the start codon. Locked nucleic acid (LNA) sequences are denoted with plus signs (+) preceding the modified nucleotides.

## C.2 Full length RNA target sequence[3]

The five lowest energy *mfold* RNA folding structures predicted for the ~1300 nucleotide RSV N gene RNA sequence. The binding regions of the probes used in these studies are highlighted in yellow or blue and numbered 1 - 7. Legends in the top right of each structure list each probe evaluated and the number of unpaired bases predicted in the corresponding binding region





## REFERENCES:

1. Guyon, A.K., Q.; Olmsted, I.R.; Sandoz, G.; Bornhop, D.J.; Nahon, J-L, *Baclofen and Other GABA<sub>B</sub> Receptor Agents Are Allosteric Modulators of the CXCL12 Chemokine Receptor CXCR4*. The Journal of Neuroscience, 2013. **33**(23).
2. Olmsted, I.R., A. Kussrow, and D.J. Bornhop, *Comparison of free-solution and surface-immobilized molecular interactions using a single platform*. Anal Chem, 2012. **84**(24): p. 10817-22.
3. Adams, N.M., et al., *The effect of hybridization-induced secondary structure alterations on RNA detection using backscattering interferometry*. Nucleic Acids Res, 2013.
4. Mann, D.A., *Probing low affinity and multivalent interactions with surface plasmon resonance: Ligands for concanavalin A*. Journal of the American Chemical Society, 1998. **120**(41): p. 10575-10582.
5. Smith, E.A., et al., *Surface plasmon resonance imaging studies of protein-carbohydrate interactions*. J Am Chem Soc, 2003. **125**(20): p. 6140-8.
6. Olmsted, I.R., et al., *Measurement of aptamer-protein interactions with back-scattering interferometry*. Anal Chem, 2011. **83**(23): p. 8867-70.
7. Bock, L.C., et al., *Selection of Single-Stranded-DNA Molecules That Bind and Inhibit Human Thrombin*. Nature, 1992. **355**(6360): p. 564-566.
8. Tsiang, M., et al., *Selection of a suppressor mutation that restores affinity of an oligonucleotide inhibitor for thrombin using in vitro genetics*. J Biol Chem, 1995. **270**(33): p. 19370-6.
9. Tasset, D.M., M.F. Kubik, and W. Steiner, *Oligonucleotide inhibitors of human thrombin that bind distinct epitopes*. J Mol Biol, 1997. **272**(5): p. 688-98.
10. Olmsted, I.R., A. Kussrow, and D.J. Bornhop, *Comparison of Free-Solution and Surface-Immobilized Molecular Interactions Using a Single Platform*. Analytical Chemistry, 2012. **84**(24): p. 10817-10822.
11. Mandal, D.K., N. Kishore, and C.F. Brewer, *Thermodynamics of lectin-carbohydrate interactions. Titration microcalorimetry measurements of the binding of N-linked carbohydrates and ovalbumin to concanavalin A*. Biochemistry, 1994. **33**(5): p. 1149-56.
12. Schwartz, A.G., et al., *The molecular epidemiology of lung cancer*. Carcinogenesis, 2007. **28**(3): p. 507-18.
13. Foa, P., et al., *Tumour markers CEA, NSE, SCC, TPA and CYFRA 21.1 in resectable non-small cell lung cancer*. Anticancer Research, 1999. **19**(4C): p. 3613-3618.
14. Kulpa, J., et al., *Carcinoembryonic antigen, squamous cell carcinoma antigen, CYFRA 21-1, and neuron-specific enolase in squamous cell lung cancer patients*. Clinical Chemistry, 2002. **48**(11): p. 1931-1937.
15. Malima, A., et al., *Highly sensitive microscale in vivo sensor enabled by electrophoretic assembly of nanoparticles for multiple biomarker detection*. Lab Chip, 2012. **12**(22): p. 4748-54.
16. Molina, R., et al., *Tumor markers (CEA, CA 125, CYFRA 21-1, SCC and NSE) in patients with non-small cell lung cancer as an aid in histological diagnosis and*

- prognosis. Comparison with the main clinical and pathological prognostic factors.* Tumour Biol, 2003. **24**(4): p. 209-18.
17. Stern, E., et al., *Label-free biomarker detection from whole blood.* Nat Nanotechnol, 2010. **5**(2): p. 138-42.
  18. Engvall, E. and P. Perlmann, *Enzyme-Linked Immunosorbent Assay (Elisa) Quantitative Assay of Immunoglobulin-G.* Immunochemistry, 1971. **8**(9): p. 871-&.
  19. Diaz, M.R. and J.W. Fell, *High-throughput detection of pathogenic yeasts of the genus Trichosporon.* Journal of Clinical Microbiology, 2004. **42**(8): p. 3696-3706.
  20. Jain, V.K. and I.T. Magrath, *A Chemiluminescent Assay for Quantitation of Beta-Galactosidase in the Femtogram Range - Application to Quantitation of Beta-Galactosidase in Iacz-Transfected Cells.* Analytical Biochemistry, 1991. **199**(1): p. 119-124.
  21. Garber, E.A.E., K.V. Venkateswaran, and T.W. O'Brien, *Simultaneous Multiplex Detection and Confirmation of the Proteinaceous Toxins Abrin, Ricin, Botulinum Toxins, and Staphylococcus Enterotoxins A, B, and C in Food.* Journal of Agricultural and Food Chemistry, 2010. **58**(11): p. 6600-6607.
  22. Lequin, R.M., *Enzyme Immunoassay (EIA)/Enzyme-Linked Immunosorbent Assay (ELISA).* Clinical Chemistry, 2005. **51**(12): p. 2415-2418.
  23. Kai, J.H., et al., *A novel microfluidic microplate as the next generation assay platform for enzyme linked immunoassays (ELISA).* Lab on a Chip, 2012. **12**(21): p. 4257-4262.
  24. Bartlett, J.M. and D. Stirling, *A short history of the polymerase chain reaction.* Methods Mol Biol, 2003. **226**: p. 3-6.
  25. Saiki, R.K., et al., *Primer-directed enzymatic amplification of DNA with a thermostable DNA polymerase.* Science, 1988. **239**(4839): p. 487-91.
  26. Saiki, R.K., et al., *Enzymatic amplification of beta-globin genomic sequences and restriction site analysis for diagnosis of sickle cell anemia.* Science, 1985. **230**(4732): p. 1350-4.
  27. Klein, D., *Quantification using real-time PCR technology: applications and limitations.* Trends in Molecular Medicine, 2002. **8**(6): p. 257-260.
  28. Louie, M., L. Louie, and A.E. Simor, *The role of DNA amplification technology in the diagnosis of infectious diseases.* Canadian Medical Association Journal, 2000. **163**(3): p. 301-309.
  29. Fonseca-Coronado, S., et al., *Specific detection of naturally occurring hepatitis C virus mutants with resistance to telaprevir and boceprevir (protease inhibitors) among treatment-naive infected individuals.* J Clin Microbiol, 2012. **50**(2): p. 281-7.
  30. Lanciotti, R.S., et al., *Rapid detection of west nile virus from human clinical specimens, field-collected mosquitoes, and avian samples by a TaqMan reverse transcriptase-PCR assay.* J Clin Microbiol, 2000. **38**(11): p. 4066-71.
  31. Schabereiter-Gurtner, C., et al., *Novel real-time PCR assay for detection of Helicobacter pylori infection and simultaneous clarithromycin susceptibility testing of stool and biopsy specimens.* J Clin Microbiol, 2004. **42**(10): p. 4512-8.
  32. Rapellino, M., et al., *CYFRA 21-1 as a tumour marker for bronchogenic carcinoma.* Eur Respir J, 1995. **8**(3): p. 407-10.

33. Andes, D., A. Pascual, and O. Marchetti, *Antifungal therapeutic drug monitoring: established and emerging indications*. *Antimicrob Agents Chemother*, 2009. **53**(1): p. 24-34.
34. Pascual, A., et al., *Voriconazole therapeutic drug monitoring in patients with invasive mycoses improves efficacy and safety outcomes*. *Clin Infect Dis*, 2008. **46**(2): p. 201-11.
35. Fister, J.C., et al., *Counting single chromophore molecules for ultrasensitive analysis and separations on microchip devices*. *Anal Chem*, 1998. **70**(3): p. 431-7.
36. Haab, B.B. and R.A. Mathies, *Single-molecule detection of DNA separations in microfabricated capillary electrophoresis chips employing focused molecular streams*. *Anal Chem*, 1999. **71**(22): p. 5137-45.
37. Chen, P.-C., *The Contrast Formation in Optical Microscopy*, ed. J.B. Pawley. 2006: Springer, US.
38. Helms, V., *Principles of Computational Cell Biology*. 2008: Wiley-VCH.
39. Harris, D.C., *Quantitative Chemical Analysis*. 2006, W.H. Freeman and Co.: New York. p. 419-44.
40. Zheng, J., *Spectroscopy-based quantitative fluorescence resonance energy transfer analysis*. *Methods in Molecular Biology*, 2006. **337**: p. 65-77.
41. Maurel, D., et al., *Cell-surface protein-protein interaction analysis with time-resolved FRET and snap-tag technologies: application to GPCR oligomerization*. *Nature Methods*, 2008. **5**(6): p. 561-567.
42. Carriba, P., et al., *Detection of heteromerization of more than two proteins by sequential BRET-FRET*. *Nature Methods*, 2008. **5**(8): p. 727-733.
43. Roy, R., S. Hohng, and T. Ha, *A practical guide to single-molecule FRET*. *Nature Methods*, 2008. **5**(6): p. 507-516.
44. Truong, K. and M. Ikura, *The use of FRET imaging microscopy to detect protein-protein interactions and protein conformational changes in vivo*. *Current Opinion in Structural Biology*, 2001. **11**(5): p. 573-578.
45. Chen, H., et al., *Measurement of FRET efficiency and ratio of donor to acceptor concentration in living cells*. *Biophysical Journal*, 2006. **91**(5): p. L39-L41.
46. Lakowicz, J.R., *Principles of Fluorescence Spectroscopy*. 3rd ed. 2006: Springer.
47. Valeur, B., *Molecular Fluorescence: Principles and Applications*. 2001: Wiley-VCH.
48. Jolley, M.E., et al., *Fluorescence Polarization Immunoassay .3. An Automated-System for Therapeutic Drug Determination*. *Clinical Chemistry*, 1981. **27**(9): p. 1575-1579.
49. Zhu, Z.Y., et al., *Single-Stranded DNA Binding Protein-Assisted Fluorescence Polarization Aptamer Assay for Detection of Small Molecules*. *Analytical Chemistry*, 2012. **84**(16): p. 7203-7211.
50. Choi, J.W., et al., *High-Throughput Analysis of Protein-Protein Interactions in Picoliter-Volume Droplets Using Fluorescence Polarization*. *Analytical Chemistry*, 2012. **84**(8): p. 3849-3854.
51. Fields, S., *Proteomics. Proteomics in genomeland*. *Science*, 2001. **291**(5507): p. 1221-4.

52. Pesciotta, E.N., D.J. Bornhop, and R.A. Flowers, *Back-Scattering Interferometry: A Versatile Platform for the Study of Free-Solution versus Surface-Immobilized Hybridization*. Chemistry-an Asian Journal, 2011. **6**(1): p. 70-73.
53. Conway de Macario, E., U.H. Rudofsky, and A.J. Macario, *Surface plasmon resonance for measuring TBP-promoter interaction*. Biochem Biophys Res Commun, 2002. **298**(5): p. 625-31.
54. Jordan, C.E. and R.M. Corn, *Surface Plasmon Resonance Imaging Measurements of Electrostatic Biopolymer Adsorption onto Chemically Modified Gold Surfaces*. Anal Chem, 1997. **69**(7): p. 1449-56.
55. Rich, R.L., et al., *High-resolution and high-throughput protocols for measuring drug/human serum albumin interactions using BIACORE*. Anal Biochem, 2001. **296**(2): p. 197-207.
56. Wegner, G.J., et al., *Fabrication of histidine-tagged fusion protein arrays for surface plasmon resonance imaging studies of protein-protein and protein-DNA interactions*. Anal Chem, 2003. **75**(18): p. 4740-6.
57. Boussaad, S., J. Pean, and N.J. Tao, *High-resolution multiwavelength surface plasmon resonance spectroscopy for probing conformational and electronic changes in redox proteins*. Anal Chem, 2000. **72**(1): p. 222-6.
58. Nelson, B.P., et al., *Surface plasmon resonance imaging measurements of DNA and RNA hybridization adsorption onto DNA microarrays*. Anal Chem, 2001. **73**(1): p. 1-7.
59. Sota, H., Y. Hasegawa, and M. Iwakura, *Detection of conformational changes in an immobilized protein using surface plasmon resonance*. Anal Chem, 1998. **70**(10): p. 2019-24.
60. Schwarz, F.P., et al., *Thermodynamics of monosaccharide binding to concanavalin A, pea (*Pisum sativum*) lectin, and lentil (*Lens culinaris*) lectin*. J Biol Chem, 1993. **268**(11): p. 7668-77.
61. Weatherman, R.V., et al., *Specificity of C-glycoside complexation by mannose/glucose specific lectins*. Biochemistry, 1996. **35**(11): p. 3619-24.
62. Neumann, L., et al., *Functional immobilization of a ligand-activated G-protein-coupled receptor*. Chembiochem, 2002. **3**(10): p. 993-8.
63. Duverger, E., et al., *Carbohydrate-lectin interactions assessed by surface plasmon resonance*. Biochimie, 2003. **85**(1-2): p. 167-79.
64. Haseley, S.R., et al., *Characterization of the carbohydrate binding specificity and kinetic parameters of lectins by using surface plasmon resonance*. Anal Biochem, 1999. **274**(2): p. 203-10.
65. Lundquist, J.J. and E.J. Toone, *The cluster glycoside effect*. Chem Rev, 2002. **102**(2): p. 555-78.
66. Dam, T.K., et al., *Differential solvation of "core" trimannoside complexes of the Dioclea grandiflora lectin and concanavalin A detected by primary solvent isotope effects in isothermal titration microcalorimetry*. J Biol Chem, 1998. **273**(49): p. 32826-32.
67. Williams, B.A., M.C. Chervenak, and E.J. Toone, *Energetics of lectin-carbohydrate binding. A microcalorimetric investigation of concanavalin A-oligomannoside complexation*. J Biol Chem, 1992. **267**(32): p. 22907-11.
68. Hariharan, P., *Basics of Interferometry*. 2007: Elsevier.

69. Fan, X., et al., *Sensitive optical biosensors for unlabeled targets: a review*. Anal Chim Acta, 2008. **620**(1-2): p. 8-26.
70. Baksh, M.M., et al., *Label-free quantification of membrane-ligand interactions using backscattering interferometry*. Nat Biotechnol, 2011. **29**(4): p. 357-60.
71. Bornhop, D.J., et al., *Free-solution, label-free molecular interactions studied by back-scattering interferometry*. Science, 2007. **317**(5845): p. 1732-6.
72. Kussrow, A., et al., *Universal sensing by transduction of antibody binding with backscattering interferometry*. Chembiochem, 2011. **12**(3): p. 367-70.
73. Kussrow, A., C.S. Enders, and D.J. Bornhop, *Interferometric methods for label-free molecular interaction studies*. Anal Chem, 2012. **84**(2): p. 779-92.
74. Kussrow, A., et al., *The potential of backscattering interferometry as an in vitro clinical diagnostic tool for the serological diagnosis of infectious disease*. Analyst, 2010. **135**(7): p. 1535-7.
75. Kussrow, A., et al., *Measurement of monovalent and polyvalent carbohydrate-lectin binding by back-scattering interferometry*. Anal Chem, 2009. **81**(12): p. 4889-97.
76. Latham, J.C., et al., *Photobiotin surface chemistry improves label-free interferometric sensing of biochemical interactions*. Angew Chem Int Ed Engl, 2006. **45**(6): p. 955-8.
77. Latham, J.C., et al., *Free-solution label-free detection of alpha-crystallin chaperone interactions by back-scattering interferometry*. Anal Chem, 2009. **81**(5): p. 1865-71.
78. Su, Y.D., S.J. Chen, and T.L. Yeh, *Common-path phase-shift interferometry surface plasmon resonance imaging system*. Optics Letters, 2005. **30**(12): p. 1488-1490.
79. Ng, S.P., et al., *Differential spectral phase interferometry for wide dynamic range surface plasmon resonance biosensing*. Biosensors & Bioelectronics, 2010. **26**(4): p. 1593-1598.
80. Brosinger, F., et al., *A label-free affinity sensor with compensation of unspecific protein interaction by a highly sensitive integrated optical Mach-Zehnder interferometer on silicon*. Sensors and Actuators B-Chemical, 1997. **44**(1-3): p. 350-355.
81. Prieto, F., et al., *An integrated optical interferometric nanodevice based on silicon technology for biosensor applications*. Nanotechnology, 2003. **14**(8): p. 907-912.
82. Prieto, F., et al., *Integrated Mach-Zehnder interferometer based on ARROW structures for biosensor applications*. Sensors and Actuators B-Chemical, 2003. **92**(1-2): p. 151-158.
83. Schipper, E.F., et al., *The realization of an integrated Mach-Zehnder waveguide immunosensor in silicon technology*. Sensors and Actuators B-Chemical, 1997. **40**(2-3): p. 147-153.
84. Bruck, R., et al., *Integrated polymer-based Mach-Zehnder interferometer label-free streptavidin biosensor compatible with injection molding*. Biosensors & Bioelectronics, 2011. **26**(9): p. 3832-3837.
85. Young, T., *A course of lectures on natural philosophy and the mechanical arts*. 1807, Princeton University: New Jersey.

86. Hradetzky, D., C. Mueller, and H. Reinecke, *Interferometric label-free biomolecular detection system*. Journal of Optics a-Pure and Applied Optics, 2006. **8**(7): p. S360-S364.
87. Ymeti, A., et al., *Realization of a multichannel integrated Young interferometer chemical sensor*. Applied Optics, 2003. **42**(28): p. 5649-5660.
88. Schmitt, K., et al., *Interferometric biosensor based on planar optical waveguide sensor chips for label-free detection of surface bound bioreactions*. Biosensors & Bioelectronics, 2007. **22**(11): p. 2591-2597.
89. Ymeti, A., et al., *An ultrasensitive young interferometer handheld sensor for rapid virus detection*. Expert Rev Med Devices, 2007. **4**(4): p. 447-54.
90. Ymeti, A., et al., *Fast, ultrasensitive virus detection using a Young interferometer sensor*. Nano Lett, 2007. **7**(2): p. 394-7.
91. Kanger, J.S., *Advanced Photonic Structures for Biological and Chemical Detection*. 2009.
92. St John, P.M., et al., *Diffraction-based cell detection using a microcontact printed antibody grating*. Anal Chem, 1998. **70**(6): p. 1108-11.
93. Houle, J.K., S., *Solving the Multiplexing-Dynamic Range Conundrum with Diffractive Optics Technology*. Nature Methods, 2007. **4**: p. i-ii.
94. Gnanaprakasa, T.J., et al., *Tethered DNA scaffolds on optical sensor platforms for detection of hipO gene from Campylobacter jejuni*. Sensors and Actuators B-Chemical, 2011. **156**(1): p. 304-311.
95. Swann, M.J., et al., *Dual-polarization interferometry: an analytical technique to measure changes in protein structure in real time, to determine the stoichiometry of binding events, and to differentiate between specific and nonspecific interactions*. Analytical Biochemistry, 2004. **329**(2): p. 190-198.
96. Lee, T.H. and M.I. Aguilar, *Dual Polarization Interferometry: An Optical Biosensor Which Allows New Insights into Peptide-Induced Changes in Biomembrane Structure*. Australian Journal of Chemistry, 2011. **64**(6): p. 844-845.
97. Baird, C.L. and D.G. Myszka, *Current and emerging commercial optical biosensors*. Journal of Molecular Recognition, 2001. **14**(5): p. 261-268.
98. .
99. Fransson, J., et al., *Human framework adaptation of a mouse anti-human IL-13 antibody*. J Mol Biol, 2010. **398**(2): p. 214-31.
100. Abdiche, Y., et al., *Determining kinetics and affinities of protein interactions using a parallel real-time label-free biosensor, the Octet*. Anal Biochem, 2008. **377**(2): p. 209-17.
101. Li, J., et al., *Detection of low-affinity anti-drug antibodies and improved drug tolerance in immunogenicity testing by Octet((R)) biolayer interferometry*. J Pharm Biomed Anal, 2011. **54**(2): p. 286-94.
102. Bornhop, D.J., *Microvolume Index of Refraction Determinations by Interferometric Backscatter*. Applied Optics, 1995. **34**(18): p. 3234-3239.
103. Swinney, K. and D.J. Bornhop, *Quantification and evaluation of Joule heating in on-chip capillary electrophoresis*. Electrophoresis, 2002. **23**(4): p. 613-20.
104. Swinney, K. and D.J. Bornhop, *Noninvasive picoliter volume thermometry based on backscatter interferometry*. Electrophoresis, 2001. **22**(10): p. 2032-6.

105. Swinney, K. and D.J. Bornhop, *A chip-scale universal detector for electrophoresis based on backscattering interferometry*. Analyst, 2000. **125**(10): p. 1713-7.
106. Swinney, K. and D.J. Bornhop, *Detection in capillary electrophoresis*. Electrophoresis, 2000. **21**(7): p. 1239-50.
107. Markov, D.A., K. Swinney, and D.J. Bornhop, *Label-free molecular interaction determinations with nanoscale interferometry*. J Am Chem Soc, 2004. **126**(50): p. 16659-64.
108. Wang, Z., K. Swinney, and D.J. Bornhop, *Attomole sensitivity for unlabeled proteins and polypeptides with on-chip capillary electrophoresis and universal detection by interferometric backscatter*. Electrophoresis, 2003. **24**(5): p. 865-73.
109. Swinney, K., D. Markov, and D.J. Bornhop, *Chip-scale universal detection based on backscatter interferometry*. Anal Chem, 2000. **72**(13): p. 2690-5.
110. Markov, D., D. Begari, and D.J. Bornhop, *Breaking the 10<sup>(-7)</sup> barrier for RI measurements in nanoliter volumes*. Anal Chem, 2002. **74**(20): p. 5438-41.
111. Bornhop, D.J., et al., *Free-solution, label-free molecular interactions studied by back-scattering interferometry*. Science, 2007. **317**(5845): p. 1732-1736.
112. Boucard, A.A., J.W. Ko, and T.C. Sudhof, *High Affinity Neurexin Binding to Cell Adhesion G-protein-coupled Receptor CIRL1/Latrophilin-1 Produces an Intercellular Adhesion Complex*. Journal of Biological Chemistry, 2012. **287**(12): p. 9399-9413.
113. Shenoy, S.S., H. Nanda, and M. Losche, *Membrane association of the PTEN tumor suppressor: Electrostatic interaction with phosphatidylserine-containing bilayers and regulatory role of the C-terminal tail*. Journal of Structural Biology, 2012. **180**(3): p. 394-408.
114. Fang, Y., A.G. Frutos, and J. Lahiri, *Membrane protein microarrays*. Journal of the American Chemical Society, 2002. **124**(11): p. 2394-2395.
115. Carlson, N.R., *Physiology of Behavior*. 9th ed. ed. 2007, Boston, MA: Allyn and Bacon.
116. Sharon, N. and H. Lis, *History of lectins: from hemagglutinins to biological recognition molecules*. Glycobiology, 2004. **14**(11): p. 53R-62R.
117. Swanson, M.D., et al., *A lectin isolated from bananas is a potent inhibitor of HIV replication*. J Biol Chem, 2010. **285**(12): p. 8646-55.
118. Cecioni, S., et al., *Selectivity among Two Lectins: Probing the Effect of Topology, Multivalency and Flexibility of "Clicked" Multivalent Glycoclusters*. Chemistry-a European Journal, 2011. **17**(7): p. 2146-2159.
119. Dhayal, M. and D.A. Ratner, *XPS and SPR Analysis of Glycoarray Surface Density*. Langmuir, 2009. **25**(4): p. 2181-2187.
120. VanEngelenburg, S.B. and A.E. Palmer, *Fluorescent biosensors of protein function*. Curr Opin Chem Biol, 2008. **12**(1): p. 60-5.
121. Joshi, P.P., et al., *Amperometric biosensors based on redox polymer-carbon nanotube-enzyme composites*. Anal Chem, 2005. **77**(10): p. 3183-8.
122. Chen, H., et al., *Bienzyme bionanomultilayer electrode for glucose biosensing based on functional carbon nanotubes and sugar-lectin biospecific interaction*. Anal Biochem, 2010. **403**(1-2): p. 36-42.

123. Linman, M.J., et al., *Surface plasmon resonance study of protein-carbohydrate interactions using biotinylated sialosides*. *Anal Chem*, 2008. **80**(11): p. 4007-13.
124. Black, F.E., et al., *Surface engineering and surface analysis of a biodegradable polymer with biotinylated end groups*. *Langmuir*, 1999. **15**(9): p. 3157-3161.
125. Herforth, C., et al., *Polymer-bound reagents for the introduction of spacer-modified biotin labels*. *Bioorganic & Medicinal Chemistry*, 2004. **12**(11): p. 2895-2902.
126. Longo, G.S., D.H. Thompson, and I. Szleifer, *Ligand-receptor interactions between surfaces: The role of binary polymer spacers*. *Langmuir*, 2008. **24**(18): p. 10324-10333.
127. Moreira, B.G., et al., *Effects of fluorescent dyes, quenchers, and dangling ends on DNA duplex stability*. *Biochemical and Biophysical Research Communications*, 2005. **327**(2): p. 473-484.
128. Owczarzy, R., B.G. Moreira, and Y. You, *Effects of fluorescent dyes, quenchers, and dangling ends on the thermodynamic stability of DNA duplexes*. *Biophysical Journal*, 2004. **86**(1): p. 310a-310a.
129. Piunno, P.A.E. and U.J. Krull, *Trends in the development of nucleic acid biosensors for medical diagnostics*. *Analytical and Bioanalytical Chemistry*, 2005. **381**(5): p. 1004-1011.
130. Sagle, L.B., et al., *Advances in localized surface plasmon resonance spectroscopy biosensing*. *Nanomedicine*, 2011. **6**(8): p. 1447-1462.
131. Bellapadrona, G., et al., *Optimization of localized surface plasmon resonance transducers for studying carbohydrate-protein interactions*. *Anal Chem*, 2012. **84**(1): p. 232-40.
132. Concepcion, J., et al., *Label-free detection of biomolecular interactions using BioLayer interferometry for kinetic characterization*. *Comb Chem High Throughput Screen*, 2009. **12**(8): p. 791-800.
133. .
134. Markov, D.A., K. Swinney, and D.J. Bornhop, *Label-free molecular interaction determinations with nanoscale interferometry*. *Journal of the American Chemical Society*, 2004. **126**(50): p. 16659-16664.
135. Drake, A.W., et al., *Biacore surface matrix effects on the binding kinetics and affinity of an antigen/antibody complex*. *Analytical Biochemistry*, 2012. **429**(1): p. 58-69.
136. Freitas, S.C., M.A. Barbosa, and M.C.L. Martins, *The effect of immobilization of thrombin inhibitors onto self-assembled monolayers on the adsorption and activity of thrombin*. *Biomaterials*, 2010. **31**(14): p. 3772-3780.
137. Spain, S.G. and N.R. Cameron, *The binding of polyvalent galactosides to the lectin Ricinus communis agglutinin 120 (RCA(120)): an ITC and SPR study*. *Polymer Chemistry*, 2011. **2**(7): p. 1552-1560.
138. Karlsson, R., *SPR for molecular interaction analysis: a review of emerging application areas*. *J Mol Recognit*, 2004. **17**(3): p. 151-61.
139. Tsai, C.S., T.B. Yu, and C.T. Chen, *Gold nanoparticle-based competitive colorimetric assay for detection of protein-protein interactions*. *Chem Commun (Camb)*, 2005(34): p. 4273-5.



140. Taguchi, T., H. Takeyama, and T. Matsunaga, *Immuno-capture of Cryptosporidium parvum using micro-well array*. Biosensors & Bioelectronics, 2005. **20**(11): p. 2276-2282.
141. Leavitt, S. and E. Freire, *Direct measurement of protein binding energetics by isothermal titration calorimetry*. Curr Opin Struct Biol, 2001. **11**(5): p. 560-6.
142. Upadhyaya, G.A., P.R. Harvey, and S.M. Strasberg, *Effect of human biliary immunoglobulins on the nucleation of cholesterol*. J Biol Chem, 1993. **268**(7): p. 5193-200.
143. Zhao, J., et al., *Glycoprotein microarrays with multi-lectin detection: unique lectin binding patterns as a tool for classifying normal, chronic pancreatitis and pancreatic cancer sera*. J Proteome Res, 2007. **6**(5): p. 1864-74.
144. Lewallen, D.M., D. Siler, and S.S. Iyer, *Factors affecting protein-glycan specificity: effect of spacers and incubation time*. Chembiochem, 2009. **10**(9): p. 1486-9.
145. Uchida, K., et al., *A reactive poly(ethylene glycol) layer to achieve specific surface plasmon resonance sensing with a high S/N ratio: the substantial role of a short underbrushed PEG layer in minimizing nonspecific adsorption*. Anal Chem, 2005. **77**(4): p. 1075-80.
146. Spinke, J., et al., *Molecular Recognition at Self-Assembled Monolayers - Optimization of Surface Functionalization*. Journal of Chemical Physics, 1993. **99**(9): p. 7012-7019.
147. Bull, H., *Adsorption of Bovine Serum ALbumin on Glass*. Biochemica et Biophysica Acta, 1956. **19**: p. 464-471.
148. Neurath, H.B., H.B., *The surface activity of proteins*. Chemical Reviews, 1938. **23**(3): p. 391-435.
149. Roach, P., D. Farrar, and C.C. Perry, *Interpretation of protein adsorption: Surface-induced conformational changes*. Journal of the American Chemical Society, 2005. **127**(22): p. 8168-8173.
150. Dabrowski, A., *Adsorption - from theory to practice*. Advances in Colloid and Interface Science, 2001. **93**(1-3): p. 135-224.
151. Yampolskaya, G. and D. Platikanov, *Proteins at fluid interfaces: Adsorption layers and thin liquid films*. Advances in Colloid and Interface Science, 2006. **128**: p. 159-183.
152. Zhang, X.H. and V.T. Moy, *Cooperative adhesion of ligand-receptor bonds*. Biophysical Chemistry, 2003. **104**(1): p. 271-278.
153. Perkins, D.I., et al., *Loop 2 Structure in Glycine and GABA(A) Receptors Plays a Key Role in Determining Ethanol Sensitivity*. Journal of Biological Chemistry, 2009. **284**(40): p. 27304-27314.
154. Mammen, M., S.K. Choi, and G.M. Whitesides, *Polyvalent interactions in biological systems: Implications for design and use of multivalent ligands and inhibitors*. Angewandte Chemie-International Edition, 1998. **37**(20): p. 2755-2794.
155. Zangar, R.C., D.S. Daly, and A.M. White, *ELISA microarray technology as a high-throughput system for cancer biomarker validation*. Expert Review of Proteomics, 2006. **3**(1): p. 37-44.

156. Liu, E. and G.S. Eisenbarth, *Accepting clocks that tell time poorly: Fluid-phase versus standard ELISA autoantibody assays*. *Clinical Immunology*, 2007. **125**(2): p. 120-126.
157. Jung, H., A.D. Robison, and P.S. Cremer, *Multivalent ligand-receptor binding on supported lipid bilayers*. *J Struct Biol*, 2009. **168**(1): p. 90-4.
158. Mukundan, H., et al., *Planar optical waveguide-based biosensor for the quantitative detection of tumor markers*. *Sensors and Actuators B-Chemical*, 2009. **138**(2): p. 453-460.
159. Baltus, R.E., K.S. Carmon, and L.A. Luck, *Quartz crystal microbalance (QCM) with immobilized protein receptors: comparison of response to ligand binding for direct protein immobilization and protein attachment via disulfide linker*. *Langmuir*, 2007. **23**(7): p. 3880-5.
160. Bock, L.C., et al., *Selection of single-stranded DNA molecules that bind and inhibit human thrombin*. *Nature*, 1992. **355**(6360): p. 564-6.
161. Tasset, D.M., M.F. Kubik, and W. Steiner, *Oligonucleotide inhibitors of human thrombin that bind distinct epitopes*. *Journal of Molecular Biology*, 1997. **272**(5): p. 688-698.
162. Cheng, A.J. and M.W. Van Dyke, *Oligodeoxyribonucleotide length and sequence effects on intramolecular and intermolecular G-quartet formation*. *Gene*, 1997. **197**(1-2): p. 253-60.
163. Fredenburgh, J.C., A.R. Stafford, and J.I. Weitz, *Evidence for allosteric linkage between exosites 1 and 2 of thrombin*. *J Biol Chem*, 1997. **272**(41): p. 25493-9.
164. Bordelon, H., et al., *Development of a low-resource RNA extraction cassette based on surface tension valves*. *ACS Appl Mater Interfaces*, 2011. **3**(6): p. 2161-8.
165. Bae, H.G., et al., *Detection of yellow fever virus: a comparison of quantitative real-time PCR and plaque assay*. *J Virol Methods*, 2003. **110**(2): p. 185-91.
166. Jayagopal, A., et al., *Hairpin DNA-functionalized gold colloids for the imaging of mRNA in live cells*. *J Am Chem Soc*, 2010. **132**(28): p. 9789-96.
167. Mehlmann, M., et al., *Robust sequence selection method used to develop the FluChip diagnostic microarray for influenza virus*. *J Clin Microbiol*, 2006. **44**(8): p. 2857-62.
168. Nam, J.M., S.I. Stoeva, and C.A. Mirkin, *Bio-bar-code-based DNA detection with PCR-like sensitivity*. *J Am Chem Soc*, 2004. **126**(19): p. 5932-3.
169. Marras, S.A., S. Tyagi, and F.R. Kramer, *Real-time assays with molecular beacons and other fluorescent nucleic acid hybridization probes*. *Clin Chim Acta*, 2006. **363**(1-2): p. 48-60.
170. Zhang, J., et al., *Rapid and label-free nanomechanical detection of biomarker transcripts in human RNA*. *Nat Nanotechnol*, 2006. **1**(3): p. 214-20.
171. Springer, T., M. Piliarik, and J. Homola, *Real-time monitoring of biomolecular interactions in blood plasma using a surface plasmon resonance biosensor*. *Anal Bioanal Chem*, 2010. **398**(5): p. 1955-61.
172. Perez, J.W., F.R. Haselton, and D.W. Wright, *Viral detection using DNA functionalized gold filaments*. *Analyst*, 2009. **134**(8): p. 1548-53.

173. Perez, J.W., et al., *Detection of respiratory syncytial virus using nanoparticle amplified immuno-polymerase chain reaction*. *Anal Biochem*, 2011. **410**(1): p. 141-8.
174. Vester, B. and J. Wengel, *LNA (locked nucleic acid): high-affinity targeting of complementary RNA and DNA*. *Biochemistry*, 2004. **43**(42): p. 13233-41.
175. Petersen, M., et al., *Locked nucleic acid (LNA) recognition of RNA: NMR solution structures of LNA:RNA hybrids*. *J Am Chem Soc*, 2002. **124**(21): p. 5974-82.
176. Ivanov, V.I., et al., *The B to A transition of DNA in solution*. *J Mol Biol*, 1974. **87**(4): p. 817-33.
177. Kypr, J., et al., *Circular dichroism and conformational polymorphism of DNA*. *Nucleic Acids Res*, 2009. **37**(6): p. 1713-25.
178. Wiese, K.C. and A. Hendriks, *Comparison of P-RnaPredict and mfold--algorithms for RNA secondary structure prediction*. *Bioinformatics*, 2006. **22**(8): p. 934-42.
179. Braasch, D.A. and D.R. Corey, *Locked nucleic acid (LNA): fine-tuning the recognition of DNA and RNA*. *Chem Biol*, 2001. **8**(1): p. 1-7.
180. Robertson, K.L. and D.C. Thach, *LNA flow-FISH: a flow cytometry-fluorescence in situ hybridization method to detect messenger RNA using locked nucleic acid probes*. *Anal Biochem*, 2009. **390**(2): p. 109-14.
181. Thanh, T.T., et al., *A real-time RT-PCR for detection of clade 1 and 2 H5N1 influenza A virus using locked nucleic acid (LNA) TaqMan probes*. *Virology*, 2010. **7**: p. 46.
182. Nielsen, K.E., et al., *NMR studies of fully modified locked nucleic acid (LNA) hybrids: solution structure of an LNA:RNA hybrid and characterization of an LNA:DNA hybrid*. *Bioconjug Chem*, 2004. **15**(3): p. 449-57.
183. Parkin, D.M., et al., *Global cancer statistics, 2002*. *CA Cancer J Clin*, 2005. **55**(2): p. 74-108.
184. Hoffman, P.C., A.M. Mauer, and E.E. Vokes, *Lung cancer*. *Lancet*, 2000. **355**(9202): p. 479-85.
185. Goh, J.B., R.W. Loo, and M.C. Goh, *Label-free monitoring of multiple biomolecular binding interactions in real-time with diffraction-based sensing*. *Sensors and Actuators B-Chemical*, 2005. **106**(1): p. 243-248.
186. Hori, S.S. and S.S. Gambhir, *Mathematical Model Identifies Blood Biomarker-Based Early Cancer Detection Strategies and Limitations*. *Science Translational Medicine*, 2011. **3**(109).
187. Whiteaker, J.R., et al., *A targeted proteomics-based pipeline for verification of biomarkers in plasma*. *Nature Biotechnology*, 2011. **29**(7): p. 625-U108.
188. Kikuchi, T., et al., *In-depth Proteomic Analysis of Nonsmall Cell Lung Cancer to Discover Molecular Targets and Candidate Biomarkers*. *Molecular & Cellular Proteomics*, 2012. **11**(10): p. 916-932.
189. Pastor, A., et al., *Diagnostic value of SCC, CEA and CYFRA 21.1 in lung cancer: A Bayesian analysis*. *European Respiratory Journal*, 1997. **10**(3): p. 603-609.
190. Takada, M., et al., *Measurement of cytokeratin 19 fragments as a marker of lung cancer by CYFRA 21-1 enzyme immunoassay*. *Br J Cancer*, 1995. **71**(1): p. 160-5.
191. Criqui, M.H., et al., *C-reactive protein and ten-year mortality in a clinical cohort*. *Circulation*, 2003. **107**(7): p. E7026-E7027.

192. Ridker, P.M., J.E. Buring, and N.R. Cook, *C-reactive protein in the prediction of cardiovascular events - Reply*. New England Journal of Medicine, 2003. **348**(11): p. 1060-1061.
193. Erbel, R. and M. Budoff, *Improvement of cardiovascular risk prediction using coronary imaging: subclinical atherosclerosis: the memory of lifetime risk factor exposure*. European Heart Journal, 2012. **33**(10): p. 1201-+.
194. Ridker, P.M., et al., *Development and validation of improved algorithms for the assessment of global cardiovascular risk in women - The Reynolds Risk Score*. Jama-Journal of the American Medical Association, 2007. **297**(6): p. 611-619.
195. Wang, Y., et al., *Roles of chemokine CXCL12 and its receptors in ischemic stroke*. Curr Drug Targets, 2012. **13**(2): p. 166-72.
196. Rempel, S.A., et al., *Identification and localization of the cytokine SDF1 and its receptor, CXC chemokine receptor 4, to regions of necrosis and angiogenesis in human glioblastoma*. Clin Cancer Res, 2000. **6**(1): p. 102-11.
197. Li, M. and R.M. Ransohoff, *Multiple roles of chemokine CXCL12 in the central nervous system: a migration from immunology to neurobiology*. Prog Neurobiol, 2008. **84**(2): p. 116-31.
198. Carbajal, K.S., et al., *Migration of engrafted neural stem cells is mediated by CXCL12 signaling through CXCR4 in a viral model of multiple sclerosis*. Proc Natl Acad Sci U S A, 2010. **107**(24): p. 11068-73.
199. Bonavia, R., et al., *Chemokines and their receptors in the CNS: expression of CXCL12/SDF-1 and CXCR4 and their role in astrocyte proliferation*. Toxicol Lett, 2003. **139**(2-3): p. 181-9.
200. Choi, W.T. and J. An, *Biology and clinical relevance of chemokines and chemokine receptors CXCR4 and CCR5 in human diseases*. Exp Biol Med (Maywood), 2011. **236**(6): p. 637-47.
201. Comerford, I. and S.R. McColl, *Mini-review series: focus on chemokines*. Immunol Cell Biol, 2011. **89**(2): p. 183-4.
202. Juarez, J., L. Bendall, and K. Bradstock, *Chemokines and their receptors as therapeutic targets: the role of the SDF-1/CXCR4 axis*. Curr Pharm Des, 2004. **10**(11): p. 1245-59.
203. Salcedo, R. and J.J. Oppenheim, *Role of chemokines in angiogenesis: CXCL12/SDF-1 and CXCR4 interaction, a key regulator of endothelial cell responses*. Microcirculation, 2003. **10**(3-4): p. 359-70.
204. Banisadr, G., et al., *Neuroanatomical distribution of CXCR4 in adult rat brain and its localization in cholinergic and dopaminergic neurons*. Eur J Neurosci, 2002. **16**(9): p. 1661-71.
205. Guyon, A. and J.L. Nahon, *Multiple actions of the chemokine stromal cell-derived factor-1alpha on neuronal activity*. J Mol Endocrinol, 2007. **38**(3): p. 365-76.
206. Rostene, W., et al., *Chemokines and chemokine receptors: new actors in neuroendocrine regulations*. Front Neuroendocrinol, 2011. **32**(1): p. 10-24.
207. Wang, J., R. Loberg, and R.S. Taichman, *The pivotal role of CXCL12 (SDF-1)/CXCR4 axis in bone metastasis*. Cancer Metastasis Rev, 2006. **25**(4): p. 573-87.

208. Gao, Z., et al., *Pancreatic stellate cells increase the invasion of human pancreatic cancer cells through the stromal cell-derived factor-1/CXCR4 axis*. *Pancreatology*, 2010. **10**(2-3): p. 186-93.
209. Liu, Y.L., et al., *Regulation of the chemokine receptor CXCR4 and metastasis by hypoxia-inducible factor in non small cell lung cancer cell lines*. *Cancer Biol Ther*, 2006. **5**(10): p. 1320-6.
210. Zhao, X.P., et al., *Transforming growth factor-beta1 upregulates the expression of CXC chemokine receptor 4 (CXCR4) in human breast cancer MCF-7 cells*. *Acta Pharmacol Sin*, 2010. **31**(3): p. 347-54.
211. Doranz, B.J., et al., *Chemokine receptors as fusion cofactors for human immunodeficiency virus type 1 (HIV-1)*. *Immunol Res*, 1997. **16**(1): p. 15-28.
212. Gabuzda, D. and J. Wang, *Chemokine receptors and mechanisms of cell death in HIV neuropathogenesis*. *J Neurovirol*, 2000. **6 Suppl 1**: p. S24-32.
213. Lazarini, F., et al., *Role of the alpha-chemokine stromal cell-derived factor (SDF-1) in the developing and mature central nervous system*. *Glia*, 2003. **42**(2): p. 139-48.
214. Busillo, J.M. and J.L. Benovic, *Regulation of CXCR4 signaling*. *Biochim Biophys Acta*, 2007. **1768**(4): p. 952-63.
215. Shepherd, A.J., et al., *Distinct modifications in Kv2.1 channel via chemokine receptor CXCR4 regulate neuronal survival-death dynamics*. *J Neurosci*, 2012. **32**(49): p. 17725-39.
216. Kaupmann, K., et al., *GABA(B)-receptor subtypes assemble into functional heteromeric complexes*. *Nature*, 1998. **396**(6712): p. 683-7.
217. Laviv, T., et al., *Compartmentalization of the GABAB receptor signaling complex is required for presynaptic inhibition at hippocampal synapses*. *J Neurosci*, 2011. **31**(35): p. 12523-32.
218. Guyon, A. and N. Leresche, *Modulation by different GABAB receptor types of voltage-activated calcium currents in rat thalamocortical neurones*. *J Physiol*, 1995. **485 ( Pt 1)**: p. 29-42.
219. Rane, M.J., et al., *Gamma-amino butyric acid type B receptors stimulate neutrophil chemotaxis during ischemia-reperfusion*. *J Immunol*, 2005. **174**(11): p. 7242-9.
220. Tian, J., et al., *Gamma-aminobutyric acid inhibits T cell autoimmunity and the development of inflammatory responses in a mouse type 1 diabetes model*. *J Immunol*, 2004. **173**(8): p. 5298-304.
221. Bowery, N.G., *GABAB receptor pharmacology*. *Annu Rev Pharmacol Toxicol*, 1993. **33**: p. 109-47.
222. Duthey, B., et al., *Anti-inflammatory effects of the GABA(B) receptor agonist baclofen in allergic contact dermatitis*. *Exp Dermatol*, 2010. **19**(7): p. 661-6.
223. Jones, J.W., et al., *Cell-free assay of G-protein-coupled receptors using fluorescence polarization*. *J Biomol Screen*, 2008. **13**(5): p. 424-9.
224. Guyon, A., et al., *Stromal cell-derived factor-1alpha modulation of the excitability of rat substantia nigra dopaminergic neurones: presynaptic mechanisms*. *J Neurochem*, 2006. **96**(6): p. 1540-50.

225. Bhattacharyya, B.J., et al., *The chemokine stromal cell-derived factor-1 regulates GABAergic inputs to neural progenitors in the postnatal dentate gyrus*. J Neurosci, 2008. **28**(26): p. 6720-30.
226. Qu, Y., et al., *Enhanced migration and CXCR4 over-expression in fibroblasts with telomerase reconstitution*. Mol Cell Biochem, 2008. **313**(1-2): p. 45-52.
227. Schonemeier, B., et al., *Regional and cellular localization of the CXCL12/SDF-1 chemokine receptor CXCR7 in the developing and adult rat brain*. J Comp Neurol, 2008. **510**(2): p. 207-20.
228. Tatsuta, M., et al., *Inhibition by gamma-amino-n-butyric acid and baclofen of gastric carcinogenesis induced by N-methyl-N'-nitro-N-nitrosoguanidine in Wistar rats*. Cancer Res, 1990. **50**(16): p. 4931-4.
229. Wang, T., W. Huang, and F. Chen, *Baclofen, a GABAB receptor agonist, inhibits human hepatocellular carcinoma cell growth in vitro and in vivo*. Life Sci, 2008. **82**(9-10): p. 536-41.
230. Azuma, H., et al., *Gamma-aminobutyric acid as a promoting factor of cancer metastasis; induction of matrix metalloproteinase production is potentially its underlying mechanism*. Cancer Res, 2003. **63**(23): p. 8090-6.
231. Han, D., et al., *Wound healing activity of gamma-aminobutyric Acid (GABA) in rats*. J Microbiol Biotechnol, 2007. **17**(10): p. 1661-9.
232. Guglani, L. and R. Lodha, *Enteral baclofen in the management of tetanus-related spasms: case report and review of literature*. J Trop Pediatr, 2007. **53**(2): p. 139-41.
233. Kolaski, K. and L.R. Logan, *Intrathecal baclofen in cerebral palsy: A decade of treatment outcomes*. J Pediatr Rehabil Med, 2008. **1**(1): p. 3-32.
234. Plassat, R., et al., *Treatment of spasticity with intrathecal Baclofen administration: long-term follow-up, review of 40 patients*. Spinal Cord, 2004. **42**(12): p. 686-93.
235. Addolorato, G., et al., *Baclofen: a new drug for the treatment of alcohol dependence*. Int J Clin Pract, 2006. **60**(8): p. 1003-8.
236. Wang, Z. and D.J. Bornhop, *Dual-capillary backscatter interferometry for high-sensitivity nanoliter-volume refractive index detection with density gradient compensation*. Anal Chem, 2005. **77**(24): p. 7872-7.
237. Wang, Z.L. and D.J. Bornhop, *Dual-capillary backscatter interferometry for high-sensitivity nanoliter-volume refractive index detection with density gradient compensation*. Analytical Chemistry, 2005. **77**(24): p. 7872-7877.
238. Dotson, S., *Experiments on and with backscattering interferometry*. Dissertation, 2008.
239. Watanabe, S., et al., *Surface plasmon resonance scattering and absorption sensing of Concanavalin A using glycoconjugated gold nanoparticles*. Supramolecular Chemistry, 2011. **23**(3-4): p. 297-303.
240. Yonzon, C.R., et al., *A comparative analysis of localized and propagating surface plasmon resonance sensors: The binding of concanavalin a to a monosaccharide functionalized self-assembled monolayer*. Journal of the American Chemical Society, 2004. **126**(39): p. 12669-12676.
241. Bell, S., et al., *p53 contains large unstructured regions in its native state*. Journal of Molecular Biology, 2002. **322**(5): p. 917-927.

Ian Olmsted  
1005 Elliston St, Old Hickory, TN 37138

828-719-9959 (Mobile)  
ianolmsted@yahoo.com

## **PROFILE**

---

Skilled research chemist completing doctorate in analytical chemistry in June, 2013. I have spent the last five years honing my skills as an assay development specialist and now plan to broaden my experience in the private sector. In addition to assay method development, I have spent considerable time designing, improving and troubleshooting interferometry-based assay instrumentation.

## **EDUCATION**

---

### **PhD, Analytical Chemistry**

Vanderbilt University Nashville, TN 2013

### **B.S. Chemistry, ACS Certified**

Appalachian State University Boone, NC 2008

- Cum Laude 2008

## **EMPLOYMENT**

---

### **Molecular Sensing, Inc.**

Assay Development Consultant Nashville, TN 2010 – 2012

- Designed and implemented drug target binding determinations performed with the backscattering interferometer, advised on future instrumentation and assay protocols.
- Reported findings and provided perspective to senior executive staff

### **Vanderbilt University**

Graduate Research Assistant Nashville, TN 2008 -

Present

- Worked on method development and utilization of backscattering interferometry for use in label free microfluidic binding assays under the direction of Dr. Darryl Bornhop
- Designed new instrument configurations, performed calibration, testing and troubleshooting of analytical instrumentation.
- Assisted writing of research grants for submission to NIH and NSF

### **Appalachian State University**

Undergraduate Research Assistant Boone, NC 2007

- Assisted Dr. Eric Allain in developing enzymes to hydrolyze starch molecules into sugar as part of a larger effort to produce fuel alcohol.

## **ADDITIONAL TRAINING**

---

### **Vanderbilt Institute for Nanoscale Engineering (VINSE)**

- Proficient in the use of ellipsometer, atomic force microscope, uv-vis spectrophotometer, GC/MS and HPLC

### **Breault Research Organization**

- Intro to ASAP optical ray trace modeling program.

## **SKILLS**

---

- Assay development
- Gel Electrophoresis
- ELISA
- GC/MS, EI/MS, LC/MS
- HPLC
- Instrument design, development, troubleshooting and maintenance
- Spectrophotometry
- Rotovap distillation
- Solid phase extraction
- Circular Dichroism

## **PUBLICATIONS**

---

1. "Measurement of Aptamer-Protein Interactions with Back-Scattering Interferometry," Ian R. Olmsted, Yi Xiao, Minseon Cho, Andrew T. Csordas, Jonathan H. Sheehan, Jens Meiler, H. Tom Soh, and Darryl J. Bornhop, *Analytical Chemistry*, vol. 83, pp. 8867-8870, 2011. DOI: 10.1021/ac202823m
2. "Comparison of Free-solution and Surface-immobilized Molecular Interactions using a Single Platform" Ian R. Olmsted, Amanda K. Kussrow, Darryl J. Bornhop, *Analytical Chemistry*, vol. 84(24), pp 10817-10822, 2012. DOI: 10.1021/ac3029333h
3. "The effect of hybridization-induced secondary structure alterations on viral RNA detection using backscattering interferometry" Nicholas M. Adams, Ian R. Olmsted, Frederick R. Haselton, Darryl J. Bornhop, David W. Wright. *Nucleic Acids Research*, March 2013. DOI: 10.1093/nar/gkt165
4. "Baclofen and other GABA<sub>B</sub> receptor agents are allosteric modulators of the CXCL12 chemokine receptor CXCR4" Guyon, A.; Kussrow, A.K.; Olmsted, I.R.; Bornhop, D.J.; Nahon, J-L. *Journal of Neuroscience* July 2013. DOI: 10.1523/JNEUROSCI.6070-11.2013